
Robot Force Control

ROBOT FORCE CONTROL

BRUNO SICILIANO AND LUIGI VILLANI

PRISMA Lab

Dipartimento di Informatica e Sistemistica

Università degli Studi di Napoli Federico II

Via Claudio 21, 80125 Napoli, Italy

Kluwer Academic Publishers
Boston/Dordrecht/London

To C. A. & F.
—BS

To My Parents
—LV

Contents

Preface	xi
Acknowledgments	xiii
1. INTRODUCTION	1
1. Motion control vs. interaction control	1
2. Indirect vs. direct force control	2
3. Experimental apparatus	4
2. MOTION CONTROL	7
1. Modeling	7
1.1 Kinematics	8
1.2 Dynamics	10
2. Tracking control	12
2.1 Dynamic model-based compensation	12
2.2 Euler angles error	14
2.3 Angle/axis error	16
2.4 Quaternion error	19
2.5 Computational issues	21
2.6 Redundancy resolution	23
3. Regulation	26
3.1 Static model-based compensation	26
3.2 Orientation errors	27
4. Further reading	28
3. INDIRECT FORCE CONTROL	31
1. Compliance control	31
1.1 Active compliance	32
1.2 Experiments	34
2. Impedance control	36
2.1 Active impedance	36
2.2 Inner motion control	38
2.3 Three-DOF impedance control	40
2.4 Experiments	40

3.	Six-DOF impedance control	43
3.1	Euler angles displacement	44
3.2	Angle/axis displacement	46
3.3	Quaternion displacement	50
3.4	Experiments	51
3.5	Nondiagonal six-DOF stiffness	61
4.	Further reading	63
4.	DIRECT FORCE CONTROL	65
1.	Force regulation	65
1.1	Static model-based compensation	66
1.2	Dynamic model-based compensation	67
1.3	Experiments	68
2.	Force and motion control	69
2.1	Force and position regulation	70
2.2	Force and position control	72
2.3	Moment and orientation control	75
2.4	Experiments	78
3.	Force tracking	82
3.1	Contact stiffness adaptation	82
3.2	Experiments	84
4.	Further reading	86
5.	ADVANCED FORCE AND POSITION CONTROL	89
1.	Task space dynamics	89
2.	Adaptive control	91
2.1	Regulation	91
2.2	Passivity-based control	97
2.3	Experiments	100
3.	Output feedback control	103
3.1	Regulation	104
3.2	Passivity-based control	106
3.3	Experiments	110
4.	Further reading	111
	Appendices	113
A-	Rigid Body Orientation	113
1.	Rotation matrix	113
2.	Euler angles	114
3.	Angle/axis	117
4.	Quaternion	118
B-	Models of Robot Manipulators	121
1.	Kinematic models	121
1.1	Six-joint manipulator	122
1.2	Seven-joint manipulator	127

2.	Dynamic models	128
2.1	Six-joint manipulator	129
2.2	Seven-joint manipulator	131
References		135
Index		145

Preface

Research on robot force control has flourished in the past two decades. Such a wide interest is motivated by the general desire of providing robotic systems with enhanced sensory capabilities. Robots using force, touch, distance, visual feedback are expected to autonomously operate in unstructured environments other than the typical industrial shop floor.

It should be no surprise that managing the interaction of a robot with the environment by adopting a purely motion control strategy turns out to be inadequate. The unavoidable modeling errors and uncertainties may cause a rise of the contact forces ultimately leading to an unstable behavior during the interaction. On the other hand, since the early work on telemanipulation, the use of force feedback was conceived to assist the human operator in the remote handling of objects with a slave manipulator. More recently, cooperative robot systems have been developed where two or more manipulators (viz. the fingers of a dexterous robot hand) are to be controlled so as to limit the exchanged forces and avoid squeezing of a commonly held object.

The subject of robot force control is not treated in depth in robotics textbooks, in spite of its crucial importance for practical manipulation tasks. In the few books addressing this topic, the material is often limited to single-degree-of-freedom tasks. On the other hand, several results are available in the robotics literature but no dedicated monograph exists. The book is thus aimed at filling this gap by providing a theoretical and experimental treatment of robot force control.

The topics covered are largely inspired by the research work of the authors and their colleagues in the robotics group at the University of Naples during the last decade, including the Doctorate thesis on force control by the second author. Nonetheless, the book is not a mere collection of the results that can be found in archival publications. The presentation of the various concepts is rather motivated by the aim to lie the methodology behind the robot force

control schemes in a uniform and instrumental yet mathematically rigorous fashion.

The force control problem is tackled as the natural evolution of the motion control problem, where feedback of the contact force as provided by a force/torque sensor is used to manage the interaction of a robot manipulator with a scarcely structured environment. In this respect, those control strategies, e.g. hybrid position/force control, devised for interaction with an accurately modeled environment are not treated.

The contents of the book are organized as follows. The interaction control problem is discussed in Chapter 1, where the motivation for the material to follow is sketched. Classical motion control schemes are presented in Chapter 2 with special concern to six-degree-of-freedom tasks and kinematic redundancy. Compliance control and impedance control are introduced in Chapter 3 as the basic strategies for indirect force control. Direct force control strategies are devised in Chapter 4 which are obtained via the closure of an outer force control loop while motion control is recovered by adopting a parallel composition of the two control actions. Chapter 5 is devoted to illustrating advanced force and position control strategies which include passivity-based, adaptive and output feedback control. Remarkably, most control schemes are experimentally tested on a setup consisting of a six-joint or a seven-joint industrial robot with open control architecture and force/torque sensor. Two appendices provide background material on rigid body orientation and the models of the robot manipulators used in the experiments.

The book is addressed to scholars and researchers entering the field of robot force control. The material can be used as a reference for part of a graduate course on robot control in Electrical and Mechanical Engineering.

Naples, September 1999

Bruno Siciliano and Luigi Villani

Acknowledgments

To Lorenzo Sciavicco goes the authors' largest sign of recognition for having pioneered research in robotics at University of Naples. He has ever constituted an inexhaustible source of inspiration and encouragement to face new challenges. The authors are grateful to Stefano Chiaverini for his substantial work in the field and his original contribution of the parallel approach. The material in Chapter 4 is greatly inspired by the joint papers with him. Warm thanks are due to Pasquale Ciacchio for having established, with the above two colleagues, the PRISMA Lab providing exciting facilities for local research. Most of the contents of Chapters 2 and 3 are the result of a fruitful cooperation with Fabrizio Caccavale and Ciro Natale. The latter also deserves a special note of mention for his invaluable support in the experimental activities, as well as for useful annotations on a draft of this book. A final word of appreciation is for Rob Zeller at Kluwer Academic Publishers in Boston for his valuable editorial assistance.

Chapter 1

INTRODUCTION

Some introductory remarks on the robot force control problem are given. The rationale for the control schemes presented in the subsequent chapters is illustrated, together with a description of the experimental apparatus.

1. MOTION CONTROL VS. INTERACTION CONTROL

Control of interaction between a robot manipulator and the environment is crucial for successful execution of a number of practical tasks where the robot end effector has to manipulate an object or perform some operation on a surface. Typical examples include polishing, deburring, machining or assembly. A complete classification of possible robot tasks is practically infeasible in view of the large variety of cases that may occur, nor would such a classification be really useful to find a general strategy to control *interaction with environment*.

During interaction, the environment sets constraints on the geometric paths that can be followed by the end effector. This situation is generally referred to as *constrained motion*. In such a case, the use of a purely *motion control* strategy for controlling interaction is a candidate to fail, as explained below.

Successful execution of an interaction task with the environment by using motion control could be obtained only if the task were accurately planned. This would in turn require an accurate model of both the robot manipulator (kinematics and dynamics) and the environment (geometry and mechanical features). Manipulator modeling can be known with enough precision, but a detailed description of the environment is difficult to obtain.

To understand the importance of task planning accuracy, it is sufficient to observe that to perform a mechanical part mating with a positional approach, the relative positioning of the parts should be guaranteed with an accuracy of an order of magnitude greater than part mechanical tolerance. Once the absolute

2 ROBOT FORCE CONTROL

position of one part is exactly known, the manipulator should guide the motion of the other with the same accuracy.

In practice, the planning errors may give rise to a *contact force* causing a deviation of the end effector from the desired trajectory. On the other hand, the control system reacts to reduce such deviation. This ultimately leads to a build-up of the contact force until saturation of the joint actuators is reached or breakage of the parts in contact occurs.

The higher the environment stiffness and position control accuracy are, the easier a situation like the one just described can occur. This drawback can be overcome if a *compliant behavior* is ensured during the interaction. This can be achieved either in a *passive* fashion by interposing a suitable compliant mechanical device between the manipulator end effector and the environment, or in an *active* fashion by devising a suitable *interaction control* strategy.

The *contact force* is the quantity describing the state of interaction in the most complete fashion. Therefore, it is expected that enhanced performance can be achieved with an interaction control provided that force measurements are available. To this purpose, a *force/torque sensor* can be mounted on a robot manipulator, typically between the wrist and the end effector, and its readings shall be passed to the robot control unit via a suitable interface.

Robot force control has attracted a wide number of researchers in the past two decades. A state-of-the-art of the first decade is provided in [111], whereas the progress of the last decade is surveyed in [105] and [35]. Just recently, a monograph on force control [48] has appeared. The following section is aimed at presenting the features of the main strategies of interaction control with proper reference to the key literature in the field.

2. INDIRECT VS. DIRECT FORCE CONTROL

Interaction control strategies can be grouped in two categories; those performing *indirect force control* and those performing *direct force control*. The main difference between the two categories is that the former achieve force control via motion control, without explicit closure of a force feedback loop; the latter, instead, offer the possibility of controlling the contact force to a desired value, thanks to the closure of a force feedback loop.

To the first category belong *compliance* (or *stiffness*) *control* [82, 87] and *impedance control* [50], where the position error is related to the contact force through a mechanical stiffness or impedance of adjustable parameters. A robot manipulator under impedance control is described by an equivalent mass-spring-damper system with the contact force as input. The resulting impedance in the various task space directions is typically nonlinear and coupled. If a force/torque sensor is available, then force measurements can be used in the control law so as to achieve a linear and decoupled impedance.

If a detailed model of the environment is available, a widely adopted strategy belonging to the second category is the *hybrid position/force control* which aims at controlling position along the unconstrained task directions and force along the constrained task directions. A selection matrix acting on both desired and feedback quantities serves this purpose for typically planar contact surfaces [84], whereas the explicit constraint equations have to be taken into account for general curved contact surfaces [115, 67, 68].

In most practical situations, a detailed model of the environment is not available. In such a case, an effective strategy still in the second category is the *inner/outer motion/force control* where an outer force control loop is closed around the inner motion control loop which is typically available in a robot manipulator [36]. In order to embed the possibility of controlling motion along the unconstrained task directions, the desired end-effector motion can be input to the inner loop of an inner/outer motion/force control scheme. The resulting *parallel control* is composed of a force control action and a motion control action, where the former is designed so as to dominate the latter in order to ensure force control along the constrained task directions [24].

The focus of the present book is on force control strategies which are conceived to manage the interaction with a more or less compliant environment without requiring an accurate model thereof. A simplified environment model is used to analyze the performance of the various schemes presented. On the other hand, the environment is an inherent part of the control scheme with the hybrid strategy which indeed represents the most effective interaction control for large values of contact stiffness, or an infinitely stiff (rigid) surface in the limit. For such a reason, hybrid position/force control schemes are not treated in the book.

The motion control problem is analyzed first not only to understand its limitations when the end effector interacts with the environment, but also to enlighten the possibility of achieving an indirect control of the contact force with a purely motion control strategy. The resulting schemes are compliance control and impedance control, depending whether a static or a dynamic model-based compensation is performed. Special emphasis is given to controlling six-degree-of-freedom interaction tasks involving the end-effector position and orientation when a contact force and moment is applied. The closure of a force feedback loop allows direct control of the contact force (moment) along the constrained task directions, and the parallel composition of the force and motion control actions also allows control of the end-effector position (orientation) along the unconstrained task directions. Practical issues like imperfect model-based compensation or lack of speed measurements are challenged by devising advanced force and position control schemes which respectively resort to parameter adaptation and output feedback.

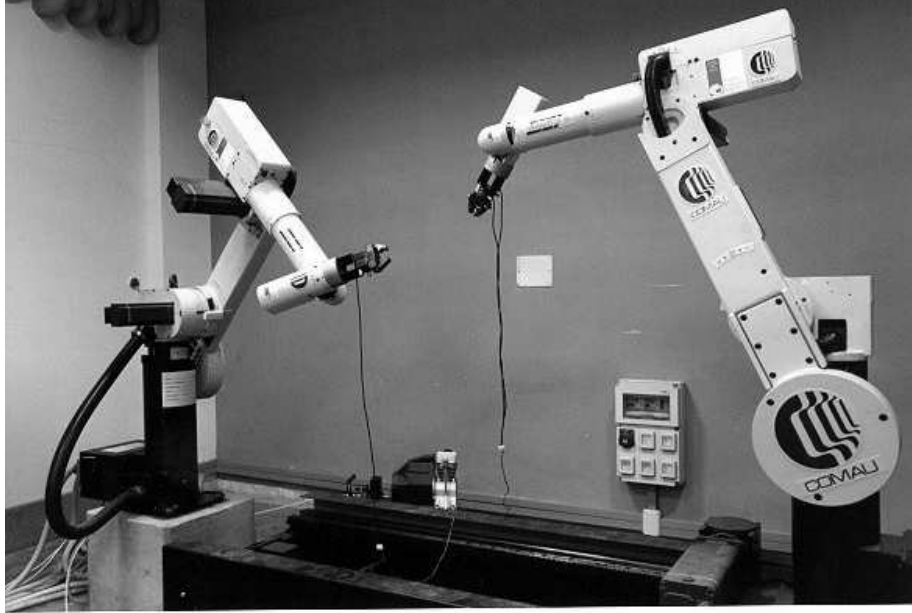


Figure 1.1. Experimental apparatus available in the PRISMA Lab.

In order to validate the theoretical findings, most of the force control schemes presented throughout the book are tested in a number of experiments for representative interaction tasks. Indeed, the force/torque sensor needed for the execution of interaction control schemes is not typically available for industrial robots, because of high cost and scarce reliability. A commercially available industrial robot has been purposefully utilized to demonstrate the credibility of force control in the perspective of the next generation of robot control units with enhanced sensory feedback capabilities. The problem of interfacing the force/torque sensor has been solved thanks to the open architecture of the control unit. This feature is crucial also for the implementation of control schemes requiring model-based compensation actions. The apparatus used for experimental testing is described in the next section.

3. EXPERIMENTAL APPARATUS

The *experimental apparatus* available in the PRISMA Lab comprises two industrial robots Comau SMART-3S (Fig. 1.1).

Each robot manipulator has a six-revolute-joint anthropomorphic geometry with nonnull shoulder and elbow offsets and non-spherical wrist. One manipulator is mounted on a sliding track which provides an additional degree of mobility. The joints are actuated by brushless motors via gear trains; shaft absolute resolvers provide motor position measurements. Each robot is con-

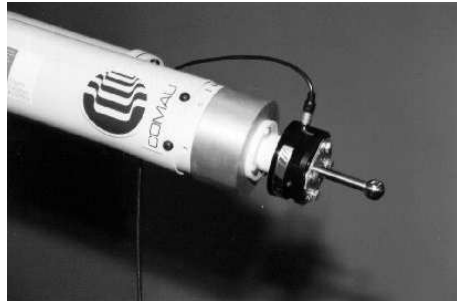


Figure 1.2. Force/torque sensor mounted at robot wrist.

trolled by the C3G 9000 control unit which has a VME-based architecture with 2 processing boards (Robot CPU and Servo CPU) both based on a Motorola 68020/68882, where the latter has an additional DSP and is in charge of trajectory generation, inverse kinematics and joint position servo control. Independent joint control is adopted where the individual servos are implemented as standard PID controllers. The native robot programming language is PDL 2, a high-level Pascal-like language with typical motion planning instructions.

An *open control architecture* is available which allows testing of advanced model-based control algorithms on a conventional industrial robot [37]. Connection of the VME bus of the C3G 9000 unit to the ISA bus of a standard PC is made possible by a BIT 3 Computer bus adapter board, and the PC and C3G controller communicate via the shared memory available in the Robot CPU; the experiments reported in the present book have been carried out by using a PC Pentium MMX/233. Time synchronization is implemented by interrupt signals from the C3G to the PC with data exchange at a given sampling rate. A set of C routines are available to drive the bus adapter boards. These routines are collected in a library (PCC3Link) and are devoted to performing communication tasks, e.g., reading shaft motor positions and/or writing motor reference currents from/to the shared memory. Also, a set of routines are devoted to performing safety checks and monitoring system health, e.g., a watchdog function and/or maximum current checks.

Seven different operating modes are available in the control unit, allowing the PC to interact with the original controller both at trajectory generation level and at joint control level. To implement model-based control schemes, the operating mode number 4 is used in which the PC is in charge of computing the control algorithm and passing the references to the current servos through the communication link at 1 ms sampling time. Joint velocities are reconstructed through numerical differentiation of joint position readings, except when a specific observer is used. All control algorithms are implemented in discrete time at 1 ms sampling interval.

6 ROBOT FORCE CONTROL

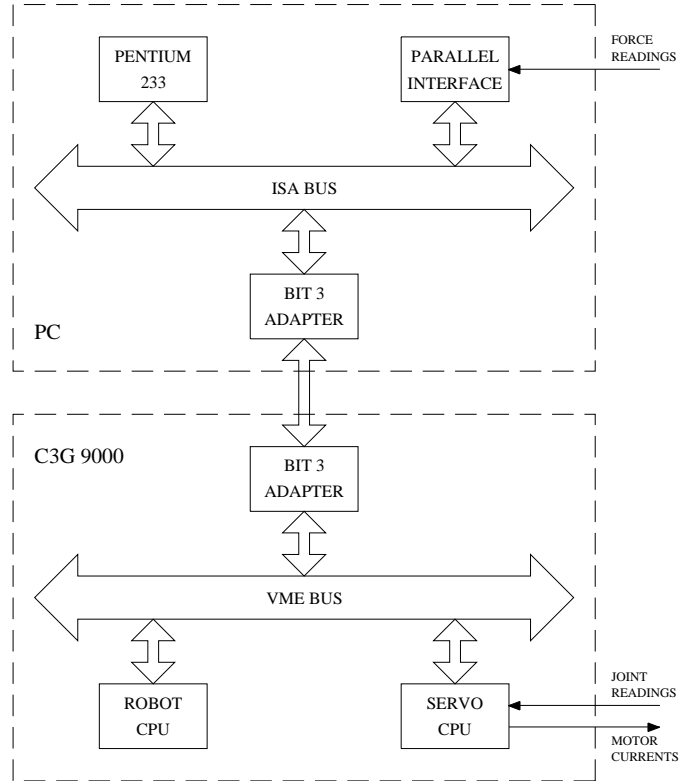


Figure 1.3. Schematic of open control architecture.

A six-axis *force/torque sensor* ATI FT30-100 with force range of ± 130 N and torque range of ± 10 N·m can be mounted at the wrist of either robot (Fig. 1.2). The sensor is connected to the PC by a parallel interface board which provides readings of six components of generalized force at 1 ms.

A schematic of the open control architecture is depicted in Fig. 1.3.

The type of environment considered in the various case studies presented in the following chapters consists of planar compliant surfaces of medium stiffness, with an estimated contact stiffness of the order of 10^4 N/m for translational displacements and of 10 Nm/rad for rotational displacements. This choice is motivated by the desire of safely analyzing the performance of the various control schemes where the interaction with the environment encompasses an unplanned transition from non-contact to contact at nonnegligible end-effector speed.

Chapter 2

MOTION CONTROL

Prior to tackling the force control problem, the motion control problem is analyzed. Kinematic and dynamic modeling of a robot manipulator are presented. The inverse dynamics strategy is pursued leading to a resolved acceleration control which ensures tracking of a desired end-effector position and orientation trajectory. Different types of orientation error are considered which are based on Euler angles, angle/axis and quaternion, respectively. A redundancy resolution scheme is embedded into the control. Regulation to a desired end-effector position and orientation is achieved by a PD control with gravity compensation.

1. MODELING

The class of robotic systems considered throughout this book is that of *robot manipulators*. The mechanical structure of a robot manipulator consists of a sequence of links connected by means of joints. Links and joints are usually made as rigid as possible to achieve high precision in robot positioning. An *end effector* is mounted at the tip of the manipulator which is specified according to the task the robot shall execute.

Completion of a generic robot task requires the execution of a specific motion prescribed to the manipulator end effector. The motion can be either unconstrained, if there is no physical interaction between the end effector and the environment, or constrained if contact forces arise between the end effector and the environment.

The correct execution of the end-effector motion is entrusted to the control system which shall provide the joint actuators of the manipulator with the commands consistent with the mechanical structure of the manipulator. Modeling a robot manipulator is therefore a necessary premise to finding motion control strategies. In the following, the kinematic model and the dynamic

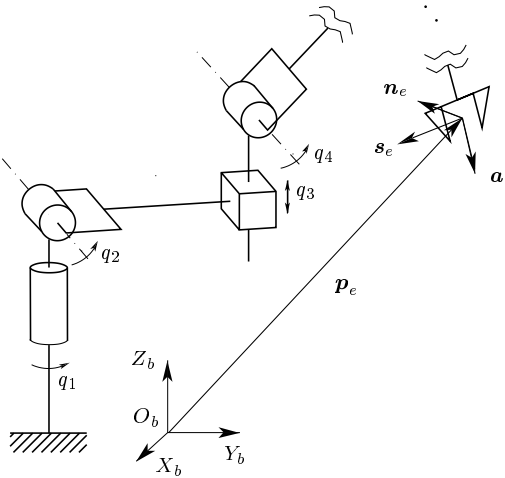


Figure 2.1. Schematic of an open-chain robot manipulator with base frame and end-effector frame.

model of a robot manipulator are concisely presented. The reader is referred to Appendix A for background material on rigid body orientation.

1.1 KINEMATICS

A robot manipulator consists of a kinematic chain of $n+1$ links connected by means of n joints. Joints can essentially be of two types: revolute and prismatic, while complex joints can be decomposed into these simple joints. Revolute joints are usually preferred to prismatic joints in view of their compactness and reliability. One end of the chain is connected to the base link, whereas an end effector is connected to the other end. The basic structure of a manipulator is the open kinematic chain which occurs when there is only one sequence of links connecting the two ends of the chain. Alternatively, a manipulator contains a closed kinematic chain when a sequence of links forms a loop. In Fig. 2.1, an open-chain robot manipulator is illustrated with conventional representation of revolute and prismatic joints.

Let \mathbf{q} denote the $(n \times 1)$ vector of *joint variables*, \mathbf{p}_e the (3×1) *position vector*, and

$$\mathbf{R}_e = [\mathbf{n}_e \quad \mathbf{s}_e \quad \mathbf{a}_e] \quad (2.1)$$

the (3×3) *rotation matrix*, describing the origin and the *orientation* of the end-effector frame, where \mathbf{n}_e , \mathbf{s}_e , \mathbf{a}_e are the unit vectors of the axes of the end-effector frame (Fig. 2.1). The quantities \mathbf{p}_e and \mathbf{R}_e characterize the end-effector frame $\Sigma_e(O_e-X_eY_eZ_e)$ with respect to a fixed base frame $\Sigma_b(O_b-X_bY_bZ_b)$ and no superscript is used; instead, if a matrix or vector quantity is to be referred to

a frame other than the base frame, then a proper frame superscript shall precede the quantity.

The *kinematic model* of the manipulator gives the relationship between \mathbf{q} and \mathbf{p}_e , i.e.

$$\mathbf{p}_e = \mathbf{p}_e(\mathbf{q}) \quad (2.2)$$

as well as between \mathbf{q} and \mathbf{R}_e , i.e.

$$\mathbf{R}_e = \mathbf{R}_e(\mathbf{q}). \quad (2.3)$$

Let $\dot{\mathbf{q}}$ denote the vector of joint velocities, $\dot{\mathbf{p}}_e$ the (3×1) vector of end-effector *linear velocity*, and $\boldsymbol{\omega}_e$ the (3×1) vector of end-effector *angular velocity*. The *differential kinematics* model gives the relationship between $\dot{\mathbf{q}}$ and

$$\mathbf{v}_e = \begin{bmatrix} \dot{\mathbf{p}}_e \\ \boldsymbol{\omega}_e \end{bmatrix} \quad (2.4)$$

in the form

$$\mathbf{v}_e = \mathbf{J}(\mathbf{q})\dot{\mathbf{q}} \quad (2.5)$$

where \mathbf{J} is the $(6 \times n)$ end-effector geometric *Jacobian* matrix. The Jacobian can be partitioned as

$$\mathbf{J} = \begin{bmatrix} \mathbf{J}_p \\ \mathbf{J}_o \end{bmatrix} \quad (2.6)$$

to separate the contributions of the joint velocities to the linear and the angular velocity in (2.4). The joint configurations at which the matrix \mathbf{J} is not full-rank are termed *kinematic singularities*.

The angular velocity is related to the time derivative of the rotation matrix by the notable relationship

$$\dot{\mathbf{R}}_e = \mathbf{S}(\boldsymbol{\omega}_e)\mathbf{R}_e \quad (2.7)$$

where \mathbf{S} is defined as in (A.4).

The description of end-effector orientation by a rotation matrix is nonminimal since the nine elements of the matrix are subject to the six constraints expressed by (A.1), and thus an arbitrary orientation can be completely specified in terms of three degrees of freedom. Since an arbitrary position is specified in terms of three independent coordinates, it follows that a general motion task for the end-effector position and orientation requires m degrees of freedom with $m \leq 6$. Whenever the number of joints exceeds the number of degrees of freedom, i.e. $n > m$, the manipulator is said *kinematically redundant*. Notice that redundancy is a concept relative to the end-effector task; for instance, a six-joint manipulator becomes redundant relative to a laser-cutting task since the end-effector rotation about the approach direction (\mathbf{a}_e) is irrelevant to completion of the task. On the other hand, a seven-joint manipulator is inherently redundant with respect to any end-effector task.

1.2 DYNAMICS

Dynamic modeling of a robot manipulator consists of finding the relationship between the forces exerted on the structure and the joint positions, velocities and accelerations. The *dynamic model* can be derived using the Lagrange formulation. Since the joint variables q_i constitute a set of generalized coordinates for the mechanical system, the Lagrange equations can be written as

$$\frac{d}{dt} \frac{\partial \mathcal{L}}{\partial \dot{q}_i} - \frac{\partial \mathcal{L}}{\partial q_i} = \xi_i \quad i = 1, \dots, n \quad (2.8)$$

where

$$\mathcal{L} = \mathcal{T} - \mathcal{U} \quad (2.9)$$

is the Lagrangian given by the difference between *kinetic energy* and *potential energy*, and ξ_i is the generalized force at joint i ; a torque for a revolute joint and a force for a prismatic joint, respectively. Typically the generalized forces are shortly referred to as torques, since most joints of a manipulator are revolute.

The kinetic energy is a quadratic form of the joint velocities, i.e.

$$\mathcal{T} = \frac{1}{2} \dot{\mathbf{q}}^T \mathbf{B}(\mathbf{q}) \dot{\mathbf{q}} \quad (2.10)$$

where the $(n \times n)$ matrix $\mathbf{B}(\mathbf{q})$ is the inertia matrix of the robot manipulator which is symmetric and positive definite. Substituting (2.10) in (2.9) and taking the derivatives needed by (2.8) leads to the equations of motion

$$\mathbf{B}(\mathbf{q}) \ddot{\mathbf{q}} + \mathbf{C}(\mathbf{q}, \dot{\mathbf{q}}) \dot{\mathbf{q}} + \mathbf{g}(\mathbf{q}) = \boldsymbol{\xi} \quad (2.11)$$

where $\boldsymbol{\xi}$ is the $(n \times 1)$ vector of joint torques, $\mathbf{g}(\mathbf{q})$ is the $(n \times 1)$ vector of gravity torques with

$$g_i(\mathbf{q}) = \frac{\partial \mathcal{U}}{\partial q_i}, \quad (2.12)$$

and

$$\mathbf{C}(\mathbf{q}, \dot{\mathbf{q}}) \dot{\mathbf{q}} = \dot{\mathbf{B}}(\mathbf{q}, \dot{\mathbf{q}}) \dot{\mathbf{q}} - \frac{1}{2} \left(\frac{\partial}{\partial \mathbf{q}} (\dot{\mathbf{q}}^T \mathbf{B}(\mathbf{q}) \dot{\mathbf{q}}) \right)^T \quad (2.13)$$

is the $(n \times 1)$ vector of Coriolis and centrifugal torques. This term is quadratic in the joint velocities, and thus its generic element can be written as

$$C_{ij} = \sum_{k=1}^n c_{ijk} \dot{q}_j \dot{q}_k. \quad (2.14)$$

There exist several choices of the elements C_{ij} of the matrix \mathbf{C} satisfying (2.14) corresponding to different factorizations of the term $\mathbf{C}(\mathbf{q}, \dot{\mathbf{q}}) \dot{\mathbf{q}}$. The choice

$$c_{ijk} = \frac{1}{2} \left(\frac{\partial B_{ij}}{\partial q_k} + \frac{\partial B_{ik}}{\partial q_j} - \frac{\partial B_{jk}}{\partial q_i} \right), \quad (2.15)$$

where the c_{ijk} 's are termed *Christoffel symbols* of the first type, makes the matrix $\dot{\mathbf{B}} - 2\mathbf{C}$ skew-symmetric; this property is very useful for control design purposes.

Regarding the joint torque, each joint is driven by an actuator (direct drive or gear drive); in general, the following torque contributions appear

$$\xi_i = \tau_i - \tau_{fi} - \tau_{ei} \quad (2.16)$$

where τ_i is the driving torque at the joint, τ_{fi} is the torque due to joint friction, and τ_{ei} is the torque caused by the external force and moment exerted by the end effector when in contact with the environment. Note that the actuators (electric or hydraulic) have been assumed as ideal torque generators.

Joint friction is difficult to model accurately; as a simplified model, only viscous friction is considered, i.e.

$$\tau_f = \mathbf{F}\dot{\mathbf{q}} \quad (2.17)$$

where \mathbf{F} is a positive definite (diagonal) matrix of viscous friction coefficients at the joints. More complex models would include nonlinear phenomena such as Coulomb friction and Stribeck effects.

Finally, let \mathbf{f} denote the (3×1) vector of external *end-effector force* and $\boldsymbol{\mu}$ the (3×1) vector of external *end-effector moment*. By applying the principle of virtual work, the resulting joint torques are

$$\tau_e = \mathbf{J}^T(\mathbf{q})\mathbf{h} \quad (2.18)$$

where

$$\mathbf{h} = \begin{bmatrix} \mathbf{f} \\ \boldsymbol{\mu} \end{bmatrix} \quad (2.19)$$

and \mathbf{J} is defined in (2.5).

In view of (2.16), (2.17) and (2.18), the dynamic model can be written in the form

$$\mathbf{B}(\mathbf{q})\ddot{\mathbf{q}} + \mathbf{C}(\mathbf{q}, \dot{\mathbf{q}})\dot{\mathbf{q}} + \mathbf{F}\dot{\mathbf{q}} + \mathbf{g}(\mathbf{q}) = \boldsymbol{\tau} - \mathbf{J}^T(\mathbf{q})\mathbf{h}. \quad (2.20)$$

It can be shown that equation (2.20) can be cast in a linear form with respect to a suitable $(p \times 1)$ vector $\boldsymbol{\pi}$ of dynamic parameters as

$$\mathbf{Y}(\mathbf{q}, \dot{\mathbf{q}}, \ddot{\mathbf{q}})\boldsymbol{\pi} = \boldsymbol{\tau} - \mathbf{J}^T(\mathbf{q})\mathbf{h} \quad (2.21)$$

where the $(n \times p)$ matrix \mathbf{Y} is termed *regressor* of the dynamic model. In general, the dynamic parameters depend on the mass, first moment of inertia and inertia tensor of each link, and the friction coefficient of each joint.

2. TRACKING CONTROL

The motion control problem for a robot manipulator can be formulated as finding the joint torques which ensure that the end effector attains a desired position and orientation. The usual way of solving this problem when the end effector is not in contact with the environment consists of two stages; first the manipulator kinematics is inverted to compute the joint variables corresponding to the given end-effector position and orientation, then a controller is designed which guarantees that the joints attain the computed values. This strategy is known as *kinematic control*.

Since the present book is focused on the problem of controlling the interaction between the manipulator end effector and the environment, a different strategy is pursued which consists of a single stage, i.e. the design of a so-called *task space control*. Direct task space feedback is utilized where the end-effector position and orientation is computed via the kinematics relationships from the joint measurements.

More specifically, the goal can be either to follow a *time-varying* desired position and orientation, i.e. a *tracking control* problem, or to reach a *constant* desired position and orientation, i.e. a *regulation* problem. The former problem is treated next, while the latter problem will be treated in Section 3.

2.1 DYNAMIC MODEL-BASED COMPENSATION

The dynamic model in the form (2.20) is represented by a set of n second-order coupled and nonlinear differential equations relating the joint positions, velocities and accelerations to the joint torques and the end-effector force and moment. A classical strategy to control this type of mechanical system is *inverse dynamics control*, which is aimed at linearizing and decoupling the manipulator dynamics via feedback. Nonlinearities such as Coriolis and centrifugal torques, friction torques, and gravity torques can be merely cancelled by adding these terms to the control input, while decoupling can be achieved by weighting the control input by the inertia matrix. According to this *dynamic model-based compensation*, the joint torques can be chosen as

$$\tau = \mathbf{B}(q)\alpha + \mathbf{C}(q, \dot{q})\dot{q} + \mathbf{F}\dot{q} + \mathbf{g}(q) \quad (2.22)$$

where it has been assumed $\mathbf{h} = \mathbf{0}$, i.e. no interaction with the environment, while α constitutes a new control input to be properly designed.

Folding the control law (2.22) into the system model (2.20), and taking into account that $\mathbf{B}(q)$ is always nonsingular, yields

$$\ddot{q} = \alpha \quad (2.23)$$

which constitutes a linear and decoupled system corresponding to a double integrator between the input α and the output q . The quantity α represents a *resolved acceleration* in terms of joint variables.

Equation (2.23) has been obtained under the assumption of perfect compensation of the terms in (2.20). This relies on the availability of an accurate dynamic model, as can be obtained via an identification procedure of the dynamic parameters in (2.21). In case of imperfect compensation, a mismatching occurs which causes the presence of a disturbance term in (2.23), i.e.

$$\ddot{\mathbf{q}} = \boldsymbol{\alpha} - \boldsymbol{\delta}; \quad (2.24)$$

in practice, the disturbance $\boldsymbol{\delta}$ is mainly due unmodeled dynamics, such as imperfect compensation of friction torques since they are difficult to model accurately.

As pointed out above, the goal is to design a *position control* action ensuring tracking of a desired end-effector position trajectory as well as an *orientation control* action ensuring tracking of a desired end-effector orientation trajectory. Since Equation (2.23) contains $\ddot{\mathbf{q}}$, it is worth considering the time derivative of (2.5), i.e.

$$\dot{\mathbf{v}}_e = \mathbf{J}(\mathbf{q})\ddot{\mathbf{q}} + \dot{\mathbf{J}}(\mathbf{q}, \dot{\mathbf{q}})\dot{\mathbf{q}} \quad (2.25)$$

which provides the relationship between the joint accelerations and the end-effector linear and angular accelerations.

At this point, the new control input $\boldsymbol{\alpha}$ in (2.23) can be chosen as

$$\boldsymbol{\alpha} = \mathbf{J}^{-1}(\mathbf{q}) (\mathbf{a} - \dot{\mathbf{J}}(\mathbf{q}, \dot{\mathbf{q}})\dot{\mathbf{q}}) \quad (2.26)$$

which in view of (2.25) leads to

$$\dot{\mathbf{v}}_e = \mathbf{a} \quad (2.27)$$

where \mathbf{a} attains the meaning of a *resolved acceleration* in terms of end-effector variables.

In deriving (2.26), a nonredundant manipulator ($n = 6$) moving in a singularity-free region of the workspace has been considered to compute the inverse of the Jacobian. A damped least-squares inverse can be adopted to gain robustness in the neighborhood of kinematic singularities, whereas a *pseudo-inverse* can be used in the redundant case ($n > 6$) in conjunction with a suitable term in the null space of the Jacobian describing the internal motion of the manipulator, as shall be seen in Subsection 2.6.

In the case of the presence of a disturbance as in (2.24), Equation (2.27) shall be modified into

$$\dot{\mathbf{v}}_e = \mathbf{a} - \mathbf{d} \quad (2.28)$$

where $\mathbf{d} = \mathbf{J}(\mathbf{q})\boldsymbol{\delta}$.

In view of the partition of \mathbf{v}_e in (2.4), it is appropriate to partition the vector \mathbf{a} into its linear and angular components, i.e.

$$\mathbf{a} = \begin{bmatrix} \mathbf{a}_p \\ \mathbf{a}_o \end{bmatrix} \quad (2.29)$$

where \mathbf{a}_p and \mathbf{a}_o are (3×1) vectors. Therefore, Equation (2.27) can be rewritten as

$$\ddot{\mathbf{p}}_e = \mathbf{a}_p \quad (2.30)$$

$$\dot{\omega}_e = \mathbf{a}_o, \quad (2.31)$$

where \mathbf{a}_p and \mathbf{a}_o shall be designed so as to ensure tracking of the desired end-effector position and orientation trajectory, respectively.

The desired position trajectory is specified in terms of the position vector $\mathbf{p}_d(t)$, linear velocity vector $\dot{\mathbf{p}}_d(t)$ and linear acceleration vector $\ddot{\mathbf{p}}_d(t)$, whereas the desired orientation trajectory is specified in terms of the rotation matrix $\mathbf{R}_d(t)$, angular velocity vector $\omega_d(t)$ and angular acceleration vector $\dot{\omega}_d(t)$. The quantities \mathbf{p}_d and \mathbf{R}_d characterize the origin and the orientation of a desired frame Σ_d .

A *position error* between the desired and the actual end-effector position can be defined as

$$\Delta \mathbf{p}_{de} = \mathbf{p}_d - \mathbf{p}_e \quad (2.32)$$

where the operator Δ denotes that a vector difference has been taken, and the double subscript denotes the corresponding frames. Then, the resolved linear acceleration can be chosen as

$$\mathbf{a}_p = \ddot{\mathbf{p}}_d + \mathbf{K}_{Dp} \Delta \dot{\mathbf{p}}_{de} + \mathbf{K}_{Pp} \Delta \mathbf{p}_{de} \quad (2.33)$$

where \mathbf{K}_{Dp} and \mathbf{K}_{Pp} are suitable feedback matrix gains. Substituting (2.33) into (2.30) gives the closed-loop dynamic behavior of the position error

$$\Delta \ddot{\mathbf{p}}_{de} + \mathbf{K}_{Dp} \Delta \dot{\mathbf{p}}_{de} + \mathbf{K}_{Pp} \Delta \mathbf{p}_{de} = \mathbf{0}. \quad (2.34)$$

The system (2.34) is exponentially stable for any choice of positive definite \mathbf{K}_{Dp} and \mathbf{K}_{Pp} , and thus tracking of \mathbf{p}_d and $\dot{\mathbf{p}}_d$ is ensured.

As regards the resolved angular acceleration, \mathbf{a}_o can be chosen in different ways, depending on the definition of end-effector orientation error used. Therefore, in the following three subsections, various definitions of *orientation error* are considered which make use of *Euler angles*, *angle/axis* and *quaternion*, respectively. The derivation of the control laws relies on the mathematical background that can be found in Appendix A.

2.2 EULER ANGLES ERROR

The most natural way of defining an orientation error is to consider an expression analogous to the position error in (2.32), i.e.

$$\Delta \boldsymbol{\varphi}_{de} = \boldsymbol{\varphi}_d - \boldsymbol{\varphi}_e \quad (2.35)$$

where $\boldsymbol{\varphi}_d$ and $\boldsymbol{\varphi}_e$ are the set of Euler angles that can be extracted respectively from the rotation matrices \mathbf{R}_d and \mathbf{R}_e describing the orientation of Σ_d and Σ_e .

Since Equation (2.31) contains $\dot{\omega}_e$, it is worth considering the relationship between the time derivative of the Euler angles $\dot{\varphi}_e$ and the end-effector angular velocity ω_e , i.e.

$$\omega_e = \mathbf{T}(\varphi_e) \dot{\varphi}_e \quad (2.36)$$

where \mathbf{T} is a transformation matrix that depends on the particular set of Euler angles considered; this matrix suffers from two *representation singularities*. The time derivative of (2.36) yields the acceleration relationship in the form

$$\ddot{\omega}_e = \mathbf{T}(\varphi_e) \ddot{\varphi}_e + \dot{\mathbf{T}}(\varphi_e, \dot{\varphi}_e) \dot{\varphi}_e. \quad (2.37)$$

As concerns the desired end-effector orientation trajectory in terms of Euler angles, the time derivative of $\dot{\varphi}_d$ can be computed as

$$\dot{\varphi}_d = \mathbf{T}^{-1}(\varphi_d) \omega_d, \quad (2.38)$$

whereas the time derivative of $\dot{\varphi}_d$ can be computed as

$$\ddot{\varphi}_d = \mathbf{T}^{-1}(\varphi_d) \left(\dot{\omega}_d - \dot{\mathbf{T}}(\varphi_d, \dot{\varphi}_d) \dot{\varphi}_d \right), \quad (2.39)$$

with obvious reference to (2.36) and (2.37); the matrix $\mathbf{T}(\varphi_d)$ in (2.38) and (2.39) has been assumed to be nonsingular.

In view of (2.37), the resolved angular acceleration based on the *Euler angles error* can be chosen as

$$\mathbf{a}_o = \mathbf{T}(\varphi_e) (\ddot{\varphi}_d + \mathbf{K}_{Do} \Delta \dot{\varphi}_{de} + \mathbf{K}_{Po} \Delta \varphi_{de}) + \dot{\mathbf{T}}(\varphi_e, \dot{\varphi}_e) \dot{\varphi}_e \quad (2.40)$$

where \mathbf{K}_{Do} and \mathbf{K}_{Po} are suitable feedback matrix gains. Substituting (2.40) into (2.31) gives the closed-loop dynamic behavior of the orientation error

$$\Delta \ddot{\varphi}_{de} + \mathbf{K}_{Do} \Delta \dot{\varphi}_{de} + \mathbf{K}_{Po} \Delta \varphi_{de} = \mathbf{0}, \quad (2.41)$$

where (2.37) has been used assuming that the matrix $\mathbf{T}(\varphi_e)$ is nonsingular. The system (2.41) is exponentially stable for any choice of positive definite \mathbf{K}_{Do} and \mathbf{K}_{Po} ; tracking of φ_d and $\dot{\varphi}_d$ is ensured, which in turn implies tracking of \mathbf{R}_d and ω_d .

The above Euler angles error becomes ill-conditioned when the actual end-effector orientation φ_e becomes close to a representation singularity. In order to overcome this drawback, an *alternative Euler angles error* can be considered which is based on the rotation matrix describing the mutual orientation between Σ_d and Σ_e , i.e.

$${}^e \mathbf{R}_d = \mathbf{R}_e^T \mathbf{R}_d \quad (2.42)$$

as in (A.8). Differentiating (2.42) with respect to time and accounting for (A.9) gives

$${}^e \dot{\mathbf{R}}_d = \mathbf{S}(\Delta {}^e \omega_{de}) {}^e \mathbf{R}_d \quad (2.43)$$

where

$$\Delta^e \boldsymbol{\omega}_{de} = {}^e \boldsymbol{\omega}_d - {}^e \boldsymbol{\omega}_e \quad (2.44)$$

is the end-effector angular velocity error which has been referred to Σ_e .

Let $\boldsymbol{\varphi}_{de}$ denote the set of Euler angles that can be extracted from ${}^e \mathbf{R}_d$. Then, in view of (2.36), the angular velocity $\Delta^e \boldsymbol{\omega}_{de}$ in (2.43) is related to the time derivative of $\boldsymbol{\varphi}_{de}$ as

$$\Delta^e \boldsymbol{\omega}_{de} = \mathbf{T}(\boldsymbol{\varphi}_{de}) \dot{\boldsymbol{\varphi}}_{de}. \quad (2.45)$$

The time derivative of (2.45) gives the acceleration relationship in the form

$$\dot{\boldsymbol{\omega}}_e = \dot{\boldsymbol{\omega}}_d - \mathbf{T}_e(\boldsymbol{\varphi}_{de}) \ddot{\boldsymbol{\varphi}}_{de} - \dot{\mathbf{T}}_e(\boldsymbol{\varphi}_{de}, \dot{\boldsymbol{\varphi}}_{de}) \dot{\boldsymbol{\varphi}}_{de} \quad (2.46)$$

where

$$\mathbf{T}_e(\boldsymbol{\varphi}_{de}) = \mathbf{R}_e \mathbf{T}(\boldsymbol{\varphi}_{de}). \quad (2.47)$$

In view of (2.46), the resolved angular acceleration can be chosen as

$$\boldsymbol{a}_o = \dot{\boldsymbol{\omega}}_d + \mathbf{T}_e(\boldsymbol{\varphi}_{de}) (\mathbf{K}_{Do} \dot{\boldsymbol{\varphi}}_{de} + \mathbf{K}_{Po} \boldsymbol{\varphi}_{de}) - \dot{\mathbf{T}}_e(\boldsymbol{\varphi}_{de}, \dot{\boldsymbol{\varphi}}_{de}) \dot{\boldsymbol{\varphi}}_{de} \quad (2.48)$$

where \mathbf{K}_{Do} and \mathbf{K}_{Po} are suitable feedback matrix gains. Substituting (2.48) into (2.31) gives the closed-loop dynamic behavior of the orientation error

$$\ddot{\boldsymbol{\varphi}}_{de} + \mathbf{K}_{Do} \dot{\boldsymbol{\varphi}}_{de} + \mathbf{K}_{Po} \boldsymbol{\varphi}_{de} = \mathbf{0} \quad (2.49)$$

where (2.46) has been used assuming that the matrix $\mathbf{T}_e(\boldsymbol{\varphi}_{de})$ is nonsingular. The system (2.49) is exponentially stable for any choice of positive definite \mathbf{K}_{Do} and \mathbf{K}_{Po} ; convergence to $\boldsymbol{\varphi}_{de} = \mathbf{0}$ and $\dot{\boldsymbol{\varphi}}_{de} = \mathbf{0}$ is ensured, which in turn implies tracking of \mathbf{R}_d and $\boldsymbol{\omega}_d$.

The clear advantage of the alternative over the classical Euler angles error based on (2.35) is that, by adopting a representation $\boldsymbol{\varphi}_{de} = [\alpha_{de} \ \beta_{de} \ \gamma_{de}]^T$ for which $\mathbf{T}(\mathbf{0})$ is nonsingular, representation singularities occur only for large orientation errors, e.g. when $\beta_{de} = \pm\pi/2$ for the XYZ representation in (A.11). Notice that it is not advisable to choose the widely-adopted ZYZ representation which is singular right at $\boldsymbol{\varphi}_{de} = \mathbf{0}$ (see the transformation matrix in (A.18))! In other words, the ill-conditioning of matrix \mathbf{T} is not influenced by the desired or actual end-effector orientation but only by the orientation error; hence, as long as the error parameter $|\beta_{de}| < \pi/2$, the behavior of system (2.31) and (2.46) is not affected by representation singularities.

2.3 ANGLE/AXIS ERROR

A different definition of orientation error can be obtained using an angle/axis representation. In view of (2.42), the mutual orientation between Σ_d and Σ_e is described by ${}^e \mathbf{R}_d$, and thus the orientation error can be defined in terms of the general expression

$${}^e \boldsymbol{o}_{de} = f(\vartheta_{de}) {}^e \boldsymbol{r}_{de}, \quad (2.50)$$

where ϑ_{de} and ${}^e\mathbf{r}_{de}$ are respectively the rotation and the unit vector corresponding to ${}^e\mathbf{R}_d$, and $f(\cdot)$ is a suitable scalar function with $f(0) = 0$. Common choices for $f(\vartheta)$ are summarized in Tab. 2.1.

Table 2.1. Common choices for $f(\vartheta)$.

Representation	$f(\vartheta)$
Classical angle/axis	$\sin(\vartheta)$
Quaternion	$\sin(\vartheta/2)$
Rodrigues parameters	$\tan(\vartheta/2)$
Simple rotation	ϑ

In the following, the classical angle/axis representation is adopted, while the quaternion will be treated in the next subsection. Hence, the *angle/axis error* is

$${}^e\mathbf{o}'_{de} = \sin(\vartheta_{de}) {}^e\mathbf{r}_{de} \quad (2.51)$$

which is usually referred to the base frame, i.e.

$$\mathbf{o}'_{de} = \mathbf{R}_e {}^e\mathbf{o}'_{de}. \quad (2.52)$$

A computational expression of \mathbf{o}'_{de} in terms of the rotation matrices of Σ_d and Σ_e can be derived in the form

$$\mathbf{o}'_{de} = \frac{1}{2} (\mathbf{S}(\mathbf{n}_e)\mathbf{n}_d + \mathbf{S}(\mathbf{s}_e)\mathbf{s}_d + \mathbf{S}(\mathbf{a}_e)\mathbf{a}_d). \quad (2.53)$$

The time derivative of the orientation error (2.53) can be related to the angular velocities of Σ_d and Σ_e as

$$\dot{\mathbf{o}}'_{de} = \mathbf{L}^T \boldsymbol{\omega}_d - \mathbf{L} \boldsymbol{\omega}_e \quad (2.54)$$

where

$$\mathbf{L} = -\frac{1}{2} (\mathbf{S}(\mathbf{n}_d)\mathbf{S}(\mathbf{n}_e) + \mathbf{S}(\mathbf{s}_d)\mathbf{S}(\mathbf{s}_e) + \mathbf{S}(\mathbf{a}_d)\mathbf{S}(\mathbf{a}_e)). \quad (2.55)$$

The second time derivative is

$$\ddot{\mathbf{o}}'_{de} = \mathbf{L}^T \dot{\boldsymbol{\omega}}_d + \dot{\mathbf{L}}^T \boldsymbol{\omega}_d - \mathbf{L} \dot{\boldsymbol{\omega}}_e - \dot{\mathbf{L}} \boldsymbol{\omega}_e. \quad (2.56)$$

The resolved angular acceleration can be chosen as

$$\mathbf{a}_o = \mathbf{L}^{-1} (\mathbf{L}^T \dot{\boldsymbol{\omega}}_d + \dot{\mathbf{L}}^T \boldsymbol{\omega}_d - \dot{\mathbf{L}} \boldsymbol{\omega}_e + \mathbf{K}_{Do} \dot{\mathbf{o}}'_{de} + \mathbf{K}_{Po} \mathbf{o}'_{de}), \quad (2.57)$$

where \mathbf{K}_{Do} and \mathbf{K}_{Po} are suitable feedback matrix gains, and \mathbf{L} is nonsingular provided that the angle ϑ_{de} belongs to the interval $(-\pi/2, \pi/2)$; it can be shown that this restriction is equivalent to the conditions $\mathbf{n}_e^T \mathbf{n}_d > 0$, $\mathbf{s}_e^T \mathbf{s}_d > 0$, $\mathbf{a}_e^T \mathbf{a}_d > 0$.

Substituting (2.57) into (2.31) gives the closed-loop dynamic behavior of the orientation error

$$\ddot{\mathbf{o}}'_{de} + \mathbf{K}_{Do} \dot{\mathbf{o}}'_{de} + \mathbf{K}_{Po} \mathbf{o}'_{de} = \mathbf{0}, \quad (2.58)$$

which is a linear and decoupled system analogous to the position error system (2.34) as well to the orientation error systems (2.41) and (2.49). Exponential stability is guaranteed for any choice of positive definite \mathbf{K}_{Do} and \mathbf{K}_{Po} ; convergence to $\mathbf{o}'_{de} = \mathbf{0}$ and $\dot{\mathbf{o}}'_{de} = \mathbf{0}$ is ensured, which in turn implies tracking of \mathbf{R}_d and $\boldsymbol{\omega}_d$.

Equation (2.57) reveals that the price to pay to obtain a linear and decoupled system is a large computational burden and the possible occurrence of a singularity. On the other hand, a simpler angle/axis scheme based on the error (2.53) can be devised where the resolved angular acceleration is chosen as

$$\mathbf{a}_o = \dot{\boldsymbol{\omega}}_d + \mathbf{K}_{Do} \Delta \boldsymbol{\omega}_{de} + \mathbf{K}_{Po} \mathbf{o}'_{de}. \quad (2.59)$$

In this case, the closed-loop dynamic behavior of the orientation error becomes

$$\Delta \dot{\boldsymbol{\omega}}_{de} + \mathbf{K}_{Do} \Delta \boldsymbol{\omega}_{de} + \mathbf{K}_{Po} \mathbf{o}'_{de} = \mathbf{0}. \quad (2.60)$$

Differently from all the previous cases (2.34), (2.41) and (2.49), the error system is nonlinear, and thus a Lyapunov argument is invoked below to ascertain its stability. To this purpose, in view of (A.29) and (A.30), the orientation error (2.51) can be expressed in terms of a quaternion as

$${}^e \mathbf{o}'_{de} = 2\eta_{de} {}^e \boldsymbol{\epsilon}_{de} \quad (2.61)$$

where $\{\eta_{de}, {}^e \boldsymbol{\epsilon}_{de}\}$ can be extracted from (2.42). Furthermore, the feedback gains are taken as scalar matrices, i.e. $\mathbf{K}_{Do} = k_{Do} \mathbf{I}$ and $\mathbf{K}_{Po} = k_{Po} \mathbf{I}$ where \mathbf{I} denotes the (3×3) identity matrix. Let

$$\mathcal{V} = 2k_{Po} {}^e \boldsymbol{\epsilon}_{de}^T {}^e \boldsymbol{\epsilon}_{de} + \frac{1}{2} \Delta \boldsymbol{\omega}_{de}^T \Delta \boldsymbol{\omega}_{de} \quad (2.62)$$

be a positive definite Lyapunov function candidate. The time derivative of (2.62) along the trajectories of system (2.60) is

$$\begin{aligned} \dot{\mathcal{V}} &= 4k_{Po} {}^e \boldsymbol{\epsilon}_{de}^T \dot{{}^e \boldsymbol{\epsilon}}_{de} + \Delta \boldsymbol{\omega}_{de}^T \Delta \dot{\boldsymbol{\omega}}_{de} \\ &= 2k_{Po} {}^e \boldsymbol{\epsilon}_{de}^T \mathbf{E}(\eta_{de}, {}^e \boldsymbol{\epsilon}_{de}) \Delta {}^e \boldsymbol{\omega}_{de} - k_{Do} \Delta \boldsymbol{\omega}_{de}^T \Delta \boldsymbol{\omega}_{de} - 2k_{Po} \eta_{de} \Delta {}^e \boldsymbol{\omega}_{de}^T {}^e \boldsymbol{\epsilon}_{de} \\ &= -k_{Do} \Delta \boldsymbol{\omega}_{de}^T \Delta \boldsymbol{\omega}_{de} \end{aligned} \quad (2.63)$$

where the propagation rule based on (A.46) and (A.47) has been exploited, i.e.

$$\dot{\eta}_{de} = -\frac{1}{2} {}^e\boldsymbol{\epsilon}_{de}^T \Delta {}^e\boldsymbol{\omega}_{de} \quad (2.64)$$

$${}^e\dot{\boldsymbol{\epsilon}}_{de} = \frac{1}{2} \mathbf{E}(\eta_{de}, {}^e\boldsymbol{\epsilon}_{de}) \Delta {}^e\boldsymbol{\omega}_{de} \quad (2.65)$$

with \mathbf{E} defined as in (A.38).

Since $\dot{\mathcal{V}}$ is only negative semi-definite, in view of LaSalle theorem, the system asymptotically converges to the invariant set described by the following equilibria:

$$\mathcal{E}_1 = \{\eta_{de} = 1, {}^e\boldsymbol{\epsilon}_{de} = \mathbf{0}, \Delta \boldsymbol{\omega}_{de} = \mathbf{0}\} \quad (2.66)$$

$$\mathcal{E}_2 = \{\eta_{de} = -1, {}^e\boldsymbol{\epsilon}_{de} = \mathbf{0}, \Delta \boldsymbol{\omega}_{de} = \mathbf{0}\} \quad (2.67)$$

$$\mathcal{E}_3 = \{\eta_{de} = 0, {}^e\boldsymbol{\epsilon}_{de} : \|{}^e\boldsymbol{\epsilon}_{de}\| = 1, \Delta \boldsymbol{\omega}_{de} = \mathbf{0}\}. \quad (2.68)$$

The equilibria in the set \mathcal{E}_3 are all unstable. To see this, consider (2.62) which, in view of (2.63), is a decreasing function. At any equilibrium in (2.68), it is

$$\mathcal{V}_\infty = 2k_{Po}. \quad (2.69)$$

Take a small perturbation $\eta_{de} = \sigma$ around such equilibrium; then, it is ${}^e\boldsymbol{\epsilon}_{de}^T {}^e\boldsymbol{\epsilon}_{de} = 1 - \sigma^2$. The perturbed Lyapunov function is

$$\mathcal{V}_\sigma = 2k_{Po} - 2\sigma^2 k_{Po} < \mathcal{V}_\infty \quad (2.70)$$

and thus, since (2.62) is decreasing, \mathcal{V} will never return to \mathcal{V}_∞ , implying that the equilibria in \mathcal{E}_3 are unstable. Therefore, the system asymptotically converges to either \mathcal{E}_1 or \mathcal{E}_2 ; since both quaternions for those equilibria represent the same orientation, it can be concluded that tracking of \mathbf{R}_d and $\boldsymbol{\omega}_d$ is achieved.

It is worth emphasizing that, compared to the previous angle/axis scheme based on (2.57), the restriction on ϑ_{de} does no longer hold. Nevertheless, for large values of ϑ_{de} , the angle/axis scheme based on (2.59) may lead to alignment of Σ_d and Σ_e with $\vartheta_{de} = \pm 2\pi$ as in the equilibrium \mathcal{E}_2 ; such occurrence is of no practical interest since ϑ_{de} is typically small for the tracking control at issue.

2.4 QUATERNION ERROR

A special type of angle/axis representation of the orientation error is obtained with the quaternion, i.e.

$$\mathbf{o}_{de}'' = \sin \frac{\vartheta_{de}}{2} {}^e\mathbf{r}_{de} = {}^e\boldsymbol{\epsilon}_{de} \quad (2.71)$$

corresponding to the vector part of the quaternion that can be extracted from the rotation matrix ${}^e\mathbf{R}_d$ in (2.42) (see (A.39)).

The relationship with the angular velocity error in (2.44) is established by (2.65).

The resolved angular acceleration based on the *quaternion error* can be chosen as

$$\dot{\boldsymbol{a}}_o = \dot{\boldsymbol{\omega}}_d + \mathbf{K}_{Do} \Delta \boldsymbol{\omega}_{de} + \mathbf{K}_{Po} \mathbf{R}_e^T \boldsymbol{\epsilon}_{de} \quad (2.72)$$

where \mathbf{K}_{Do} and \mathbf{K}_{Po} are suitable feedback matrix gains, and the orientation error has been referred to the base frame. Substituting (2.72) into (2.31) gives the closed-loop dynamic behavior of the orientation error

$$\Delta \dot{\boldsymbol{\omega}}_{de} + \mathbf{K}_{Do} \Delta \boldsymbol{\omega}_{de} + \mathbf{K}_{Po} \mathbf{R}_e^T \boldsymbol{\epsilon}_{de} = \mathbf{0}. \quad (2.73)$$

Similarly to the angle/axis case above, a Lyapunov argument is invoked below to ascertain stability of system (2.73). Again, the feedback gains are taken as scalar matrices, i.e. $\mathbf{K}_{Do} = k_{Do} \mathbf{I}$ and $\mathbf{K}_{Po} = k_{Po} \mathbf{I}$. Let

$$\mathcal{V} = k_{Po} \left((\eta_{de} - 1)^2 + {}^e \boldsymbol{\epsilon}_{de}^T {}^e \boldsymbol{\epsilon}_{de} \right) + \frac{1}{2} \Delta \boldsymbol{\omega}_{de}^T \Delta \boldsymbol{\omega}_{de} \quad (2.74)$$

be a positive definite Lyapunov function candidate. The time derivative of (2.74) along the trajectories of system (2.73) is

$$\begin{aligned} \dot{\mathcal{V}} &= 2k_{Po} \left((\eta_{de} - 1) \dot{\eta}_{de} + {}^e \boldsymbol{\epsilon}_{de}^T {}^e \dot{\boldsymbol{\epsilon}}_{de} \right) + \Delta \boldsymbol{\omega}_{de}^T \Delta \dot{\boldsymbol{\omega}}_{de} \\ &= k_{Po} \left(-(\eta_{de} - 1) {}^e \boldsymbol{\epsilon}_{de}^T \Delta {}^e \boldsymbol{\omega}_{de} + {}^e \boldsymbol{\epsilon}_{de}^T \mathbf{E}(\eta_{de}, {}^e \boldsymbol{\epsilon}_{de}) \Delta {}^e \boldsymbol{\omega}_{de} \right) \\ &\quad - k_{Do} \Delta \boldsymbol{\omega}_{de}^T \Delta \boldsymbol{\omega}_{de} - k_{Po} \Delta {}^e \boldsymbol{\omega}_{de}^T {}^e \boldsymbol{\epsilon}_{de} \\ &= -k_{Do} \Delta \boldsymbol{\omega}_{de}^T \Delta \boldsymbol{\omega}_{de} \end{aligned} \quad (2.75)$$

where (2.64) and (2.65) have been exploited.

Since $\dot{\mathcal{V}}$ is only negative semi-definite, in view of LaSalle theorem, the system asymptotically converges to the invariant set described by the two equilibria \mathcal{E}_1 and \mathcal{E}_2 in (2.66) and (2.67).

The equilibrium \mathcal{E}_2 is unstable. To see this, consider (2.74) which, in view of (2.75), is a decreasing function. At the equilibrium in (2.67), it is

$$\mathcal{V}_\infty = 4k_{Po}. \quad (2.76)$$

Take a small perturbation $\eta_{de} = -1 + \sigma$ around the equilibrium with $\sigma > 0$; then, it is ${}^e \boldsymbol{\epsilon}_{de}^T {}^e \boldsymbol{\epsilon}_{de} = 2\sigma - \sigma^2$. The perturbed Lyapunov function is

$$\mathcal{V}_\sigma = 4k_{Po} - 2\sigma k_{Po} < \mathcal{V}_\infty \quad (2.77)$$

and thus, since (2.74) is decreasing, \mathcal{V} will never return to \mathcal{V}_∞ , implying that \mathcal{E}_2 is unstable. Therefore, the system must asymptotically converge to \mathcal{E}_1 , which in turn implies that tracking of \mathbf{R}_d and $\boldsymbol{\omega}_d$ is achieved.

2.5 COMPUTATIONAL ISSUES

The features of the various control schemes can be further investigated from a computational viewpoint. Since the main differences reside in the way the orientation error is defined, the analysis can be focused on the issues regarding the computation of the resolved angular acceleration. In this respect, it is assumed that the robot manipulator is controlled in a real-time fashion, and thus the planning of the desired end-effector trajectory shall be updated on the basis of sensory information about the surrounding environment where the robot operates. Therefore, the two key elements in the analysis are the trajectory generation and the computation of the orientation error.

The most congenial way for the user to specify a desired orientation trajectory is the angle/axis method. Given the rotation matrices describing the initial and final orientation of Σ_d , the rotation matrix of the mutual orientation is computed; the angle and axis unit vector are extracted, and the orientation trajectory is interpolated from zero to the total angle while keeping the unit vector constant. This method provides the user with a meaningful interpretation of the end-effector orientation along the trajectory from a geometric viewpoint, and thus it is superior to the computationally lighter Euler angles method for which the intermediate orientations of Σ_d cannot be predicted in advance. On the other hand, assigning the angle and axis directly leads to specifying a desired trajectory in terms of a quaternion via (A.29) and (A.30). Upon these premises, it is assumed that the desired end-effector orientation trajectory is generated in terms of the rotation matrix \mathbf{R}_d via (A.21); then, the angular velocity ω_d and acceleration $\dot{\omega}_d$ are simply computed from the time derivatives of the interpolating polynomial for the angle.

Regarding the actual orientation of Σ_e , this is typically available from the direct kinematics equation in terms of the rotation matrix \mathbf{R}_e which can be computed from the joint position measurements via (2.3); further, the actual end-effector angular velocity ω_e can be computed from the joint velocity measurements via (2.5).

The computational burden of the schemes presented in the previous subsections has been evaluated in terms of the number of floating-point operations and transcendental functions needed to compute the resolved angular acceleration α_o . The angle/axis scheme based on (2.57) has been ruled out in view of its inherent computational complexity, and thus the scheme based on (2.59) has been considered hereafter. The results are reported in Tab. 2.2, where the additional computations needed for desired trajectory generation by those schemes not using \mathbf{R}_d , ω_d and $\dot{\omega}_d$ are evidenced; the computations have been optimized whenever possible, e.g. by avoiding multiplications by zero and carrying out partial factorizations.

It can be recognized that the extraction of Euler angles augments the overall load for both schemes, compared to the quaternion and the angle/axis scheme.

Table 2.2. Computational load of the angular part for the resolved acceleration control schemes.

Orientation error	Resolved acceleration		Trajectory generation	
	Flops	Funcs	Flops	Funcs
Classical Euler angles	68	8	52	8
Alternative Euler angles	136	8	0	0
Angle/axis	55	0	0	0
Quaternion	60	1	21	1

The interesting feature of the alternative Euler angles scheme is the absence of extra computations for trajectory generation, which instead penalizes the classical scheme due to the extraction of Euler angles from \mathbf{R}_d and the computation of their time derivatives. The computational load for the quaternion scheme is smaller than for the Euler angles schemes, even though an additional effort is required to compute the desired trajectory in terms of a quaternion. Not surprisingly, the angle/axis scheme is the most computationally efficient since it operates directly on the desired and actual rotation matrices, the desired and actual angular velocities, and the desired angular acceleration.

In conclusion, a critical discussion is in order concerning the pros and cons of each scheme.

At first sight, the classical Euler angles scheme might seem the simplest one in view of its similarity with the position scheme. Nevertheless, the analysis has revealed that, besides the heavy computational load due to Euler angles extraction, there is no guarantee to avoid the occurrence of representation singularities even when good end-effector orientation tracking is achieved. On the other hand, the effort to plan a singularity-free orientation trajectory is considerable especially when the angle/axis method is adopted for meaningful task specification purposes.

The alternative Euler angles scheme has the main merit to almost overcome the above drawback of representation singularities, since it keenly operates on the set of Euler angles which is extracted from a single rotation matrix describing the mutual orientation between Σ_d and Σ_e . It may suffer only in the case of large orientation errors, but there is no practical worry for a convergent algorithm with matched initial conditions between the desired and the actual end-effector orientation. A weakness, however, is that the computational burden is still considerable.

The breakthrough of the quaternion scheme stands in its applicability for any magnitude of the orientation error, since it is inherently based on a singularity-free representation of orientation. Its tracking performance is apparently as good as the alternative Euler angles scheme, although the closed-loop orientation error dynamics is nonlinear. A further advantage is represented by

the contained computational burden, even though the orientation error is not directly based on the desired and actual rotation matrices.

Finally, the angle/axis scheme has the least computational load among all the schemes. Its performance is worse than that of the quaternion scheme in the case of large orientation errors, whereas both schemes exhibit the same good behavior for small orientation errors.

2.6 REDUNDANCY RESOLUTION

In case the manipulator is kinematically redundant, there exist infinite joint motions that produce the same end-effector motion. In particular, even when the end effector is at rest, it is possible to generate an *internal motion* at the joints. As a minimal requirement, such motion should be made stable. In addition, it could be keenly utilized to meet additional task requirements besides the execution of the end-effector trajectory, thus providing *redundancy resolution*.

Redundancy can be solved either at kinematic level, that is in the first stage of a kinematic control strategy, or at dynamic level by suitably modifying the inverse dynamics control law. The latter approach is pursued hereafter since task space control is of interest in the present book.

Since the Jacobian matrix for a redundant manipulator has more columns than rows ($n > 6$), a suitable right inverse of \mathbf{J} is to be used in lieu of \mathbf{J}^{-1} . Hence, in lieu of (2.26), the new control input in (2.22) can be chosen as

$$\boldsymbol{\alpha} = \mathbf{J}^\dagger(\mathbf{q}) \left(\mathbf{a} - \dot{\mathbf{J}}(\mathbf{q})\dot{\mathbf{q}} \right) + \boldsymbol{\alpha}_n \quad (2.78)$$

where

$$\mathbf{J}^\dagger = \mathbf{W}^{-1} \mathbf{J}^T \left(\mathbf{J} \mathbf{W}^{-1} \mathbf{J}^T \right)^{-1} \quad (2.79)$$

denotes the right pseudo-inverse of \mathbf{J} weighted by the positive definite ($n \times n$) matrix \mathbf{W} . Also, in (2.78), $\boldsymbol{\alpha}_n$ denotes a joint acceleration vector lying in the null space of \mathbf{J} which is available for redundancy resolution. In fact, plugging (2.78) in (2.23) gives

$$\ddot{\mathbf{q}} = \mathbf{J}^\dagger(\mathbf{q}) \left(\mathbf{a} - \dot{\mathbf{J}}(\mathbf{q})\dot{\mathbf{q}} \right) + \boldsymbol{\alpha}_n. \quad (2.80)$$

Then, premultiplying both sides of (2.80) by \mathbf{J} , accounting for (2.25), and observing that $\mathbf{J}\mathbf{J}^\dagger = \mathbf{I}$, $\mathbf{J}\boldsymbol{\alpha}_n = \mathbf{0}$, yields the same end-effector resolved acceleration as in (2.27); \mathbf{I} denotes the ($n \times n$) identity matrix.

The matrix projecting arbitrary joint accelerations into the null space of \mathbf{J} is given by $(\mathbf{I} - \mathbf{J}^\dagger \mathbf{J})$, no matter what choice is made for the weighting matrix \mathbf{W} in (2.79). Therefore, it is significant to choose \mathbf{W} so that the redundancy resolution scheme for motion control should not be altered when interaction with the environment occurs. To this purpose, from (2.20) the joint

accelerations induced by the external end-effector force and moment are given by

$$\ddot{\mathbf{q}}_e = -\mathbf{B}^{-1}(\mathbf{q})\mathbf{J}^T(\mathbf{q})\mathbf{h}. \quad (2.81)$$

Projecting these accelerations in the null space of the Jacobian gives

$$\ddot{\mathbf{q}}_{en} = -\left(\mathbf{I} - \mathbf{J}^\dagger(\mathbf{q})\mathbf{J}(\mathbf{q})\right)\mathbf{B}^{-1}(\mathbf{q})\mathbf{J}^T(\mathbf{q})\mathbf{h}. \quad (2.82)$$

Choosing $\mathbf{W} = \mathbf{B}$ in (2.79) and plugging the resulting \mathbf{J}^\dagger in (2.82) yields $\ddot{\mathbf{q}}_{en} = \mathbf{0}$, meaning that the external force and moment produce no null space joint accelerations. Therefore, in view of this choice, in the design of the joint resolved acceleration in (2.78) the vector $\boldsymbol{\alpha}_n$ can be used to solve redundancy independently of the occurrence of interaction with the environment. The matrix

$$\mathbf{J}^\dagger = \mathbf{B}^{-1}\mathbf{J}^T\left(\mathbf{J}\mathbf{B}^{-1}\mathbf{J}^T\right)^{-1} \quad (2.83)$$

weighted by the inertia matrix is termed *dynamically consistent pseudo-inverse* of the Jacobian.

The next step consists of designing a redundancy resolution control in terms of the null space joint accelerations $\boldsymbol{\alpha}_n$ in (2.78). To this purpose, $\boldsymbol{\alpha}_n$ shall be chosen so as to ensure stabilization of the null space motion and possibly optimization of an additional task function. Let

$$\mathbf{e}_n = \left(\mathbf{I} - \mathbf{J}^\dagger(\mathbf{q})\mathbf{J}(\mathbf{q})\right)(\boldsymbol{\beta} - \dot{\mathbf{q}}) \quad (2.84)$$

denote the null space velocity error where $\boldsymbol{\beta}$ is a joint velocity vector which is available for redundancy resolution. The goal is to make \mathbf{e}_n asymptotically converge to zero. Taking the time derivative of (2.84) and using (2.80) gives the null space dynamics, i.e.

$$\dot{\mathbf{e}}_n = \left(\mathbf{I} - \mathbf{J}^\dagger(\mathbf{q})\mathbf{J}(\mathbf{q})\right)(\dot{\boldsymbol{\beta}} - \boldsymbol{\alpha}_n) - \left(\mathbf{J}^\dagger(\mathbf{q})\mathbf{J}(\mathbf{q}) + \mathbf{J}^\dagger(\mathbf{q})\dot{\mathbf{J}}(\mathbf{q})\right)(\boldsymbol{\beta} - \dot{\mathbf{q}}) \quad (2.85)$$

where $\dot{\mathbf{J}}^\dagger$ is a shortcut notation for the time derivative of \mathbf{J}^\dagger .

Consider the Lyapunov function candidate

$$\mathcal{V} = \frac{1}{2}\mathbf{e}_n^T\mathbf{B}(\mathbf{q})\mathbf{e}_n. \quad (2.86)$$

Computing the time derivative of (2.86) along the trajectories of system (2.85) yields

$$\dot{\mathcal{V}} = \frac{1}{2}\mathbf{e}_n^T\dot{\mathbf{B}}\mathbf{e}_n + \mathbf{e}_n^T\mathbf{B}\left(\dot{\boldsymbol{\beta}} - \boldsymbol{\alpha}_n - \dot{\mathbf{J}}^\dagger\mathbf{J}(\boldsymbol{\beta} - \dot{\mathbf{q}})\right), \quad (2.87)$$

where the dependence on \mathbf{q} has been dropped off, and the identity

$$\mathbf{e}_n^T\mathbf{B}\mathbf{J}^\dagger = \mathbf{0}^T \quad (2.88)$$

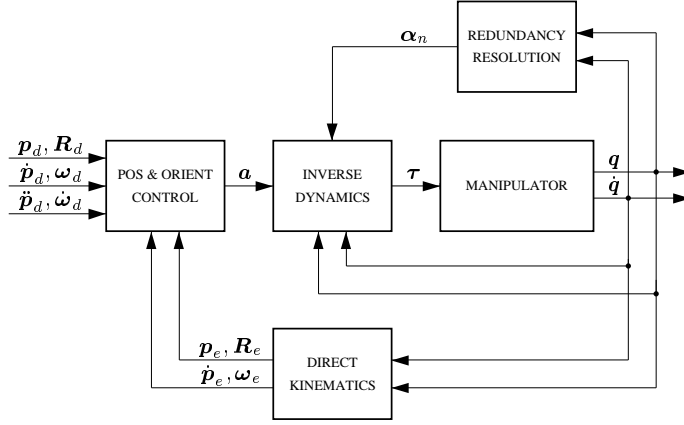


Figure 2.2. Inverse dynamics control with redundancy resolution.

has been exploited.

Choosing

$$\alpha_n = (\mathbf{I} - \mathbf{J}^\dagger \mathbf{J}) (\dot{\beta} - \mathbf{J}^\dagger \mathbf{J}(\beta - \dot{q}) + \mathbf{B}^{-1}(\mathbf{K}_n \mathbf{e}_n + \mathbf{C} \mathbf{e}_n)) \quad (2.89)$$

where \mathbf{K}_n is a positive definite matrix, and folding it into (2.87) gives

$$\dot{\mathcal{V}} = \frac{1}{2} \mathbf{e}_n^T (\dot{\mathbf{B}} - 2\mathbf{C}) \mathbf{e}_n - \mathbf{e}_n^T \mathbf{K}_n \mathbf{e}_n = -\mathbf{e}_n^T \mathbf{K}_n \mathbf{e}_n \leq 0 \quad (2.90)$$

thanks to (2.88) and the skew-symmetry of the matrix $\dot{\mathbf{B}} - 2\mathbf{C}$. Therefore, it can be concluded that the choice (2.89) gives a negative definite $\dot{\mathcal{V}}$, and thus $\mathbf{e}_n \rightarrow \mathbf{0}$ asymptotically.

Regarding the utilization of redundancy, a typical choice for β is

$$\beta = k_\beta \mathbf{B}^{-1} \left(\frac{\partial w(\mathbf{q})}{\partial \mathbf{q}} \right) \quad (2.91)$$

where k_β is a signed scalar and $w(\mathbf{q})$ is an additional task function that can be locally optimized.

A block diagram summarizing the overall inverse dynamics control with redundancy resolution is sketched in Fig. 2.2. The inverse dynamics control law gives τ as in (2.22) with α as in (2.78). The position and orientation control gives the resolved acceleration \mathbf{a} as in (2.29) with \mathbf{a}_p as in (2.33) and \mathbf{a}_o as any of (2.40), (2.48), (2.57), (2.59), (2.72). The direct kinematics gives the actual end-effector position and orientation as in (2.2) and (2.3), and the linear and angular velocity as in (2.4) and (2.5). Finally, the redundancy resolution scheme gives α_n as in (2.89) with β as in (2.91). Obviously, if no redundancy is available, then $\alpha_n = \mathbf{0}$ and the inverse dynamics control law (2.26) shall be used in lieu of (2.78).

3. REGULATION

For certain motion tasks, it can be sufficient to guarantee *regulation* of the end effector to a *constant* desired position \mathbf{p}_d and orientation \mathbf{R}_d . In such a case, simpler control laws can be adopted which do not require a full knowledge of the manipulator dynamic model, but just a *static model-based compensation*.

3.1 STATIC MODEL-BASED COMPENSATION

Mechanical intuition suggests that task space regulation can be achieved by designing a suitable control action which realizes an equivalent force and moment $\boldsymbol{\gamma}$ aimed at driving the end effector toward the desired position and orientation, i.e.

$$\boldsymbol{\tau} = \mathbf{J}^T(\mathbf{q})\boldsymbol{\gamma} - \mathbf{K}_D\dot{\mathbf{q}} + \mathbf{g}(\mathbf{q}), \quad (2.92)$$

where the matrix \mathbf{J}^T is needed to compute the resulting joint torques in a way analogous to (2.18) and the term \mathbf{g} is needed to compensate for the static torques due to gravity; also in (2.92), the derivative term $-\mathbf{K}_D\dot{\mathbf{q}}$, with \mathbf{K}_D an $(n \times n)$ positive definite matrix gain, provides additional damping torques at the joints which are expected to improve the transient behavior of the system. The control based on (2.92) is known as *proportional-derivative (PD) control with gravity compensation*.

Substituting (2.92) into (2.20) gives the closed-loop dynamic behavior of the system in the form

$$\mathbf{B}(\mathbf{q})\ddot{\mathbf{q}} + \mathbf{C}(\mathbf{q}, \dot{\mathbf{q}})\dot{\mathbf{q}} + (\mathbf{F} + \mathbf{K}_D)\dot{\mathbf{q}} = \mathbf{J}^T(\mathbf{q})\boldsymbol{\gamma}. \quad (2.93)$$

The stability of this system can be studied by introducing the following positive definite Lyapunov function candidate

$$\mathcal{V} = \frac{1}{2}\dot{\mathbf{q}}^T \mathbf{B}(\mathbf{q})\dot{\mathbf{q}} + \mathcal{U}_p + \mathcal{U}_o, \quad (2.94)$$

where the first term is the kinetic energy of the manipulator while the second and third terms are the potential energy associated respectively with a position error and an orientation error to be defined afterwards.

In view of the partition of \mathbf{h} in (2.19), it is appropriate to partition the vector $\boldsymbol{\gamma}$ into its force and moment components, i.e.

$$\boldsymbol{\gamma} = \begin{bmatrix} \boldsymbol{\gamma}_p \\ \boldsymbol{\gamma}_o \end{bmatrix} \quad (2.95)$$

where $\boldsymbol{\gamma}_p$ and $\boldsymbol{\gamma}_o$ are (3×1) vectors which shall be chosen so as to provide a position and an orientation control action, respectively.

The desired end-effector position is specified in terms of the *constant* position vector \mathbf{p}_d , whereas the desired end-effector orientation is specified in terms of the *constant* rotation matrix \mathbf{R}_d .

The *position control* can be chosen as a proportional action

$$\gamma_p = \mathbf{K}_{Pp} \Delta \mathbf{p}_{de} \quad (2.96)$$

where $\Delta \mathbf{p}_{de}$ is defined in (2.32) and \mathbf{K}_{Pp} is a suitable feedback matrix gain. Accordingly, the potential energy in (2.94) is

$$\mathcal{U}_p = \frac{1}{2} \Delta \mathbf{p}_{de}^T \mathbf{K}_{Pp} \Delta \mathbf{p}_{de}. \quad (2.97)$$

As regards the *orientation control*, this will also be chosen as a proportional action, but the actual expression will depend on the particular definition of end-effector orientation error chosen among those illustrated in the previous section.

3.2 ORIENTATION ERRORS

The natural counterpart of the position control in (2.96) is obtained when using the *Euler angles error* in (2.35) which leads to

$$\gamma_o = \mathbf{T}^{-T}(\varphi_e) \mathbf{K}_{Po} \Delta \varphi_{de} \quad (2.98)$$

where \mathbf{K}_{Po} is a suitable feedback matrix gain and \mathbf{T} is defined in (2.36). Accordingly, the potential energy in (2.94) is

$$\mathcal{U}_o = \frac{1}{2} \Delta \varphi_{de}^T \mathbf{K}_{Po} \Delta \varphi_{de}. \quad (2.99)$$

In view of (2.97) and (2.99), the time derivative of (2.94) along the trajectories of system (2.93) with (2.96) and (2.98) is

$$\dot{\mathcal{V}} = -\dot{\mathbf{q}}^T (\mathbf{F} + \mathbf{K}_D) \dot{\mathbf{q}}, \quad (2.100)$$

where (2.5) has been used together with the skew-symmetry of $\dot{\mathbf{B}} = 2\mathbf{C}$. Since $\dot{\mathcal{V}}$ is only negative semi-definite, in view of LaSalle theorem, the system asymptotically converges to the invariant set described by the equilibrium:

$$\mathcal{E} = \{\Delta \mathbf{p}_{de} = \mathbf{0}, \Delta \varphi_{de} = \mathbf{0}, \dot{\mathbf{q}} = \mathbf{0}\} \quad (2.101)$$

which is stable as long as no (kinematic or representation) singularity occurs.

For the *alternative Euler angles error* φ_{de} that can be extracted from (2.42), the orientation control action is

$$\gamma_o = \mathbf{T}_e^{-T}(\varphi_{de}) \mathbf{K}_{Po} \varphi_{de} \quad (2.102)$$

where \mathbf{T}_e is defined in (2.47). The stability of the equilibrium

$$\mathcal{E} = \{\Delta \mathbf{p}_{de} = \mathbf{0}, \varphi_{de} = \mathbf{0}, \dot{\mathbf{q}} = \mathbf{0}\} \quad (2.103)$$

can be proven in a formally analogous way to the above, by choosing the potential energy in (2.94) as

$$\mathcal{U}_o = \frac{1}{2} \boldsymbol{\varphi}_{de}^T \mathbf{K}_{Po} \boldsymbol{\varphi}_{de}. \quad (2.104)$$

For the *angle/axis error* \boldsymbol{o}'_{de} that can be computed as in (2.53), the orientation control action is

$$\boldsymbol{\gamma}_o = \mathbf{K}_{Po} \boldsymbol{o}'_{de} \quad (2.105)$$

with $\mathbf{K}_{Po} = k_{Po} \mathbf{I}$. The stability of the equilibrium

$$\mathcal{E} = \{\Delta \mathbf{p}_{de} = \mathbf{0}, \eta_{de} = 1, {}^e \boldsymbol{\epsilon}_{de} = \mathbf{0}, \dot{\mathbf{q}} = \mathbf{0}\} \quad (2.106)$$

can be proven in a formally analogous way to the above, by choosing the potential energy in (2.94) as

$$\mathcal{U}_o = 2k_{Po} {}^e \boldsymbol{\epsilon}_{de}^T {}^e \boldsymbol{\epsilon}_{de}, \quad (2.107)$$

while the equilibrium analysis is conceptually the same as in Subsection 2.3.

For the *quaternion error* ${}^e \boldsymbol{\epsilon}_{de}$ that can be extracted from (2.42), the orientation control action is

$$\boldsymbol{\gamma}_o = \mathbf{K}_{Po} \mathbf{R}_e {}^e \boldsymbol{\epsilon}_{de} \quad (2.108)$$

with $\mathbf{K}_{Po} = k_{Po} \mathbf{I}$. The stability of the equilibrium \mathcal{E} in (2.106) can be proven in a formally analogous way to the above, by choosing the potential energy in (2.94) as

$$\mathcal{U}_o = k_{Po} \left((\eta_{de} - 1)^2 + {}^e \boldsymbol{\epsilon}_{de}^T {}^e \boldsymbol{\epsilon}_{de} \right), \quad (2.109)$$

while the equilibrium analysis is conceptually the same as in Subsection 2.4.

4. FURTHER READING

Kinematic and dynamic modeling of rigid robot manipulators can be found in any classical robotics textbook, e.g. [81, 32, 38, 99, 116, 88, 6]. Identification of dynamic parameters needed by an inverse dynamics control was studied in [9, 58, 85]; the computation of a minimal set of dynamic parameters was considered in [45], while the dynamic model identified for the robot manipulator used in the experiment is reported in [16]. A complete treatment of model-based control is provided in [1], whereas advanced control schemes are covered in [23].

The original resolved acceleration control scheme dates back to [66] where an angle/axis error was used. Subsequent developments of the scheme are based on the work in [60]. The use of a quaternion error was proposed in [117] where a nonlinear closed-loop system for the orientation error was obtained; a linear closed-loop system was instead obtained in [59] at the expense of a more

involved choice of resolved angular acceleration. Further material about rigid body orientation can be found in classical mechanics textbook, e.g. [47, 86] as well as in an advanced robotics textbook [70]; a treatment of quaternion algebra is included in [30] while an algorithm for the extraction of a quaternion from a rotation matrix was given in [90]. The general problem of attitude control using quaternions was addressed in [107, 39]. Other representations of orientation for resolved acceleration control are discussed in [106], while a complete reformulation of resolved acceleration control based on different types of orientation errors was presented in [18], including the alternative Euler angles error which mitigates the effects of representation singularities.

A large body of literature is available on kinematic redundancy. The main techniques developed for redundant manipulators are described in [71]. The problem of solving redundancy at the acceleration level is discussed in [34]. The issue of stabilization of the internal motion was focused in [53]. The properties of the dynamically consistent pseudo-inverse of the manipulator Jacobian are analyzed in [43].

The PD control with gravity compensation has long constituted the simplest position control strategy for a robot manipulator. Its stability was keenly proven in the seminal work [100] where the passivity property of the dynamic model is fully exploited.

Chapter 3

INDIRECT FORCE CONTROL

The potential offered by motion control strategies to ensure a compliant behavior during the interaction between the end effector and the environment is investigated. Compliance control and impedance control are introduced as effective tools to achieve indirect control of the contact force. An inner motion loop is adopted to enhance disturbance rejection. Six-DOF impedance control schemes are derived using different types of orientation displacement and the properties of rotational stiffness are analyzed in detail. A generalization to the case of nondiagonal six-DOF stiffness is discussed. Throughout the chapter, experimental results are presented for an industrial robot interacting with the environment.

1. COMPLIANCE CONTROL

In order to gain insight into the problems arising at the interaction between the end effector and the environment, it is worth analyzing first the effects of a motion control strategy in the presence of a contact force and moment. In the previous chapter, it has been shown that a static model-based compensation control provides regulation to a desired end-effector position and orientation, while a dynamic model-based compensation control is needed to ensure accurate tracking of a desired end-effector trajectory. The two control schemes are reconsidered at the beginning of this chapter as useful tools to achieve an *indirect force control*, i.e. a control of the force (moment) through suitable actions on the position (orientation) error at the end effector.

For the sake of illustrating the useful concepts of *compliance* and *impedance*, the end-effector position and orientation is described by a (6×1) vector $\mathbf{x}_e = [\mathbf{p}_e^T \quad \boldsymbol{\varphi}_e^T]^T$, where the classical Euler angles representation of orientation has been selected in spite of its potential drawbacks concerned with representation singularities. Accordingly, the desired position and orientation is denoted as \mathbf{x}_d with obvious meaning of its components. As a consequence, the end-effector

error can be denoted as

$$\Delta \mathbf{x}_{de} = \begin{bmatrix} \Delta \mathbf{p}_{de} \\ \Delta \boldsymbol{\varphi}_{de} \end{bmatrix}. \quad (3.1)$$

It should be noticed that any of the other representations of orientation considered in the previous chapter leads to a (3×1) orientation error that can be used in lieu of $\Delta \boldsymbol{\varphi}_{de}$ in (3.1).

1.1 ACTIVE COMPLIANCE

In the case of a nonnull contact force and moment ($\mathbf{h} \neq \mathbf{0}$), the *static model-based compensation* control scheme in Section 3. of the previous chapter no longer ensures that the end effector reaches its desired position and orientation. In fact, by using the error in (3.1) and accounting for (2.96) and (2.98), the vector $\boldsymbol{\gamma}$ in (2.92) becomes

$$\boldsymbol{\gamma} = \mathbf{H}^{-T}(\boldsymbol{\varphi}_e) \mathbf{K}_P \Delta \mathbf{x}_{de} \quad (3.2)$$

where

$$\mathbf{K}_P = \begin{bmatrix} \mathbf{K}_{Pp} & \mathbf{O} \\ \mathbf{O} & \mathbf{K}_{Po} \end{bmatrix}. \quad (3.3)$$

and

$$\mathbf{H} = \begin{bmatrix} \mathbf{I} & \mathbf{O} \\ \mathbf{O} & \mathbf{T} \end{bmatrix}, \quad (3.4)$$

with \mathbf{T} in (2.36) and \mathbf{O} denoting the (3×3) null matrix. The steady state ($\dot{\mathbf{q}} = \mathbf{0}$, $\ddot{\mathbf{q}} = \mathbf{0}$) of the system (2.20) with (2.92) and (3.2) is

$$\mathbf{J}^T \mathbf{H}^{-T}(\boldsymbol{\varphi}_e) \mathbf{K}_P \Delta \mathbf{x}_{de} = \mathbf{J}^T \mathbf{h}. \quad (3.5)$$

On the assumption of a full-rank Jacobian, Equation (3.5) gives

$$\Delta \mathbf{x}_{de} = \mathbf{K}_P^{-1} \mathbf{H}^T(\boldsymbol{\varphi}_e) \mathbf{h}. \quad (3.6)$$

Equation (3.6) shows that at steady state the manipulator, under a proportional control action on the position and orientation error, behaves as a generalized spring in respect of the force and moment \mathbf{h} . Thus, the matrix \mathbf{K}_P^{-1} plays the role of an *active compliance*, meaning that it is possible to act on the elements of \mathbf{K}_P so as to ensure a compliant behavior during the interaction.

The selection of the elements of \mathbf{K}_P is not an easy task, since it is strongly affected by the characteristics of the environment. For a better understanding of interaction between the end effector and the environment it would be necessary to have an analytical description of the contact force and moment, which would be very demanding from a modeling viewpoint.

On the other hand, the partitions of \mathbf{K}_P in (3.3), $\Delta\mathbf{x}_{de}$ in (3.1) and \mathbf{h} in (2.19), as well as the expression of \mathbf{H} in (3.4), suggest separating Equation (3.6) into

$$\Delta\mathbf{p}_{de} = \mathbf{K}_{Pp}^{-1}\mathbf{f} \quad (3.7)$$

$$\Delta\varphi_{de} = \mathbf{K}_{Po}^{-1}\mathbf{T}^T(\varphi_e)\boldsymbol{\mu} \quad (3.8)$$

which allow analyzing the compliant behavior of the end-effector position separately from that of the end-effector orientation.

The presence of the matrix \mathbf{T} in (3.8) reveals that, even on the assumption of knowing the contact moment, the actual compliance for the end-effector orientation does depend not only on the choice of \mathbf{K}_{Po} but also on the choice of the particular set of Euler angles and in turn on the current manipulator configuration through the kinematics equation (2.3). Furthermore, the use of different orientation errors may bear noticeable implications as concerns the active compliance for the rotational part, and thus the analysis is deferred to Section 3.

Nonetheless, at this stage, it is worth analyzing the behavior for the translational part to acquire familiarity about how to act on the compliance for a given model of contact force. A real contact is a naturally distributed phenomenon in which the local characteristics of both the end effector and the environment are involved. In addition, friction effects between parts typically exist which greatly complicate the nature of the contact itself. A simplified analysis can be pursued by considering a frictionless and elastically compliant environment which is described by the model

$$\mathbf{f} = \mathbf{K}_f(\mathbf{p}_e - \mathbf{p}_o) \quad (3.9)$$

where \mathbf{p}_e is the end-effector position at the contact point, while \mathbf{p}_o is the rest position and \mathbf{K}_f is the (3×3) *contact stiffness* matrix of the environment.

With the environment model (3.9), Equation (3.7) becomes

$$\Delta\mathbf{p}_{de} = \mathbf{K}_{Pp}^{-1}\mathbf{K}_f(\mathbf{p}_e - \mathbf{p}_o); \quad (3.10)$$

thus, at steady state, the end-effector position is given by

$$\mathbf{p}_{e,\infty} = \left(\mathbf{I} + \mathbf{K}_{Pp}^{-1}\mathbf{K}_f \right)^{-1} \left(\mathbf{p}_d + \mathbf{K}_{Pp}^{-1}\mathbf{K}_f\mathbf{p}_o \right), \quad (3.11)$$

while the contact force can be found to be

$$\mathbf{f}_\infty = \left(\mathbf{I} + \mathbf{K}_f\mathbf{K}_{Pp}^{-1} \right)^{-1} \mathbf{K}_f(\mathbf{p}_d - \mathbf{p}_o). \quad (3.12)$$

Analysis of (3.11) shows that the steady-state position depends on the environment rest position as well as on the desired position imposed by the control

system to the end effector. The interaction of the two systems (environment and end effector) is influenced by the mutual weight of the respective compliance features. It is then possible to decrease the active compliance so that the end effector dominates the environment and vice versa. Such a dominance can be specified with reference to the single task directions, assuming that both \mathbf{K}_{Pp} and \mathbf{K}_f are diagonal. For a given contact stiffness, according to the prescribed interaction task, large values of the elements of \mathbf{K}_{Pp} are to be chosen for those directions along which the environment has to comply, whereas small values of the elements of \mathbf{K}_{Pp} are to be chosen for those directions along which the end effector has to comply.

Expression (3.12) gives the value of the contact force at steady state, which reveals that it may be appropriate to tune the end-effector compliance with the environment compliance along certain task directions. In fact, along a direction with high contact stiffness, it is better to have a compliant end effector so that it can taper the intensity of interaction through a suitable choice of the desired position. In this case, the end-effector steady-state position $\mathbf{p}_{e,\infty}$ practically coincides with the environment undeformed position \mathbf{p}_o . Hence, the end effector sustains the elastic force, depending on the corresponding elements of \mathbf{K}_P , that is determined by the choice of the component of $(\mathbf{p}_d - \mathbf{p}_o)$ along the relative direction. In the dual case of high environment compliance, if the end effector is made stiff, the steady-state position $\mathbf{p}_{e,\infty}$ is very close to the desired position \mathbf{p}_d . Hence, it is the environment to sustain the elastic force along the constrained task directions of interest.

In certain cases, it is possible to employ mechanical devices interposed between the manipulator end effector and the environment so as to change the *passive compliance* along particular task directions. For instance, in a peg-in-hole insertion task with a tight clearance, the peg axis would be required to line up almost exactly with the hole axis. If a discrepancy exists between the peg and the hole axes in either distance or direction, then the insertion cannot be accomplished, because of jamming or wedging. To accommodate the insertion, the gripper is provided with a device ensuring high stiffness along the insertion direction and high compliance along the other directions (*remote center of compliance*). The inconvenience of such devices is their low versatility to different operating conditions and generic interaction tasks, i.e. whenever a modification of the compliant mechanical hardware is required. On the other hand, with active compliance actions the control software can be easily modified so as to satisfy the requirements of different interaction tasks.

1.2 EXPERIMENTS

The above compliance control scheme has been tested in *experiments* on the six-joint industrial robot with open control architecture described in Section 3. of Chapter 1. The force sensor is not used for control but only for measurement

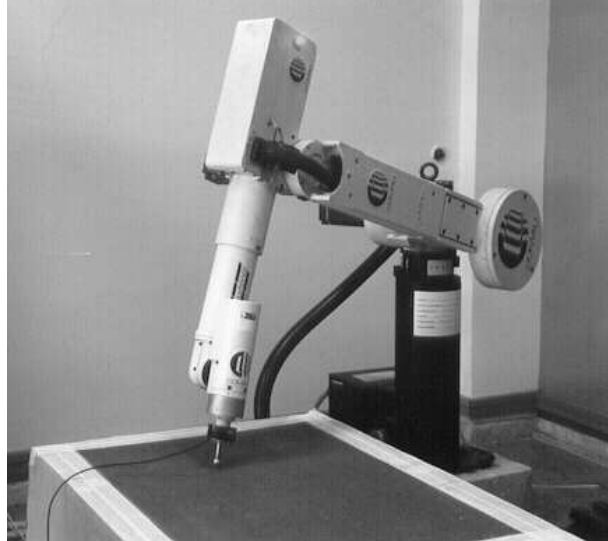


Figure 3.1. Robot end effector in contact with cardboard box.

of contact forces. The kinematic model and dynamic model of the robot manipulator are given in Appendix B.

Only the inner three joints are used while the outer three joints are mechanically braked. Hence $n = 3$ in (2.92) with $\mathbf{J} = \mathbf{J}_p$ and $\boldsymbol{\gamma} = \boldsymbol{\gamma}_p$. Accordingly, a three-DOF task is considered, involving end-effector position and linear force. The environment is constituted by a cardboard box, where the stiffness depends on the contact point and is about 10^4 N/m.

An end effector has been built as a stick with a sphere at the tip, both made of steel. A picture illustrating the robot with the wrist force sensor and the environment is given in Fig. 3.1.

Case Study. With reference to the base frame, the task consists of a straight-line motion in the Y_bZ_b -plane with an end-effector (horizontal) displacement of 0.25 m along Y_b and (vertical) displacement of -0.15 m along Z_b . The trajectory along the path is generated according to a trapezoidal velocity profile with cubic blends, and null initial and final velocities and accelerations, and a duration of 6 s. The surface of the cardboard box is nearly flat and has been placed (horizontally) in the X_bY_b -plane in such a way as to obstruct the desired end-effector motion. The gains of the control action in (2.96) and (2.92) have been set to $\mathbf{K}_{Pp} = 8000\mathbf{I}$ and $\mathbf{K}_D = 20\mathbf{I}$; note that \mathbf{K}_{Pp} has been chosen on the basis of a trade-off between position accuracy during the unconstrained motion and compliant behavior at the end effector (limited values of contact

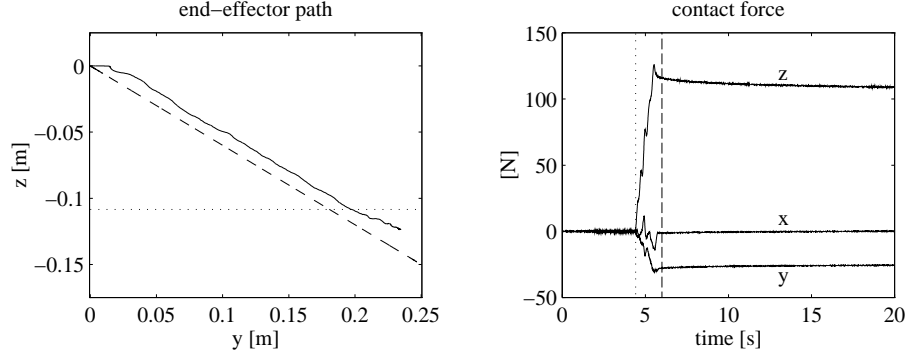


Figure 3.2. Experimental results under compliance control.

force) during the constrained motion, while \mathbf{K}_D has been chosen so as to guarantee a well-damped behavior.

The results are presented in Fig. 3.2 in terms of the desired (dashed) and the actual (solid) end-effector path, together with the time history of the contact force; in order to facilitate interpretation of the results, the approximate location (dotted) of the surface is illustrated on the plot of the end-effector path, while the instant of contact (dotted line) and the instant of the end of the motion trajectory (dashed line) are evidenced on the plot of the contact force.

It can be recognized that path tracking accuracy is rather poor during execution of the whole task. On the other hand, the contact force along Z_b reaches a steady-state value but its amount is rather large. Reduction of the contact force could be obtained by decreasing \mathbf{K}_{Pp} , at the expense of a larger end-effector position error though.

Finally, notice the presence of an appreciable value of contact force along Y_b at steady state due to contact friction, which indeed has not been modeled in the above analysis.

2. IMPEDANCE CONTROL

Compliance control is designed to achieve a desired static behavior of the interaction. In order to achieve a desired dynamic behavior, the actual mass and damping at the contact are to be considered besides the stiffness, leading to *impedance control*.

2.1 ACTIVE IMPEDANCE

In order to further investigate the interaction between the end effector and the environment, it is worth analyzing the performance of the *dynamic model-based compensation* control scheme in Section 2. of the previous chapter. The inverse dynamic control law (2.22) in the case of a nonnull contact force and

moment ($\mathbf{h} \neq \mathbf{0}$) leads to

$$\ddot{\mathbf{q}} = \boldsymbol{\alpha} - \mathbf{B}^{-1}(\mathbf{q}) \mathbf{J}^T(\mathbf{q}) \mathbf{h} \quad (3.13)$$

in lieu of (2.23). Equation (3.13) reveals the existence of a nonlinear coupling term due to the contact force and moment. The choice of $\boldsymbol{\alpha}$ as in (2.26) with \mathbf{a}_p as in (2.33) and \mathbf{a}_o as in (2.40) leads to

$$\Delta \ddot{\mathbf{x}}_{de} + \mathbf{K}_D \Delta \dot{\mathbf{x}}_{de} + \mathbf{K}_P \Delta \mathbf{x}_{de} = \mathbf{H}^{-1}(\boldsymbol{\varphi}_e) \mathbf{J}(\mathbf{q}) \mathbf{B}^{-1}(\mathbf{q}) \mathbf{J}^T(\mathbf{q}) \mathbf{h} \quad (3.14)$$

with $\Delta \mathbf{x}_{de}$ in (3.1), \mathbf{K}_P in (3.3), \mathbf{H} in (3.4) and

$$\mathbf{K}_D = \begin{bmatrix} \mathbf{K}_{Dp} & \mathbf{O} \\ \mathbf{O} & \mathbf{K}_{Do} \end{bmatrix}. \quad (3.15)$$

Equation (3.14) establishes a relationship through a generalized *active impedance* between the contact force and moment \mathbf{h} and the end-effector position and orientation error $\Delta \mathbf{x}_{de}$. This impedance can be attributed to a mechanical system characterized by a mass matrix

$$\mathbf{M} = \mathbf{J}^{-T} \mathbf{B} \mathbf{J}^{-1} \mathbf{H}, \quad (3.16)$$

a damping matrix $\mathbf{M} \mathbf{K}_D$ and a stiffness matrix $\mathbf{M} \mathbf{K}_P$, which allows specifying the dynamic behavior of the end effector.

The presence of \mathbf{M} makes the system coupled and nonlinear. If it is wished to keep linearity and decoupling during the interaction with the environment, it is necessary to measure the contact force and moment; this can be achieved by means of an appropriate *force/torque sensor* which is usually mounted at the manipulator wrist. Choosing

$$\boldsymbol{\tau} = \mathbf{B}(\mathbf{q}) \boldsymbol{\alpha} + \mathbf{C}(\mathbf{q}, \dot{\mathbf{q}}) \dot{\mathbf{q}} + \mathbf{F} \dot{\mathbf{q}} + \mathbf{g}(\mathbf{q}) + \mathbf{J}^T(\mathbf{q}) \mathbf{h} \quad (3.17)$$

with $\boldsymbol{\alpha}$ as in (2.26),

$$\mathbf{a}_p = \ddot{\mathbf{p}}_d + \mathbf{K}_{Mp}^{-1} (\mathbf{K}_{Dp} \Delta \dot{\mathbf{p}}_{de} + \mathbf{K}_{Pp} \Delta \mathbf{p}_{de} - \mathbf{f}) \quad (3.18)$$

$$\begin{aligned} \mathbf{a}_o = \mathbf{T}(\boldsymbol{\varphi}_e) (\ddot{\boldsymbol{\varphi}}_d + \mathbf{K}_{Mo}^{-1} (\mathbf{K}_{Do} \Delta \dot{\boldsymbol{\varphi}}_{de} + \mathbf{K}_{Po} \Delta \boldsymbol{\varphi}_{de} - \mathbf{T}^T(\boldsymbol{\varphi}_e) \boldsymbol{\mu})) \\ + \dot{\mathbf{T}}(\boldsymbol{\varphi}_e, \dot{\boldsymbol{\varphi}}_e) \dot{\boldsymbol{\varphi}}_e \end{aligned} \quad (3.19)$$

with \mathbf{K}_{Mp} and \mathbf{K}_{Mo} positive definite matrix gains, leads to

$$\mathbf{K}_{Mp} \Delta \ddot{\mathbf{p}}_{de} + \mathbf{K}_{Dp} \Delta \dot{\mathbf{p}}_{de} + \mathbf{K}_{Pp} \Delta \mathbf{p}_{de} = \mathbf{f} \quad (3.20)$$

$$\mathbf{K}_{Mo} \Delta \ddot{\boldsymbol{\varphi}}_{de} + \mathbf{K}_{Do} \Delta \dot{\boldsymbol{\varphi}}_{de} + \mathbf{K}_{Po} \Delta \boldsymbol{\varphi}_{de} = \mathbf{T}^T(\boldsymbol{\varphi}_e) \boldsymbol{\mu} \quad (3.21)$$

on the assumption of error-free force measurements.

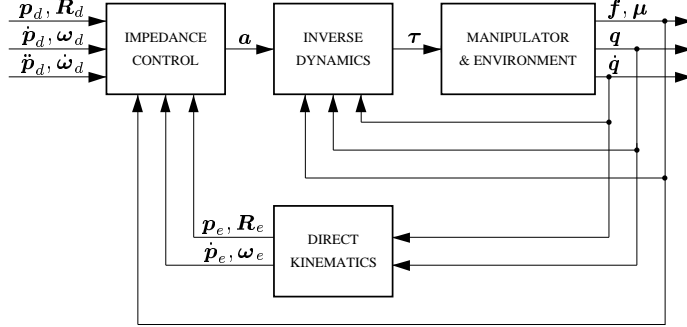


Figure 3.3. Impedance control.

It is worth noticing that the addition of the term $\mathbf{J}^T \mathbf{h}$ in (3.17) exactly compensates the contact force and moment and then it renders the end effector infinitely stiff with respect to the environment. In order to confer a compliant behavior at the end effector, the terms \mathbf{f} in (3.18) and $\mathbf{T}^T \boldsymbol{\mu}$ in (3.19) have been introduced which allow characterizing the end effector as a linear and decoupled impedance for both the translational part in (3.20) with regard to the contact force \mathbf{f} and the rotational part in (3.21) with regard to the equivalent contact moment $\mathbf{T}^T \boldsymbol{\mu}$.

The behavior of the system described by (3.20) and (3.21) at steady state is analogous to that described by (3.7) and (3.8); hence, the need for the matrix \mathbf{T}^T in (3.19); nonetheless, compared to the active compliance specified by \mathbf{K}_P^{-1} , now Equations (3.20) and (3.21) allow specifying the end-effector dynamics through a six-degree-of-freedom (six-DOF) impedance, where the translational impedance is specified by \mathbf{K}_{Mp} , \mathbf{K}_{Dp} and \mathbf{K}_{Pp} , and the rotational impedance is specified by \mathbf{K}_{Mo} , \mathbf{K}_{Do} and \mathbf{K}_{Po} .

As anticipated with the treatment of active compliance, the use of different orientation errors shall be studied in detail as concerns the rotational impedance.

A block diagram of the resulting impedance control is sketched in Fig. 3.3. With respect to the inverse dynamics scheme for motion control in Fig. 2.2, the position and orientation control is replaced with an impedance control which handles the measured contact force and moment and provides the resolved acceleration as in (3.18) and (3.19). Then, the inverse dynamics control law gives τ as in (3.17) with α as in (2.26). Redundancy resolution can be merely added to the scheme in Fig. 3.3 if wished, since the action of α_n is not influenced by the contact force and moment in view of the choice of \mathbf{J}^\dagger as in (2.83).

2.2 INNER MOTION CONTROL

The selection of good impedance parameters that guarantee a satisfactory compliant behavior during the interaction may turn out to be inadequate to en-

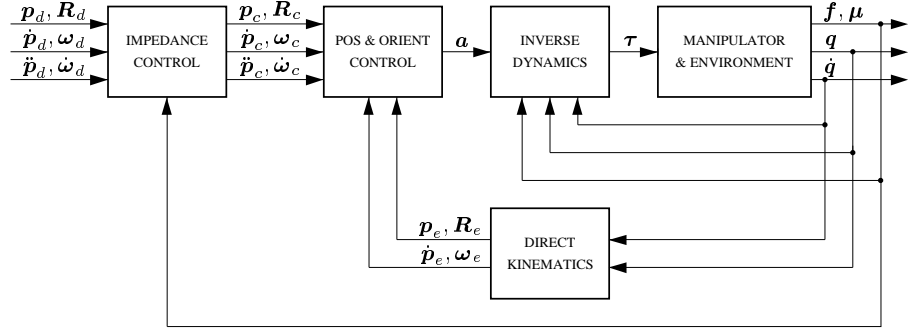


Figure 3.4. Impedance control with inner motion control loop.

sure accurate tracking of the desired position and orientation trajectory when the end effector moves in free space. In fact, by stacking the two equations (3.20) and (3.21) and accounting for the presence of a disturbance as in (2.28) yields

$$\mathbf{K}_M \Delta \ddot{\mathbf{x}}_{de} + \mathbf{K}_D \Delta \dot{\mathbf{x}}_{de} + \mathbf{K}_P \Delta \mathbf{x}_{de} = \mathbf{H}^T(\boldsymbol{\varphi}_e) \mathbf{h} + \mathbf{K}_M \mathbf{H}^{-1}(\boldsymbol{\varphi}_e) \mathbf{d} \quad (3.22)$$

with

$$\mathbf{K}_M = \begin{bmatrix} \mathbf{K}_{Mp} & \mathbf{O} \\ \mathbf{O} & \mathbf{K}_{Mo} \end{bmatrix}. \quad (3.23)$$

An effective *disturbance rejection*, at least at steady state, can be achieved by choosing a low weight for the matrix $\mathbf{K}_P^{-1} \mathbf{K}_M$ which corresponds to a stiff control action with an equivalent light mass at the end effector. Such a feature can eventually conflict with the desire of guaranteeing a compliant behavior when the end effector is in contact with a rather stiff environment.

A solution to this drawback can be devised by separating the motion control action from the impedance control action as follows. The motion control action is purposefully made stiff so as enhance *disturbance rejection* but, rather than ensuring tracking of the desired end-effector position and orientation, it shall ensure tracking of a reference position and orientation resulting from the impedance control action. In other words, the desired position and orientation together with the measured contact force and moment are input to the impedance equation which, via a suitable integration, generates the position and orientation to be used as a reference for the motion control action.

In order to realize the above solution, it is worth introducing a reference frame other than the desired frame specified by \mathbf{p}_d and \mathbf{R}_d . This frame is referred to as the *compliant frame* Σ_c , and is specified by a position vector \mathbf{p}_c and a rotation matrix \mathbf{R}_c . In this way, the inverse dynamics motion control strategy can be still adopted as long as the actual end-effector position \mathbf{p}_e and orientation \mathbf{R}_e is taken to coincide with \mathbf{p}_c and \mathbf{R}_c in lieu of \mathbf{p}_d and \mathbf{R}_d , respectively. Accordingly, the actual end-effector linear velocity $\dot{\mathbf{p}}_e$ and angular velocity $\boldsymbol{\omega}_e$ are taken to coincide with $\dot{\mathbf{p}}_c$ and $\boldsymbol{\omega}_c$, respectively.

A block diagram of the resulting scheme is sketched in Fig. 3.4 and reveals the presence of an *inner motion control* loop with respect to the outer impedance control loop.

The remainder of this chapter is devoted to analyze in detail the realization of an active impedance between the desired frame Σ_d and the compliant frame Σ_c for the translational part and the rotational part in lieu of the respective equations (3.20) and (3.21). The former is considered next leading to a three-DOF impedance control scheme.

2.3 THREE-DOF IMPEDANCE CONTROL

The mutual position between Σ_d and Σ_c can be described by the position displacement

$$\Delta\mathbf{p}_{dc} = \mathbf{p}_d - \mathbf{p}_c \quad (3.24)$$

which has been referred to the base frame.

In view (3.20), the *translational impedance* equation is chosen so as to enforce an equivalent mass-damper-spring behavior for the position displacement when the end effector exerts a force \mathbf{f} on the environment, i.e.

$$\mathbf{M}_p \Delta\ddot{\mathbf{p}}_{dc} + \mathbf{D}_p \Delta\dot{\mathbf{p}}_{dc} + \mathbf{K}_p \Delta\mathbf{p}_{dc} = \mathbf{f}, \quad (3.25)$$

where \mathbf{M}_p , \mathbf{D}_p and \mathbf{K}_p are positive definite matrices.

With reference to the scheme in Fig. 3.4, the *three-DOF impedance control* generates the reference position for the inner motion control. Therefore, in order to allow the implementation of the complete control scheme, the linear acceleration to be used in lieu of (3.18) shall be designed to track the position and the linear velocity of Σ_c , i.e.

$$\mathbf{a}_p = \ddot{\mathbf{p}}_c + \mathbf{K}_{Dp} \Delta\dot{\mathbf{p}}_{ce} + \mathbf{K}_{Pp} \Delta\mathbf{p}_{ce} \quad (3.26)$$

where

$$\Delta\mathbf{p}_{ce} = \mathbf{p}_c - \mathbf{p}_e \quad (3.27)$$

is the *position error* between Σ_c and Σ_e . Notice that \mathbf{p}_c and its associated derivatives can be computed by forward integration of the translational impedance equation (3.25) with input \mathbf{f} available from the force/torque sensor.

2.4 EXPERIMENTS

The above three-DOF impedance control schemes have been tested in *experiments* on the six-joint industrial robot where the first three joints are used, i.e. $n = 3$ in (3.17) with $\mathbf{J} = \mathbf{J}_p$ and $\mathbf{h} = \mathbf{f}$. Now, the force sensor is used for control. The environment is the same as described in Section 1.2.

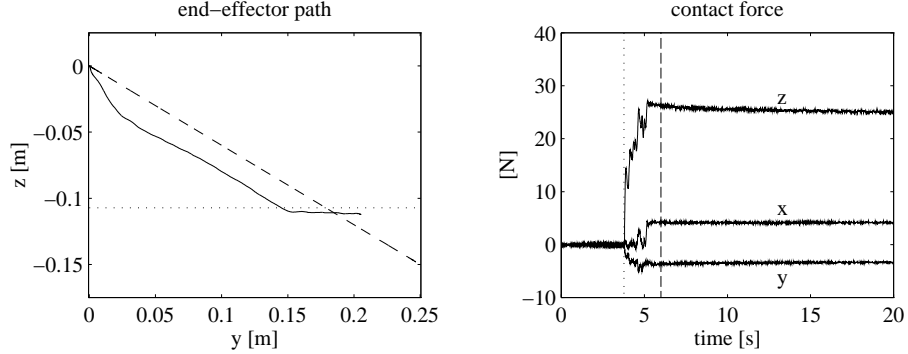


Figure 3.5. Experimental results under three-DOF impedance control.

First case study: Impedance control. The end effector has been placed in the same initial position as for the previous case study with the same trajectory. The impedance parameters in (3.18) have been set to $\mathbf{K}_{Mp} = 10\mathbf{I}$, $\mathbf{K}_{Dp} = 255\mathbf{I}$ and $\mathbf{K}_{Pp} = 500\mathbf{I}$, where the choice of \mathbf{K}_{Pp} is aimed at obtaining a value of the contact force along Z_b of approximately 20 N with the available estimate of the surface stiffness.

The results are presented in Fig. 3.5 in terms of the desired (dashed) and the actual (solid) end-effector path, together with the time history of the contact force. As above, the approximate location (dotted) of the surface is illustrated on the plot of the end-effector path, while the instant of contact (dotted line) and the instant of the end of the motion trajectory (dashed line) are evidenced on the plot of the contact force.

It can be recognized that path tracking accuracy is poor during execution of the whole task; this is imputable to the disturbance term on the right-hand side of (3.22). On the other hand, the contact force along Z_b is limited during the transient and reaches a constant value at steady state. Improvement of the position tracking accuracy might be achieved by increasing \mathbf{K}_{Pp} ; however, this would give rise to larger contact forces. Finally, notice the presence of an appreciable value of contact friction force along both X_b and Y_b at steady state which is caused by the end-effector position deviation along both X_b and Y_b (although the former is not visible in the figure).

Second case study: Impedance control with inner motion control. In order to carry out a fair comparison with the previous control scheme, the impedance parameters in (3.25) have been set to the same values as in the previous case study, i.e. $\mathbf{M}_p = 10\mathbf{I}$, $\mathbf{D}_p = 255\mathbf{I}$ and $\mathbf{K}_p = 500\mathbf{I}$, while the inner position loop gains in (3.26) have been set to $\mathbf{K}_{Dp} = 90\mathbf{I}$ and $\mathbf{K}_{Pp} = 2500\mathbf{I}$.

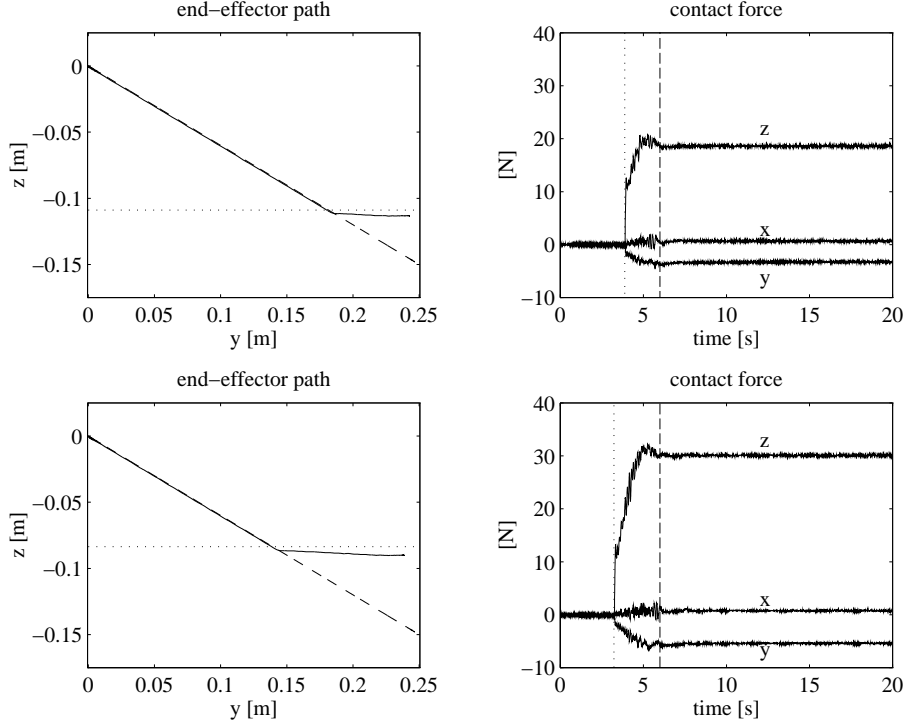


Figure 3.6. Experimental results under three-DOF impedance control with inner motion control.

The results are presented in the upper part of Fig. 3.6 in terms of the desired (dashed) and the actual (solid) end-effector path, together with the time history of the contact force. As above, the approximate location (dotted) of the surface is illustrated on the plot of the end-effector path, while the instant of contact (dotted line) and the instant of the end of the motion trajectory (dashed line) are evidenced on the plot of the contact force.

It can be recognized that path tracking accuracy is noticeably improved with respect to that obtained with the previous scheme and now is very good; this confirms the effective rejection of the disturbance thanks to the inner position loop.

On the other hand, the contact force along Z_b is still limited during the transient and reaches an approximate value of 20 N at steady state, as wished with the choice of K_p above. As before, an appreciable value of contact friction force along Y_b occurs that remains at steady state, while the good end-effector tracking accuracy essentially causes no contact friction along X_b by maintaining the motion in the Y_bZ_b -plane.

To investigate robustness of the scheme with respect to changes in the environment location, the task has been repeated with the same impedance parameters and inner position loop gains as before but the cardboard box was raised by about 0.025 m. From the results presented in the lower part of Fig. 3.6, it can be recognized that the imposed motion would require the end effector to penetrate into the surface by a larger amount, and thus the same value of \mathbf{K}_p gives rise to a different (larger in this case) contact force at steady state. It is worth noticing that the larger value of contact force yields larger contact friction as well.

3. SIX-DOF IMPEDANCE CONTROL

Equation (3.25) admits a nice physical interpretation when \mathbf{p}_d is constant, $\mathbf{M}_p = m_p \mathbf{I}$ and \mathbf{K}_p is symmetric. In this case, the first term represents the inertial force acting on a rigid body with mass m_p and kinetic energy

$$\mathcal{T}_p = \frac{1}{2} m_p \dot{\mathbf{p}}_c^T \dot{\mathbf{p}}_c. \quad (3.28)$$

The second term represents a dissipative damping force, while the last term represents the force exerted on the body by a three-dimensional spring with stiffness matrix \mathbf{K}_p , equilibrium position \mathbf{p}_d and potential energy

$$\mathcal{U}_p = \frac{1}{2} \Delta \mathbf{p}_{dc}^T \mathbf{K}_p \Delta \mathbf{p}_{dc}. \quad (3.29)$$

In order to ensure a proper end-effector behavior for the successful execution of an interaction task, the selection of the stiffness matrix plays a key role. Therefore, it is worth analyzing the elastic term from a geometric point of view.

The stiffness matrix \mathbf{K}_p can be decomposed as

$$\mathbf{K}_p = \mathbf{U}_p \boldsymbol{\Gamma}_p \mathbf{U}_p^T, \quad (3.30)$$

where $\boldsymbol{\Gamma}_p = \text{diag}\{\gamma_{p1}, \gamma_{p2}, \gamma_{p3}\}$ and $\mathbf{U}_p = [\mathbf{u}_{p1} \ \mathbf{u}_{p2} \ \mathbf{u}_{p3}]$ are respectively the eigenvalue matrix and the (orthogonal) eigenvector matrix. Then, considering a position displacement of length λ along the i -th eigenvector leads to an elastic force

$$\mathbf{f}_E = \mathbf{K}_p \Delta \mathbf{p}_{dc} = \gamma_{pi} \lambda \mathbf{u}_{pi} \quad (3.31)$$

which represents an elastic force along the same \mathbf{u}_{pi} axis. This implies that the translational stiffness matrix can be expressed in terms of three parameters γ_{pi} representing the stiffness along three principal axes \mathbf{u}_{pi} , and in turn it establishes the property of *task geometric consistency* for the elastic force in (3.31).

As far as the *rotational impedance* is concerned, the analysis depends on the particular type of representation for the orientation displacement between Σ_d and Σ_c . In the following subsections, the rotational impedance equation is

derived for the *Euler angles displacement*, the *angle/axis displacement* and the *quaternion displacement*, already introduced with reference to the motion control problem to express an end-effector orientation error.

3.1 EULER ANGLES DISPLACEMENT

In view of (3.21), the *rotational impedance* equation based on the classical *Euler angles displacement* is

$$\mathbf{M}_o \Delta \ddot{\varphi}_{dc} + \mathbf{D}_o \Delta \dot{\varphi}_{dc} + \mathbf{K}_o \Delta \varphi_{dc} = \mathbf{T}^T(\varphi_c) \boldsymbol{\mu}, \quad (3.32)$$

where \mathbf{M}_o , \mathbf{D}_o and \mathbf{K}_o are positive definite matrices describing the generalized inertia, rotational damping, rotational stiffness, respectively, and

$$\Delta \varphi_{dc} = \varphi_d - \varphi_c. \quad (3.33)$$

Notice that, differently from (3.25), the dynamic behavior for the rotational part is not absolutely determined by the choice of the impedance parameters but it does also depend on the orientation of the compliant frame with respect to the base frame through the matrix $\mathbf{T}^T(\varphi_c)$. Moreover, Equation (3.32) becomes ill-defined in the neighborhood of a representation singularity; in particular, at such a singularity, moment components in the null space of \mathbf{T}^T do not generate any contribution to the dynamics of the orientation displacement, leading to a possible build-up of large values of contact moment.

The effect of the rotational stiffness can be better understood by considering an infinitesimal orientation displacement between Σ_d and Σ_c . From (3.32), in the absence of representation singularities, the elastic moment is

$$\boldsymbol{\mu}_E = \mathbf{T}^{-T}(\varphi_c) \mathbf{K}_o \Delta \varphi_{dc}. \quad (3.34)$$

In the case of an infinitesimal orientation displacement about φ_c , it is

$$\begin{aligned} d(\Delta \varphi_{dc}) &= (\dot{\varphi}_d - \dot{\varphi}_c) \Big|_{\varphi_d = \varphi_c} dt \\ &= \mathbf{T}^{-1}(\varphi_c) \Delta \omega_{dc} dt, \end{aligned} \quad (3.35)$$

where $\Delta \omega_{dc} = \omega_d - \omega_c$ is the relative angular velocity between the two frames. Folding (3.35) into (3.34) written for an infinitesimal displacement $d(\Delta \varphi_{dc})$ gives

$$\boldsymbol{\mu}_E = \mathbf{T}^{-T}(\varphi_c) \mathbf{K}_o \mathbf{T}^{-1}(\varphi_c) \Delta \omega_{dc} dt. \quad (3.36)$$

Equation (3.36) reveals that the relationship between the orientation displacement and the elastic moment depends on the orientation of Σ_c . It follows that the property of *task geometric consistency* of the elastic force (3.31) is lost

when considering the elastic moment (3.34), that is, the eigenvectors of the matrix \mathbf{K}_o do not represent the three principal axes for the rotational stiffness.

The drawbacks discussed above can be mitigated by adopting the *alternative Euler angles displacement* φ_{dc} that can be extracted from the rotation matrix

$${}^c\mathbf{R}_d = \mathbf{R}_c^T \mathbf{R}_d. \quad (3.37)$$

Then, a *rotational impedance* at the end effector can be defined as

$$\mathbf{M}_o \ddot{\varphi}_{dc} + \mathbf{D}_o \dot{\varphi}_{dc} + \mathbf{K}_o \varphi_{dc} = \mathbf{T}^T(\varphi_{dc}) {}^c\boldsymbol{\mu} \quad (3.38)$$

where \mathbf{M}_o , \mathbf{D}_o and \mathbf{K}_o are defined in a similar way to (3.32) and ${}^c\boldsymbol{\mu}$ is referred to Σ_c .

An advantage with respect to (3.32) is that now the impedance behavior for the rotational part depends only on the relative orientation between Σ_d and Σ_c through the matrix $\mathbf{T}^T(\varphi_{dc})$. Hence, if XYZ Euler angles are adopted, representation singularities have a mitigated effect since they occur when $\beta_{dc} = \pm\pi/2$, i.e. for large end-effector orientation displacements.

From (3.38) the elastic moment is

$${}^c\boldsymbol{\mu}_E = \mathbf{T}^{-T}(\varphi_{dc}) \mathbf{K}_o \varphi_{dc}. \quad (3.39)$$

The infinitesimal orientation displacement about $\varphi_{dc} = \mathbf{0}$ is

$$\begin{aligned} d\varphi_{dc} &= \dot{\varphi}_{dc} \Big|_{\varphi_{dc} = \mathbf{0}} dt \\ &= \mathbf{T}^{-1}(\mathbf{0}) \Delta {}^c\boldsymbol{\omega}_{dc} dt. \end{aligned} \quad (3.40)$$

Folding (3.40) into (3.39) written for an infinitesimal displacement $d\varphi_{dc}$ gives

$$\begin{aligned} {}^c\boldsymbol{\mu}_E &= \mathbf{T}^{-T}(d\varphi_{dc}) \mathbf{K}_o \mathbf{T}^{-1}(\mathbf{0}) \Delta {}^c\boldsymbol{\omega}_{dc} dt \\ &\simeq \mathbf{T}^{-T}(\mathbf{0}) \mathbf{K}_o \mathbf{T}^{-1}(\mathbf{0}) \Delta {}^c\boldsymbol{\omega}_{dc} dt \end{aligned} \quad (3.41)$$

where the first-order approximation $\mathbf{T}^{-T}(d\varphi_{dc})dt \simeq \mathbf{T}^{-T}(\mathbf{0})dt$ has been made. Equation (3.41) reveals that the relationship between the orientation displacement and the elastic moment is independent of the orientation of Σ_c . Notice, however, that the choice of Euler angles affects the resulting stiffness through the matrix $\mathbf{T}(\mathbf{0})$ which must be invertible; as already emphasized in Subsection 2.2 of the previous chapter, the widely-adopted ZYZ representation of Euler angles cannot be used here, being singular right at $\varphi_{dc} = \mathbf{0}$ (see the matrix in (A.18))! It is convenient, instead, to adopt the XYZ representation which gives $\mathbf{T}(\mathbf{0}) = \mathbf{I}$ (see the matrix in (A.17)) and thus, for an infinitesimal displacement,

$${}^c\boldsymbol{\mu}_E \simeq \mathbf{K}_o \Delta {}^c\boldsymbol{\omega}_{dc} dt. \quad (3.42)$$

As regards the property of *task geometric consistency* for the elastic moment (3.39), when \mathbf{K}_o is a diagonal matrix and the XYZ representation of Euler angles is adopted, the i -th eigenvector \mathbf{u}_{oi} of $\mathbf{K}_o = \text{diag}\{\gamma_{o1}, \gamma_{o2}, \gamma_{o3}\}$ is the i -th column of the identity matrix. Hence, the orientation displacement of an angle ϑ_{dc} about \mathbf{u}_{oi} is described by

$$\boldsymbol{\varphi}_{dc} = \vartheta_{dc} \mathbf{u}_{oi} \quad (3.43)$$

which, in view of the expression of $\mathbf{T}(\boldsymbol{\varphi}_{dc})$ for XYZ Euler angles, leads to

$${}^c\boldsymbol{\mu}_E = \gamma_{oi} \vartheta_{dc} \mathbf{u}_{oi}, \quad (3.44)$$

representing an elastic moment about the same \mathbf{u}_{oi} axis; thus the vectors \mathbf{u}_{oi} have the meaning of rotational stiffness principal axes. It can be easily recognized that the same property does not hold in general for a nondiagonal \mathbf{K}_o .

Equations (3.32) or (3.38) define the dynamic behavior between Σ_d and Σ_c in terms of a rotational impedance. Therefore, in order to allow the implementation of the complete *six-DOF impedance control* with inner motion loop in Fig. 3.4, the angular acceleration \boldsymbol{a}_o shall be designed to track the orientation and angular velocity of Σ_c .

With reference to the *Euler angles error* used in (2.40), the angular acceleration is taken as

$$\boldsymbol{a}_o = \mathbf{T}(\boldsymbol{\varphi}_e) (\ddot{\boldsymbol{\varphi}}_c + \mathbf{K}_{Do} \Delta \dot{\boldsymbol{\varphi}}_{ce} + \mathbf{K}_{Po} \Delta \boldsymbol{\varphi}_{ce}) + \dot{\mathbf{T}}(\boldsymbol{\varphi}_e, \dot{\boldsymbol{\varphi}}_e) \dot{\boldsymbol{\varphi}}_e \quad (3.45)$$

where

$$\Delta \boldsymbol{\varphi}_{ce} = \boldsymbol{\varphi}_c - \boldsymbol{\varphi}_e \quad (3.46)$$

is the orientation error between Σ_c and Σ_e . Notice that $\boldsymbol{\varphi}_c$ and its associated derivatives can be computed by forward integration of the rotational impedance equation (3.32) with input $\boldsymbol{\mu}$ available from the force/torque sensor.

On the other hand, with reference to the *alternative Euler angles error* used in (2.48), the angular acceleration is taken as

$$\begin{aligned} \boldsymbol{a}_o = & \dot{\boldsymbol{\omega}}_d - \dot{\mathbf{T}}_e(\boldsymbol{\varphi}_{de}, \dot{\boldsymbol{\varphi}}_{de}) \dot{\boldsymbol{\varphi}}_{de} \\ & - \mathbf{T}_e(\boldsymbol{\varphi}_{de}) (\ddot{\boldsymbol{\varphi}}_{dc} + \mathbf{K}_{Do}(\dot{\boldsymbol{\varphi}}_{dc} - \dot{\boldsymbol{\varphi}}_{de}) + \mathbf{K}_{Po}(\boldsymbol{\varphi}_{dc} - \boldsymbol{\varphi}_{de})) \end{aligned} \quad (3.47)$$

where the orientation control acts as to take $\boldsymbol{\varphi}_{de}$ to coincide with $\boldsymbol{\varphi}_{dc}$ which ultimately implies that Σ_e is aligned with Σ_c . Notice that $\boldsymbol{\varphi}_{dc}$ and its associated derivatives can be computed by forward integration of the rotational impedance equation (3.38).

3.2 ANGLE/AXIS DISPLACEMENT

A class of geometrically meaningful representations of the mutual orientation between Σ_d and Σ_c can be given in terms of the *angle/axis displacement*

$${}^c\boldsymbol{o}_{dc} = f(\vartheta_{dc}) {}^c\boldsymbol{r}_{dc}, \quad (3.48)$$

where ϑ_{dc} and ${}^c\mathbf{r}_{dc}$ correspond to ${}^c\mathbf{R}_d$, and $f(\vartheta_{dc})$ is any of the functions listed in Tab. 2.1. Those are strictly increasing smooth functions in an interval $(-\vartheta_M, \vartheta_M)$ with $\vartheta_M > 0$. Hence, the derivative $f'(\vartheta_{dc})$ of f with respect to ϑ_{dc} is strictly positive in that interval.

From (A.10) the angular velocity of Σ_d relative to Σ_c is given by

$$\Delta {}^c\boldsymbol{\omega}_{dc} = {}^c\boldsymbol{\omega}_d - {}^c\boldsymbol{\omega}_c = \mathbf{R}_c^T (\boldsymbol{\omega}_d - \boldsymbol{\omega}_c). \quad (3.49)$$

Differentiating (3.48), and using (A.26) and (A.27), gives

$${}^c\dot{\boldsymbol{\omega}}_{dc} = \boldsymbol{\Omega}({}^c\mathbf{r}_{dc}, \vartheta_{dc}) \Delta {}^c\boldsymbol{\omega}_{dc} \quad (3.50)$$

where

$$\boldsymbol{\Omega} = \boldsymbol{\Omega}_{\parallel} + \boldsymbol{\Omega}_{-} \quad (3.51)$$

with

$$\boldsymbol{\Omega}_{\parallel} = f'(\vartheta_{dc}) {}^c\mathbf{r}_{dc} {}^c\mathbf{r}_{dc}^T \quad (3.52)$$

$$\boldsymbol{\Omega}_{-} = \frac{1}{2} f(\vartheta_{dc}) \left(\cot(\vartheta_{dc}/2) (\mathbf{I} - {}^c\mathbf{r}_{dc} {}^c\mathbf{r}_{dc}^T) - \mathbf{S}({}^c\mathbf{r}_{dc}) \right). \quad (3.53)$$

The matrix $\boldsymbol{\Omega}_{\parallel}$ ($\boldsymbol{\Omega}_{-}$) projects the relative angular velocity $\Delta {}^c\boldsymbol{\omega}_{dc}$ in a direction parallel (orthogonal) to ${}^c\mathbf{o}_{dc}$. Also, notice that the following property of $\boldsymbol{\Omega}$ holds

$$\boldsymbol{\Omega}({}^c\mathbf{r}_{dc}, 0) = f'(0) \mathbf{I} \quad (3.54)$$

which will be useful in the following.

In order to derive the impedance equation for the rotational part, it is convenient to refer to the following energy-based argument. Let

$$\mathcal{T}_o = \frac{1}{2} \Delta {}^c\boldsymbol{\omega}_{dc}^T \mathbf{M}_o \Delta {}^c\boldsymbol{\omega}_{dc} \quad (3.55)$$

express the rotational kinetic energy of a rigid body with inertia tensor \mathbf{M}_o and angular velocity $\Delta {}^c\boldsymbol{\omega}_{dc}$. It is worth pointing out that, from a rigorous physical viewpoint, \mathcal{T}_o is representative of a pseudo-kinetic energy since it is defined in terms of a relative velocity. Nonetheless, it should be clear that, if the orientation of Σ_d is constant, then it would attain the meaning of a true kinetic energy. Then consider the potential energy

$$\mathcal{U}_o = \psi {}^c\mathbf{o}_{dc}^T \mathbf{K}_o {}^c\mathbf{o}_{dc}, \quad (3.56)$$

where ψ is a positive constant depending on the particular choice of $f(\cdot)$, and \mathbf{K}_o is a symmetric positive definite matrix.

Having defined the various energy contributions, the terms in the rotational impedance equation can be derived by considering the associated powers.

Taking the time derivative of (3.55) yields

$$\dot{\mathcal{T}}_o = {}^c\boldsymbol{\mu}_I^T \Delta {}^c\boldsymbol{\omega}_{dc} \quad (3.57)$$

where

$${}^c\boldsymbol{\mu}_I = \mathbf{M}_o \Delta {}^c\dot{\boldsymbol{\omega}}_{dc} \quad (3.58)$$

is the inertial moment and $\Delta {}^c\dot{\boldsymbol{\omega}}_{dc}$ denotes the time derivative of $\Delta {}^c\boldsymbol{\omega}_{dc}$ in (3.49). Further, taking the time derivative of (3.56) and accounting for (3.50) yields

$$\dot{\mathcal{U}}_o = {}^c\boldsymbol{\mu}_E^T \Delta {}^c\boldsymbol{\omega}_{dc} \quad (3.59)$$

where

$${}^c\boldsymbol{\mu}_E = 2\psi \boldsymbol{\Omega}^T ({}^c\mathbf{r}_{dc}, \vartheta_{dc}) \mathbf{K}_o {}^c\boldsymbol{\omega}_{dc} \quad (3.60)$$

is the elastic moment.

Finally, a dissipative contribution can be added as

$${}^c\boldsymbol{\mu}_D = \mathbf{D}_o \Delta {}^c\boldsymbol{\omega}_{dc}, \quad (3.61)$$

where \mathbf{D}_o is a positive definite matrix characterizing a rotational damping at the end effector.

Therefore, a *rotational impedance* at the end effector can be defined by adding the contributions (3.58), (3.61) and (3.60), i.e.

$$\mathbf{M}_o \Delta {}^c\dot{\boldsymbol{\omega}}_{dc} + \mathbf{D}_o \Delta {}^c\boldsymbol{\omega}_{dc} + \mathbf{K}'_o {}^c\boldsymbol{\omega}_{dc} = {}^c\boldsymbol{\mu}, \quad (3.62)$$

where the equality ${}^c\boldsymbol{\mu} = {}^c\boldsymbol{\mu}_I + {}^c\boldsymbol{\mu}_D + {}^c\boldsymbol{\mu}_E$ has been imposed, and

$$\mathbf{K}'_o = 2\psi \boldsymbol{\Omega}^T ({}^c\mathbf{r}_{dc}, \vartheta_{dc}) \mathbf{K}_o. \quad (3.63)$$

Notice that the rotational part of the impedance equation has been derived in terms of quantities all referred to Σ_c ; this allows the impedance behavior to be effectively expressed in terms of the relative orientation between Σ_d and Σ_c , no matter what the absolute orientation of the compliant frame with respect to the base frame is.

It is worth remarking that, by adopting an angle/axis representation of the orientation and pursuing an energy-based argument, the contributions in the rotational impedance equation correspond to physically meaningful energy terms; also, the velocity used is dual to the moment $\boldsymbol{\mu}$ exerted by the end effector, i.e. with no need of a transformation matrix depending on the actual end-effector orientation.

In the following, the analysis for small orientation displacements is carried out and consistency with the task geometry is investigated.

Consider an infinitesimal orientation displacement expressed as

$$\begin{aligned} d^c \boldsymbol{o}_{dc} &= {}^c \dot{\boldsymbol{o}}_{dc} \Big|_{\vartheta_{dc} = 0} dt \\ &= \boldsymbol{\Omega}({}^c \boldsymbol{r}_{dc}, 0) \Delta^c \boldsymbol{\omega}_{dc} dt \\ &= f'(0) \Delta^c \boldsymbol{\omega}_{dc} dt \end{aligned} \quad (3.64)$$

where the property (3.54) has been exploited. Folding (3.64) into (3.60), written for an infinitesimal displacement about $\vartheta_{dc} = 0$, gives

$$\begin{aligned} {}^c \boldsymbol{\mu}_E &= 2\psi \boldsymbol{\Omega}^T({}^c \boldsymbol{r}_{dc}, d\vartheta_{dc}) \boldsymbol{K}_o d^c \boldsymbol{o}_{dc} \\ &\simeq 2\psi (f'(0))^2 \boldsymbol{K}_o \Delta^c \boldsymbol{\omega}_{dc} dt \\ &= \boldsymbol{K}_o \Delta^c \boldsymbol{\omega}_{dc} dt, \end{aligned} \quad (3.65)$$

where the first-order approximation $\boldsymbol{\Omega}({}^c \boldsymbol{r}_{dc}, d\vartheta_{dc}) \simeq f'(0) \boldsymbol{I}$ has been considered and the choice $\psi = 1/2(f'(0))^2$ has been made. Equation (3.65) clearly shows how the relationship between the orientation displacement and the elastic moment is independent of the orientation of Σ_c , and the problem of representation singularities is not of concern since $f'(0)$ is finite.

As regards the property of *task geometric consistency*, the stiffness matrix in (3.60) can be decomposed as

$$\boldsymbol{K}_o = \boldsymbol{U}_o \boldsymbol{\Gamma}_o \boldsymbol{U}_o^T \quad (3.66)$$

where $\boldsymbol{\Gamma}_o = \text{diag}\{\gamma_{o1}, \gamma_{o2}, \gamma_{o3}\}$ and $\boldsymbol{U}_o = [\boldsymbol{u}_{o1} \quad \boldsymbol{u}_{o2} \quad \boldsymbol{u}_{o3}]$ are respectively the eigenvalue matrix and the (orthogonal) eigenvector matrix. Then, considering an orientation displacement by an angle ϑ_{dc} about the i -th eigenvector

$$\boldsymbol{o}_{dc}^c = f(\vartheta_{dc}) \boldsymbol{u}_{oi}, \quad (3.67)$$

and taking into account the decomposition of $\boldsymbol{\Omega}$ into the two terms (3.52) and (3.53) yields

$${}^c \boldsymbol{\mu}_E = 2\psi \boldsymbol{\Omega}_{||}^T(\boldsymbol{u}_{oi}, \vartheta_{dc}) \gamma_{oi} f(\vartheta_{dc}) \boldsymbol{u}_{oi} = 2\psi f'(\vartheta_{dc}) f(\vartheta_{dc}) \gamma_{oi} \boldsymbol{u}_{oi}. \quad (3.68)$$

This represents an elastic moment about the same \boldsymbol{u}_{oi} axis which is in the same direction of the orientation displacement since $f'(\vartheta_{dc}) > 0$. Therefore, the rotational stiffness matrix can be expressed in terms of three parameters γ_{oi} representing the stiffness about three principal axes \boldsymbol{u}_{oi} , i.e. in a consistent way with the task geometry.

For the implementation of the inner motion loop in Fig. 3.4, with reference to the *angle/axis error* used in (2.59), the angular acceleration is taken as

$$\boldsymbol{a}_o = \dot{\boldsymbol{\omega}}_c + \boldsymbol{K}_{Do} \Delta \boldsymbol{\omega}_{ce} + \boldsymbol{K}_{Po} \boldsymbol{o}'_{ce} \quad (3.69)$$

where

$$\mathbf{o}'_{ce} = \frac{1}{2} (\mathbf{S}(\mathbf{n}_e)\mathbf{n}_c + \mathbf{S}(\mathbf{s}_e)\mathbf{s}_c + \mathbf{S}(\mathbf{a}_e)\mathbf{a}_c) \quad (3.70)$$

where \mathbf{n}_c , \mathbf{s}_c , \mathbf{a}_c are the column of the matrix \mathbf{R}_c which can be computed by forward integration of the rotational impedance equation (3.62).

3.3 QUATERNION DISPLACEMENT

With reference to the different angle/axis representations of orientation displacement in Table 2.1, a special case is constituted by the *quaternion displacement*. Such a representation has the advantage over other angle/axis representations to avoid representation singularities.

The mutual orientation between Σ_d and Σ_c can be described by the quaternion $\{\eta_{dc}, {}^c\epsilon_{dc}\}$ extracted from ${}^c\mathbf{R}_d$. Indeed, the orientation displacement to be considered in (3.62) is given by the vector part ${}^c\epsilon_{dc}$ and, in view of (3.56), the expression of the potential energy becomes

$$\mathcal{U}_o = 2 {}^c\epsilon_{dc}^T \mathbf{K}_o {}^c\epsilon_{dc}, \quad (3.71)$$

where it has been set $\psi = 2$. Even though the potential energy is expressed in terms of the vector part of the quaternion, it can be shown that \mathcal{U}_o coincides with the rotational elastic energy associated with a torsional spring of stiffness \mathbf{K}_o acting so as to align Σ_c with Σ_d .

In view of (3.62), the resulting impedance equation for the rotational part becomes

$$\mathbf{M}_o \Delta {}^c\dot{\omega}_{dc} + \mathbf{D}_o \Delta {}^c\omega_{dc} + \mathbf{K}'_o {}^c\epsilon_{dc} = {}^c\mu, \quad (3.72)$$

where the rotational stiffness matrix is

$$\mathbf{K}'_o = 2 \mathbf{E}^T(\eta_{dc}, {}^c\epsilon_{dc}) \mathbf{K}_o \quad (3.73)$$

with \mathbf{E} as in (A.38).

In the case of free motion, it is worth finding the equilibria of the rotational impedance equation (3.72). These should occur whenever Σ_d and Σ_c are aligned.

Consider the Hamiltonian contribution

$$\mathcal{H}_o = \mathcal{T}_o + \mathcal{U}_o, \quad (3.74)$$

associated with the rotational motion, which is a positive definite function. Taking the time derivative of (3.74) and accounting for (3.55) and (3.56) along with (3.72) and (3.73) yields

$$\dot{\mathcal{H}}_o = -\Delta {}^c\omega_{dc}^T \mathbf{D}_o \Delta {}^c\omega_{dc} + {}^c\mu^T \Delta {}^c\omega_{dc}. \quad (3.75)$$

If ${}^c\boldsymbol{\mu} = \mathbf{0}$, $\dot{\mathcal{H}}_o$ in (3.75) vanishes if and only if $\Delta {}^c\boldsymbol{\omega}_{dc} = \mathbf{0}$; hence from (3.72) it follows that ${}^c\boldsymbol{\epsilon}_{dc}$ asymptotically tends to the invariant set described by

$${}^c\boldsymbol{\mu}_E = 2(\eta_{dc}\mathbf{K}_o {}^c\boldsymbol{\epsilon}_{dc} + \mathbf{S}({}^c\boldsymbol{\epsilon}_{dc})\mathbf{K}_o {}^c\boldsymbol{\epsilon}_{dc}) = \mathbf{0} \quad (3.76)$$

where (3.73) has been exploited.

By observing that the two terms in (3.76) are mutually orthogonal, the following sets of equilibria are found:

$$\mathcal{E}_1 = \{\eta_{dc} = \pm 1, {}^c\boldsymbol{\epsilon}_{dc} = \mathbf{0}, \Delta {}^c\boldsymbol{\omega}_{dc} = \mathbf{0}\} \quad (3.77)$$

$$\mathcal{E}_2 = \{\eta_{dc} = 0, {}^c\boldsymbol{\epsilon}_{dc}: \mathbf{K}_o {}^c\boldsymbol{\epsilon}_{dc} = \gamma_{oi} {}^c\boldsymbol{\epsilon}_{dc}, \|{}^c\boldsymbol{\epsilon}_{dc}\| = 1, \Delta {}^c\boldsymbol{\omega}_{dc} = \mathbf{0}\} \quad (3.78)$$

where $\gamma_{oi} > 0$ denotes an eigenvalue of matrix \mathbf{K}_o .

The equilibria in \mathcal{E}_2 are unstable. To see this, consider the Hamiltonian contribution (3.74) which, in view of (3.75), is a decreasing function. At any of the equilibria in (3.78), it is

$$\mathcal{H}_{o,\infty} = 2\gamma_{oi} {}^c\boldsymbol{\epsilon}_{dc}^T {}^c\boldsymbol{\epsilon}_{dc} = 2\gamma_{oi} \quad (3.79)$$

where (A.31) has been used. Consider a small perturbation around the equilibrium with $\eta_{dc} = \sigma$, ${}^c\boldsymbol{\epsilon}_{dc}$ such that ${}^c\boldsymbol{\epsilon}_{dc}^T {}^c\boldsymbol{\epsilon}_{dc} = 1 - \sigma^2$, $\Delta {}^c\boldsymbol{\omega}_{dc} = \mathbf{0}$ and $\mathbf{K}_o {}^c\boldsymbol{\epsilon}_{dc} = \gamma_{oi} {}^c\boldsymbol{\epsilon}_{dc}$. The perturbed Hamiltonian contribution is

$$\mathcal{H}_{o,\sigma} = 2\gamma_{oi}(1 - \sigma^2) < \mathcal{H}_{o,\infty} \quad (3.80)$$

and thus, since (3.74) is decreasing, \mathcal{H}_o will never return to $\mathcal{H}_{o,\infty}$, implying that those equilibria are all unstable. Notice that, at such equilibria, Σ_d is anti-aligned with Σ_c with respect to the axis of the mutual rotation ${}^c\mathbf{R}_d$ between the two frames.

It can be concluded that ${}^c\boldsymbol{\epsilon}_{dc}$ must converge to \mathcal{E}_1 . Interestingly enough, the two equilibria in \mathcal{E}_1 both give the same mutual orientation ${}^c\mathbf{R}_d = \mathbf{I}$, thus implying the alignment of Σ_d with Σ_c , so as wished.

For the implementation of the inner motion loop in Fig. 3.4, with reference to the *quaternion error* used in (2.72), the angular acceleration is taken as

$$\boldsymbol{a}_o = \dot{\boldsymbol{\omega}}_c + \mathbf{K}_{Do}\Delta\boldsymbol{\omega}_{ce} + \mathbf{K}_{Po}\mathbf{R}_e {}^e\boldsymbol{\epsilon}_{ce}. \quad (3.81)$$

Notice that \mathbf{R}_c , $\boldsymbol{\omega}_c$ and $\dot{\boldsymbol{\omega}}_c$ can be computed by forward integration of the rotational impedance equation (3.72).

3.4 EXPERIMENTS

The above impedance control schemes have been tested in a number of *experiments* on the six-joint and the seven-joint industrial robots with open control architecture described in Section 3. of Chapter 1 and force/torque

sensor. The kinematic model and dynamic model of the seven-joint robot manipulator are given in Appendix B

An end effector has been built as a steel stick with a wooden disk of 5.5 cm radius at the tip. The end-effector frame has its origin at the center of the disk and its approach axis normal to the disk surface and pointing outwards.

The performance of the quaternion-based six-DOF impedance control has been compared with that of the two six-DOF impedance control schemes based on Euler angles. An analysis of the computational burden for the three control schemes based on (3.17), (2.26), (3.26) and (3.25) has been carried out for the available hardware, leading to a total time of: 0.264 ms for the impedance control using (3.45) and (3.32), 0.230 ms for the impedance control using (3.47) and (3.38), and 0.195 ms for the impedance control using (3.81) and (3.72). Details on the computational load in terms of floating-point operations and transcendental functions number are given in Table 3.1.

Table 3.1. Computational load for the three six-DOF impedance control schemes.

Orientation error	Flops	Funcs
Classical Euler angles	1420	30
Alternative Euler angles	1467	24
Quaternion	1429	15

First case study: Interaction with environment. The first case study has been developed to analyze *interaction with environment*. This is constituted by a flat plexiglas surface. The translational stiffness at the contact between the end effector and the surface is of the order of 10^4 N/m, while the rotational stiffness for small angles is of the order of 20 Nm/rad.

The task consists of taking the disk in contact with the surface at an angle of unknown magnitude (Fig. 3.7). The end-effector desired position is required to make a straight-line motion with a vertical displacement of -0.24 m along the Z_b -axis of the base frame. The trajectory along the path is generated according to a fifth-order interpolating polynomial with null initial and final velocities and accelerations, and a duration of 7 s. The end-effector desired orientation is required to remain constant during the task. The surface is placed (horizontally) in the X_bY_b -plane in such a way as to obstruct the desired end-effector motion, both for the translational part and for the rotational part.

The parameters of the translational part of the six-DOF impedance equation (3.25) have been set to $\mathbf{M}_p = 9\mathbf{I}$, $\mathbf{D}_p = 2000\mathbf{I}$, $\mathbf{K}_p = 700\mathbf{I}$, while the parameters of the rotational part of the six-DOF impedance equation (3.72) have been set to $\mathbf{M}_o = 0.4\mathbf{I}$, $\mathbf{D}_o = 5\mathbf{I}$, $\mathbf{K}_o = 2\mathbf{I}$. Notice that the stiffness matrices have been chosen so as to ensure a compliant behavior at the end

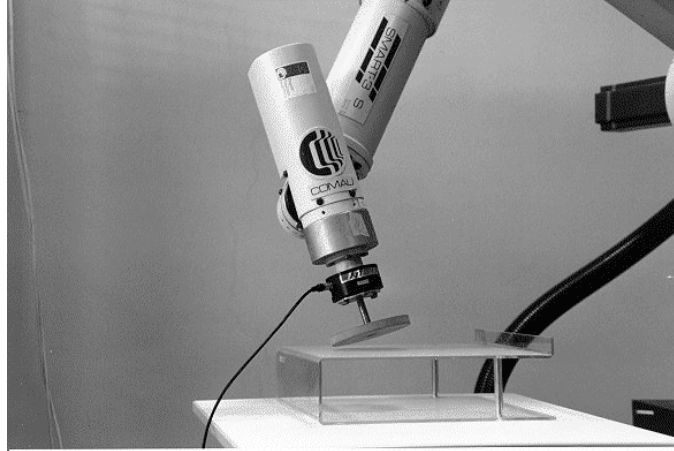


Figure 3.7. End effector in contact with plexiglas surface.

effector (limited values of contact force and moment) during the constrained motion, while the damping matrices have been chosen so as to guarantee a well-damped behavior.

The gains of the inner motion control loop actions in (3.26) and (3.81) have been set to $\mathbf{K}_{Pp} = 2025\mathbf{I}$, $\mathbf{K}_{Po} = 4500\mathbf{I}$, $\mathbf{K}_{Dp} = \mathbf{K}_{Do} = 65\mathbf{I}$.

The results in Fig. 3.8 show the effectiveness of the quaternion-based six-DOF impedance control. After the contact, the component of the position error between Σ_d and Σ_e $\Delta\mathbf{p}_{de} = \mathbf{p}_d - \mathbf{p}_e$ along the Z_b -axis significantly deviates from zero, as expected, while small errors can be seen also for the components along the X_b - and the Y_b -axis due to contact friction. As for the orientation error, all the components of the orientation displacement between Σ_d and Σ_e ${}^e\epsilon_{de}$ significantly deviate from zero since the end-effector frame has to rotate with respect to the base frame after the contact in order to comply with the surface. Also, in view of the imposed task, a prevailing component of the contact force can be observed along the Z_b -axis after the contact, while the small components along the X_b - and the Y_b -axis arise as a consequence of the above end-effector deviation. As for the contact moment referred to Σ_d , the component about the Z_b -axis is small, as expected. It can be recognized that all the above quantities reach constant steady-state values after the desired motion is stopped. The oscillations on the force and moment during the transient can be mainly ascribed to slipping of the disk on the surface after the contact.

In sum, it can be asserted that a compliant behavior is successfully achieved. A similar performance has been obtained also with the six-DOF impedance control schemes based on the Euler angles error, i.e. by using either (3.32) or (3.38) in lieu of (3.72). This fact can be explained because both the absolute

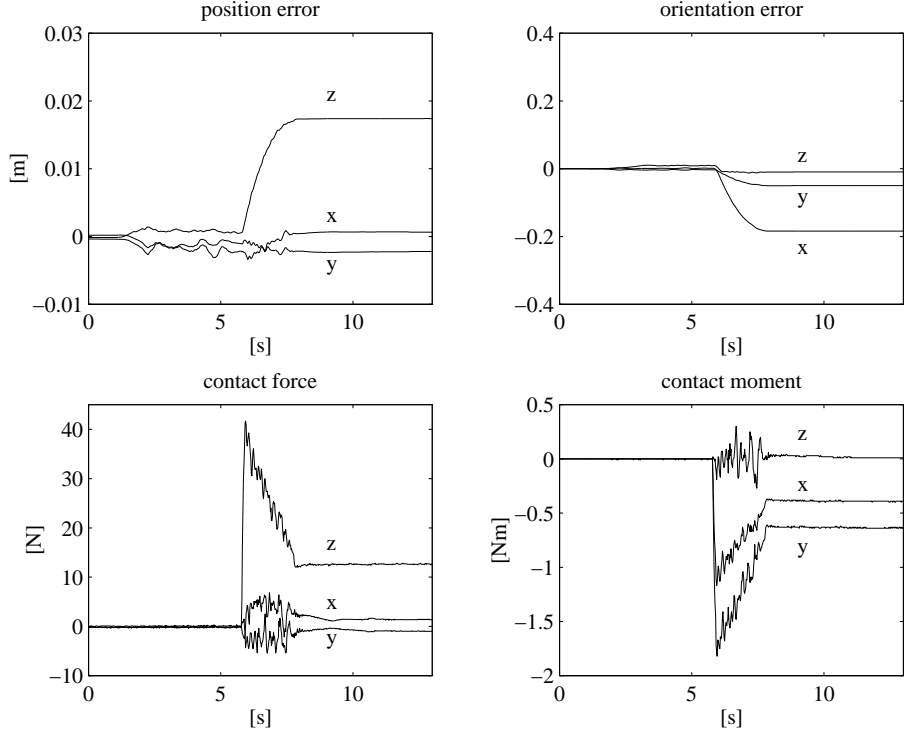


Figure 3.8. Experimental results under six-DOF impedance control based on quaternion in the first case study.

end-effector orientation in (3.32) and the relative orientation in (3.38) keep far from representation singularities. The results are not reported here for brevity.

Second case study: Representation singularity. The second case study is aimed at testing the performance of the quaternion-based six-DOF impedance control when the end-effector orientation is close to a *representation singularity* of \mathbf{T} . The end effector and the surface are the same as in the previous case study.

The end-effector desired position is required to make a straight-line motion with a horizontal displacement of 0.085 m along the X_b -axis of the base frame. The trajectory along the path is generated according to a fifth-order interpolating polynomial with null initial and final velocities and accelerations, and a duration of 5 s. The end-effector desired orientation is required to remain constant during the task. The surface is now placed vertically in such a way as to obstruct the desired end-effector motion, only for the rotational part though. Therefore, no impedance control has been accomplished for the translational part, i.e. \mathbf{p}_c in (3.26) coincides with \mathbf{p}_d .

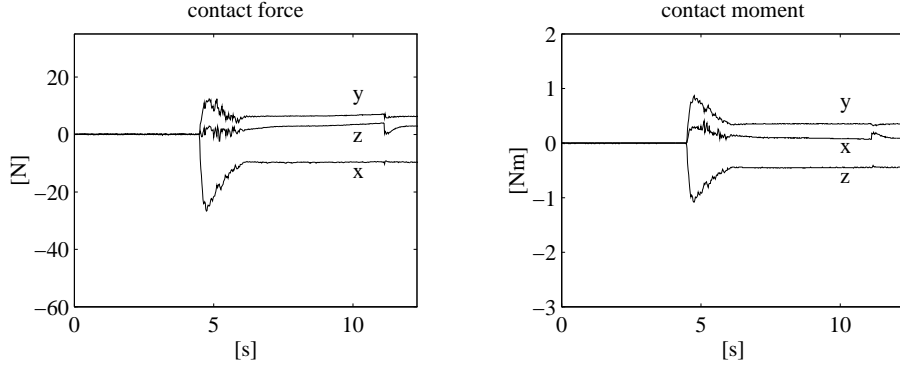


Figure 3.9. Experimental results under six-DOF impedance control based on quaternion in the second case study.

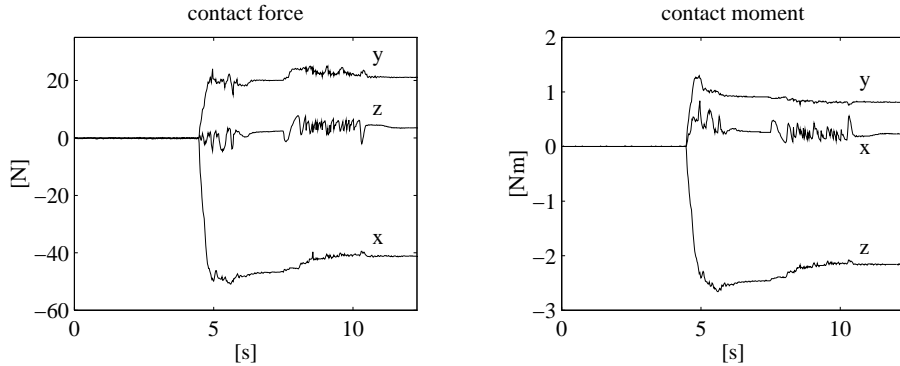


Figure 3.10. Experimental results under six-DOF impedance control based on the classical Euler angles in the second case study.

The parameters of the quaternion-based impedance equations (3.25) and (3.72) are set to $\mathbf{M}_p = 10\mathbf{I}$, $\mathbf{D}_p = 600\mathbf{I}$, $\mathbf{K}_p = 1000\mathbf{I}$, $\mathbf{M}_o = 0.25\mathbf{I}$, $\mathbf{D}_o = 3.5\mathbf{I}$, $\mathbf{K}_o = 2.5\mathbf{I}$. In order to carry out a comparison, the impedance control based on the Euler angles has also been tested. The parameters of the rotational impedance equation (3.32) have been set to the same values as for the quaternion. As regards the gains of the inner motion control loop, these have been chosen equal to those in the previous experiment for both types of impedance control schemes.

The results in Figs. 3.9 and 3.10 show the significant differences occurring in the performance of the two schemes. For the impedance control based on (3.32), large values of contact force and moment are generated since the rotational impedance equation suffers from ill-conditioning of the matrix $\mathbf{T}(\varphi_c)$; this phenomenon is not present for the quaternion-based impedance control based

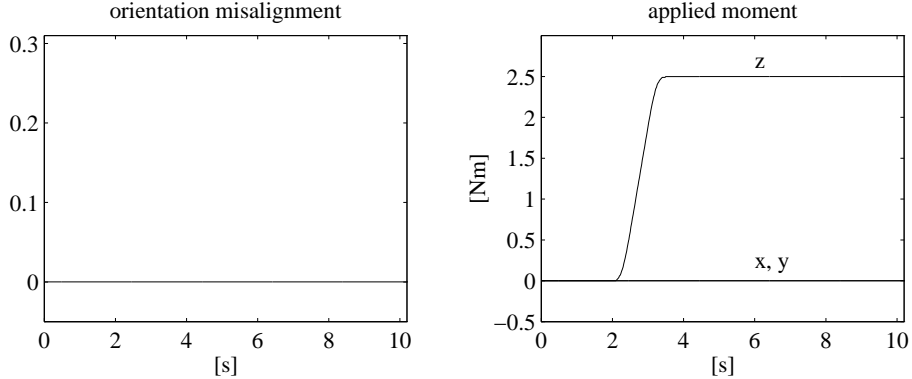


Figure 3.11. Experimental results under six-DOF impedance control based on quaternion in the third case study.

on (3.72) since representation singularities are not involved in the rotational impedance equation. On the other hand, testing of the impedance control based on the alternative Euler angles in (3.38) has revealed a performance as good as the quaternion-based impedance control, since the orientation displacement φ_{dc} is kept far from a representation singularity. Hence, the results are not reported here for brevity.

In sum it can be concluded that both the impedance control based on the alternative Euler angles and the quaternion-based impedance control perform better than the impedance control based on the classical Euler angles, as far as interaction with the environment is concerned.

Third case study: Task geometric consistency. Another case study has been developed to analyze *task geometric consistency* when an external moment is applied at the end effector. The quaternion-based impedance control and the impedance control based on Euler angles have been tested.

The stiffness matrices of the rotational part of the impedance equations (3.72) and (3.32) have been taken as diagonal matrices; \mathbf{K}_o has been chosen as in (3.66) with $\mathbf{U}_o = \mathbf{I}$ and $\mathbf{\Gamma}_o = 2.5\mathbf{I}$ for both schemes. The remaining parameters of the rotational impedance have been set to $\mathbf{M}_o = 0.25\mathbf{I}$ and $\mathbf{D}_o = 1.5\mathbf{I}$ for both schemes. No impedance control has been accomplished for the translational part. The gains of the inner motion control loop have been chosen equal to those in the previous case study.

The position and orientation of the desired frame are required to remain constant, and a torque is applied about the approach axis of Σ_d ; the torque is taken from zero to 2.5 Nm according to a linear interpolating polynomial with 4th-order blends and a total duration of 1 s.

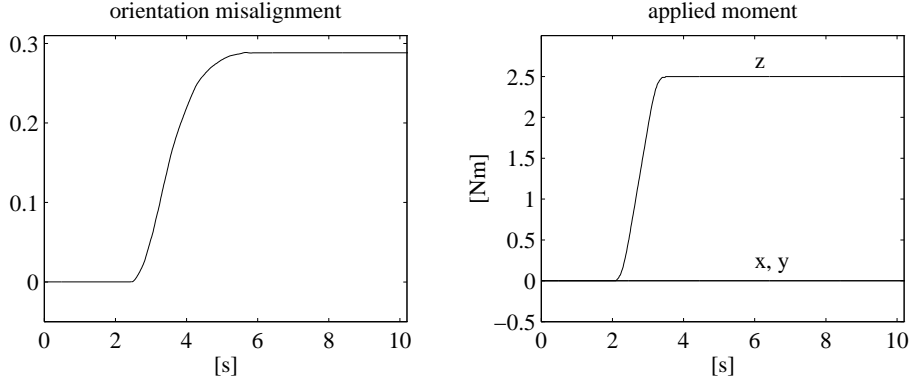


Figure 3.12. Experimental results under six-DOF impedance control based on classical Euler angles in the third case study.

The results in Figs. 3.11 and 3.12 show the different performance in terms of the orientation misalignment δ which has been defined as the norm of the vector product between the orientation error and the unit vector of the approach axis of Σ_d \mathbf{u}_{o3} , i.e.

$$\delta = \|\mathbf{S}({}^e\boldsymbol{\epsilon}_{de})\mathbf{u}_{o3}\|.$$

For the impedance control based on (3.32) the instantaneous axis of rotation of Σ_e changes, while remarkably no misalignment occurs for the impedance control based on (3.72). The impedance control based on (3.38) has also been tested and its performance is as good as that of the quaternion-based control; hence, the results are not reported for brevity.

Fourth case study: Nondiagonal rotational stiffness. In the fourth case study, the quaternion-based impedance control and the impedance control based on the alternative Euler angles have been tested when the *rotational stiffness* is chosen as a *nondiagonal* matrix. The impedance control based on the classical Euler angles has been ruled out in view of the poor results of the previous experiment.

The principal axes of the stiffness matrices of the rotational impedance equations (3.72) and (3.38) are rotated with respect to the coordinate axes of Σ_d ; \mathbf{K}_o has been chosen as in (3.66) with

$$\mathbf{U}_o = \begin{bmatrix} 0.8047 & -0.3106 & 0.5059 \\ 0.5059 & 0.8047 & -0.3106 \\ -0.3106 & 0.5059 & 0.8047 \end{bmatrix} \quad \boldsymbol{\Gamma}_o = \begin{bmatrix} 4 & 0 & 0 \\ 0 & 1 & 0 \\ 0 & 0 & 2.5 \end{bmatrix}$$

for both schemes. The remaining parameters of the rotational impedance have been set to $\mathbf{M}_o = 0.25\mathbf{I}$ and $\mathbf{D}_o = 1.5\mathbf{I}$ for both schemes. As above, no impedance control has been accomplished for the translational part, and the

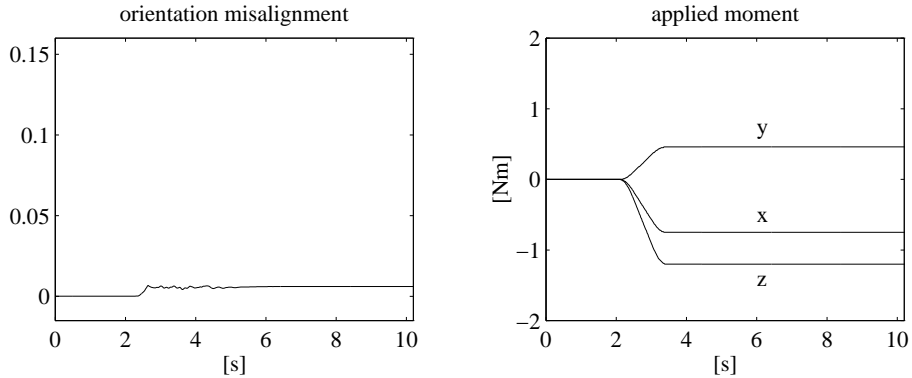


Figure 3.13. Experimental results under six-DOF impedance control based on quaternion in the fourth case study.

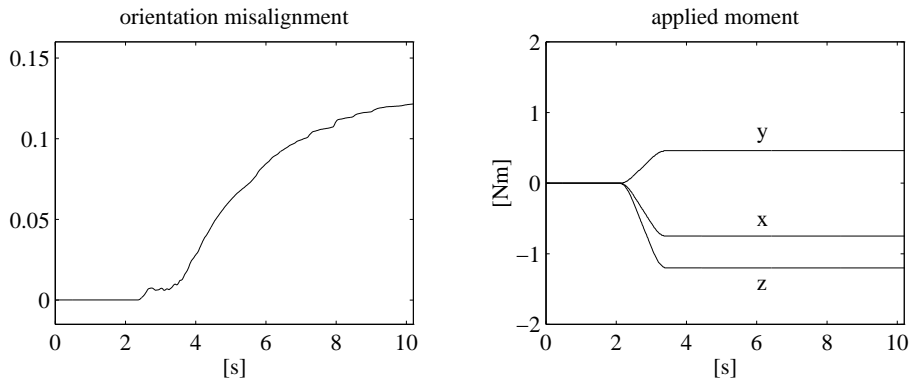


Figure 3.14. Experimental results under six-DOF impedance control based on alternative Euler angles in the fourth case study.

gains of the inner motion control loop have been chosen equal to those in the previous case study. A torque has been applied about the axis whose unit vector is \mathbf{u}_{o3} ; the torque is taken from zero to -1.5 Nm according to a linear interpolating polynomial with 4th-order blends and a total duration of 1 s.

The results in Figs. 3.13 and 3.14 show the significant differences occurring in terms of the orientation misalignment δ . It can be seen that the instantaneous axis of rotation of Σ_e does not appreciably rotate with the impedance control based on (3.72), given the performance of the inner loop acting on the end-effector orientation error. Instead, a significant misalignment occurs with the impedance control based on (3.38).

In sum, it can be concluded that the quaternion-based impedance control performs better than both impedance control schemes based on the Euler angles as far as task geometric consistency is concerned.

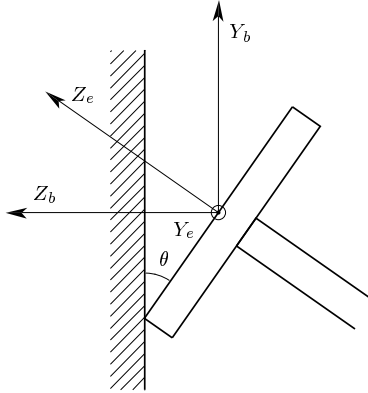


Figure 3.15. Disk in contact with surface.

Fifth case study: Redundancy resolution. The six-DOF quaternion-based impedance control has been tested in a case study when a *redundancy resolution* scheme is incorporated into the motion control as in Fig. 2.2.

The environment is constituted by a cardboard box. The translational stiffness at the contact between the end effector and the surface is of the order of 5000 N/m, while the rotational stiffness for small angles is of the order of 15 Nm/rad.

The task in the experiment consists of four phases; namely, reconfiguring the manipulator, approaching the surface, staying in contact, and leaving the surface. To begin, the additional task function in (2.91) has been chosen as

$$w(\mathbf{q}) = \frac{1}{2}(q_3 - q_{3d})^2$$

where q_3 is the elbow joint and q_{3d} is a desired trajectory from the initial value of q_3 to the final value of 1.1 rad in a time of 4 s with a fifth-order interpolating polynomial with null initial and final velocity and acceleration. This function is aimed at reconfiguring the manipulator in a more dexterous posture before contacting the surface.

After a lapse of 4 s, the disk is taken in contact with the surface at an angle $\theta = 7\pi/36$ rad; see Fig. 3.15 where the orientation of the base and end-effector frames is depicted. The end-effector desired position is required to make a straight-line motion with a horizontal displacement of 0.08 m along the Z_b axis of the base frame. The trajectory along the path is generated according to a fifth-order interpolating polynomial with null initial and final velocities and accelerations, and a duration of 2 s. The end-effector desired orientation is required to remain constant during the task. The surface is placed (vertically) in the X_bY_b -plane of the base frame in such a way to obstruct the desired end-effector motion, both for the translational part and the rotational part. After

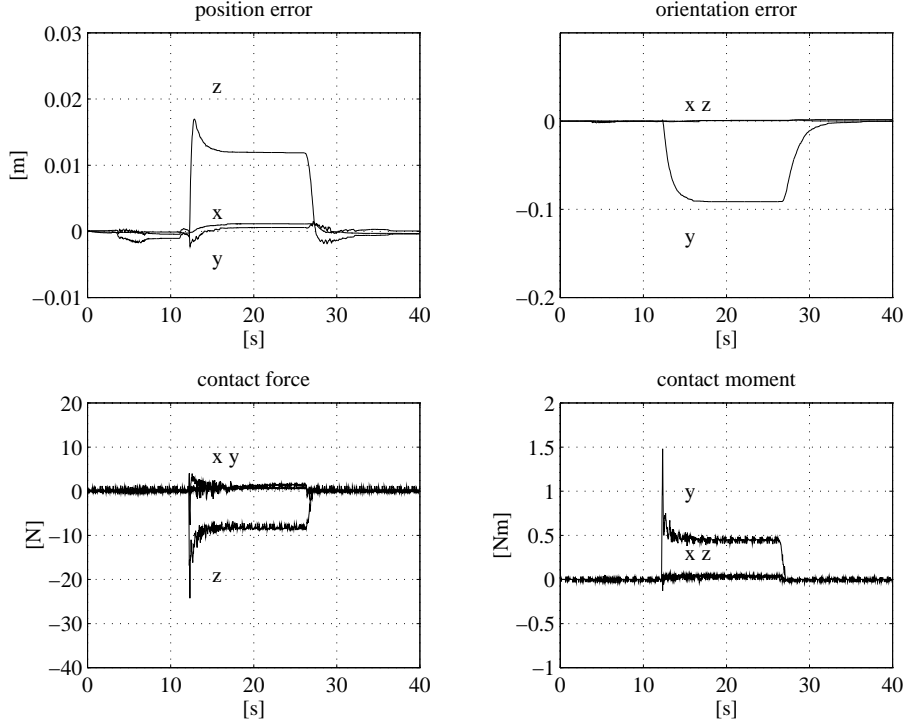


Figure 3.16. Experimental results under six-DOF impedance control based on quaternion in the fifth case study.

a lapse of 13 s in contact, the end-effector motion is commanded back to the initial position with a duration of 4 s.

The parameters of the translational impedance (3.25) have been set to $\mathbf{M}_p = 16\mathbf{I}$, $\mathbf{D}_p = \text{diag}\{800, 800, 250\}$ and $\mathbf{K}_p = \text{diag}\{1300, 1300, 800\}$, while the parameters of the rotational impedance (3.72) have been set to $\mathbf{M}_o = 0.7\mathbf{I}$ and $\mathbf{D}_o = 4\mathbf{I}$, $\mathbf{K}_o = 2.5\mathbf{I}$.

The gains of the inner motion control loop in (3.26) and (3.81) have been set to $\mathbf{K}_{Pp} = 2250\mathbf{I}$ and $\mathbf{K}_{Po} = 4000\mathbf{I}$, $\mathbf{K}_{Dp} = 70\mathbf{I}$ and $\mathbf{K}_{Do} = 75\mathbf{I}$. The gains of the redundancy resolution control in (2.89) and (2.91) have been set to $\mathbf{K}_n = 20\mathbf{I}$ and $k_\beta = 250$.

The results in Fig. 3.16 show the effectiveness of the six-DOF impedance control with redundancy resolution. During the reconfiguration (8 s), the components of the position error between Σ_d and Σ_e $\Delta\mathbf{p}_{de} = \mathbf{p}_d - \mathbf{p}_e$ and of the orientation error between Σ_d and Σ_e ${}^e\epsilon_{de}$ are practically zero, meaning that the dynamics of the null space motion does not disturb the end-effector motion. Such error remains small during the approach (2 s). During the contact (13 s), the component of the position error along the Z_b -axis significantly deviates

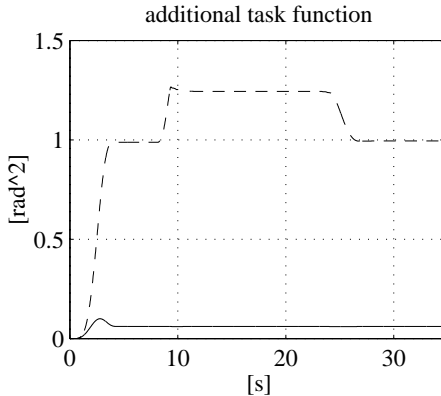


Figure 3.17. Additional task function in the fifth case study.

from zero, as expected; as for the orientation error, the component of the orientation error along the Y_e -axis significantly deviates from zero since Σ_e has to rotate about Y_e in order to comply with the surface. Also, in view of the imposed task, a prevailing component of the contact force can be observed along the Z_b -axis after the contact, whereas the sole component of the contact moment about the Y_e -axis is significant, as expected. During the takeoff (4 s), both the errors and the contact force and moment return to zero.

The same task has been executed again for the six-DOF impedance control without redundancy resolution ($k_\beta = 0$). The performance in terms of the contact between the end effector and the surface is substantially the same as above since the additional task does not interfere with the primary interaction task; hence, the time history of the relevant quantities is omitted for brevity. Nevertheless, a comparison between the two cases in Fig. 3.17 shows that the task function is successfully optimized when redundancy is exploited (solid) other than when redundancy is not exploited (dashed).

3.5 NONDIAGONAL SIX-DOF STIFFNESS

In the above treatment of the six-DOF impedance, it has been implicitly assumed that the translational stiffness is separated from the rotational stiffness. Nevertheless, the general form of a *six-DOF stiffness* may contain off-diagonal terms, which may be useful to accomplish certain compliant tasks, e.g. to prevent jamming during parts mating.

The quaternion displacement is considered hereafter in view of its task geometric consistency property and avoidance of representation singularities. A coupling elastic energy can be added to \mathcal{U}_p in (3.29) and \mathcal{U}_o in (3.71), leading

to

$$\mathcal{U} = \frac{1}{2} \Delta^c \mathbf{p}_{dc}^T \mathbf{K}_p \Delta^c \mathbf{p}_{dc} + 2^c \boldsymbol{\epsilon}_{dc}^T \mathbf{K}_o^c \boldsymbol{\epsilon}_{dc} + 2\eta_{dc}^c \boldsymbol{\epsilon}_{dc}^T \mathbf{K}_m \Delta^c \mathbf{p}_{dc} \quad (3.82)$$

where \mathbf{K}_m is a constant matrix such that the *nondiagonal stiffness* matrix

$$\mathbf{K} = \begin{bmatrix} \mathbf{K}_p & \mathbf{K}_m^T \\ \mathbf{K}_m & \mathbf{K}_o \end{bmatrix} \quad (3.83)$$

is positive definite. In (3.82) the position displacement has been referred to Σ_c for consistency with the orientation displacement. A sufficient condition for the positive definiteness of \mathbf{K} is

$$\gamma_m(\mathbf{K}_o) \gamma_m(\mathbf{K}_p) > \sigma_M^2(\mathbf{K}_m) \quad (3.84)$$

where $\gamma_m(\cdot)$ ($\gamma_M(\cdot)$) denotes the minimum (maximum) eigenvalue and $\sigma_M(\cdot)$ denotes the maximum singular value of a matrix. Notice that, being $|\eta_{dc}| \leq 1$, the function \mathcal{U} is positive definite in the variables $\Delta^c \mathbf{p}_{dc}$ and $^c \boldsymbol{\epsilon}_{dc}$ under condition (3.84).

Taking the time derivative of (3.82) yields

$$\dot{\mathcal{U}} = {}^c \mathbf{f}_E^T \Delta^c \dot{\mathbf{p}}_{dc} + {}^c \boldsymbol{\mu}_E^T \Delta^c \boldsymbol{\omega}_{dc} \quad (3.85)$$

where

$${}^c \mathbf{f}_E = \mathbf{K}_p \Delta^c \mathbf{p}_{dc} + 2 \mathbf{K}_m^T {}^c \boldsymbol{\epsilon}_{dc} \quad (3.86)$$

$${}^c \boldsymbol{\mu}_E = \mathbf{G}^T(\eta_{dc}, {}^c \boldsymbol{\epsilon}_{dc}) \mathbf{K}_m \Delta^c \mathbf{p}_{dc} + 2 \mathbf{E}^T(\eta_{dc}, {}^c \boldsymbol{\epsilon}_{dc}) \mathbf{K}_o {}^c \boldsymbol{\epsilon}_{dc} \quad (3.87)$$

with

$$\mathbf{G} = \eta_{dc} \mathbf{E} - {}^c \boldsymbol{\epsilon}_{dc} {}^c \boldsymbol{\epsilon}_{dc}^T, \quad (3.88)$$

are respectively the elastic force and moment which contain coupling terms, i.e. the orientation displacement appears in (3.86) while the position displacement appears in (3.87).

Therefore, the equations of the translational and the rotational impedance (3.25) and (3.72) become

$$\mathbf{M}_p \Delta^c \ddot{\mathbf{p}}_{dc} + \mathbf{D}_p \Delta^c \dot{\mathbf{p}}_{dc} + \mathbf{K}_p \Delta^c \mathbf{p}_{dc} + 2 \mathbf{K}_m^T {}^c \boldsymbol{\epsilon}_{dc} = {}^c \mathbf{f} \quad (3.89)$$

$$\mathbf{M}_o \Delta^c \dot{\boldsymbol{\omega}}_{dc} + \mathbf{D}_o \Delta^c \boldsymbol{\omega}_{dc} + \mathbf{K}'_m \Delta^c \mathbf{p}_{dc} + \mathbf{K}'_o {}^c \boldsymbol{\epsilon}_{dc} = {}^c \boldsymbol{\mu} \quad (3.90)$$

where the terms in (3.89) have all been referred to Σ_c , and

$$\mathbf{K}'_o = 2 \mathbf{E}^T(\eta_{dc}, {}^c \boldsymbol{\epsilon}_{dc}) \mathbf{K}_o \quad (3.91)$$

$$\mathbf{K}'_m = \mathbf{G}^T(\eta_{dc}, {}^c \boldsymbol{\epsilon}_{dc}) \mathbf{K}_m. \quad (3.92)$$

The stiffness analysis for small position and orientation displacements between Σ_d and Σ_c shows that

$${}^c\mathbf{f}_E \simeq \mathbf{K}_p \Delta {}^c\dot{\mathbf{p}}_{dc} dt + \mathbf{K}_m^T \Delta {}^c\omega_{dc} dt \quad (3.93)$$

$${}^c\boldsymbol{\mu}_E \simeq \mathbf{K}_m \Delta {}^c\dot{\mathbf{p}}_{dc} dt + \mathbf{K}_o \Delta {}^c\omega_{dc} dt \quad (3.94)$$

and thus \mathbf{K} is the stiffness matrix for small displacements.

As regards the property of *task geometric consistency*, taking the coupling stiffness as a symmetric matrix $\mathbf{K}_m = \mathbf{K}_m^T$ allows for the decomposition

$$\mathbf{K}_m = \mathbf{U}_m \boldsymbol{\Gamma}_m \mathbf{U}_m^T \quad (3.95)$$

where $\boldsymbol{\Gamma}_m = \text{diag}\{\gamma_{m1}, \gamma_{m2}, \gamma_{m3}\}$ and $\mathbf{U}_m = [\mathbf{u}_{m1} \ \mathbf{u}_{m2} \ \mathbf{u}_{m3}]$ are respectively the eigenvalue matrix and the (orthogonal) eigenvector matrix. Then, considering a null position displacement and an orientation displacement by an angle ϑ_{dc} about the i -th eigenvector gives

$${}^c\mathbf{f}_E = 2\gamma_{mi} \sin \frac{\vartheta_{dc}}{2} \mathbf{u}_{mi} \quad (3.96)$$

which represents an elastic force along the same \mathbf{u}_{mi} axis. On the other hand, considering a null orientation displacement and a position displacement of length λ along the i -th eigenvector gives

$${}^c\boldsymbol{\mu}_E = \lambda \gamma_{mi} \mathbf{u}_{mi} \quad (3.97)$$

which represents an elastic moment about the same \mathbf{u}_{mi} axis. Therefore, the coupling stiffness matrix \mathbf{K}_m can be expressed in terms of three parameters γ_{mi} representing the coupling stiffness about three principal axes \mathbf{u}_{mi} .

Finally, the computation of the equilibria of the impedance equations (3.89) and (3.90) with the relative stability analysis can be carried out in a conceptually analogous way to Subsection 3.3.

4. FURTHER READING

Stiffness control was proposed in [87] and is conceptually equivalent to compliance control [82]. Devices based on the remote center of compliance were discussed in [110] for successful mating of rigid parts. The original idea of a mechanical impedance model used for controlling the interaction between manipulator and environment is due to [50], and a similar formulation is given in [55].

The adoption of an inner motion control loop to provide impedance control with disturbance rejection was presented to [64], and has been experimentally demonstrated for an industrial robot with joint friction in [14]. Linear [31] and nonlinear [56, 22] adaptive impedance control algorithms have been proposed

to overcome model uncertainties, while robust schemes can be found in [65]. Impedance control has also been used in the hybrid position/force control framework [4]. Emphasis on the problems with a stiff environment is given in [54] and stability of impedance control was analyzed in [51]. The automatic specification of robotic tasks that involve multiple and time-varying contacts of the manipulator end-effector with the environment is a challenging issue. General formalisms addressing this problem were proposed in [83, 15].

A reference work on modeling six-DOF (spatial) stiffness is [61] while the properties of spatial compliance have been analyzed in detail in [80, 41]; a six-DOF variable compliant wrist was proposed in [52]. The energy-based approach to derive a spatial impedance was introduced in [42] and later adopted in [95] for active impedance control. The various six-DOF impedance control schemes with different representations of end-effector orientation can be found in [19] with full experimental support in [17]. The technique for redundancy resolution is based on [73, 74]. In [20, 21] the quaternion-based six-DOF impedance control is extended to the case of nondiagonal stiffness which can be useful for the execution of specific compliant tasks as discussed in [5].

Chapter 4

DIRECT FORCE CONTROL

Direct force control schemes are developed which achieve force regulation when the end effector is in contact with a compliant environment, thanks to the adoption of an integral action on the force error generated by an outer force loop. Motion control capabilities along the unconstrained task directions are recovered using a parallel composition of the force and motion control actions. Force tracking along the constrained task direction is achieved by adapting the estimate of the contact stiffness. Throughout the chapter, experimental results are presented for an industrial robot in contact with a compliant surface.

1. FORCE REGULATION

In the previous chapter, an indirect control of the contact force has been achieved by suitably controlling the end-effector motion. In this way, it is possible to ensure limited values of the contact force for a given rough estimate of the environment stiffness. Certain interaction tasks, however, do require the fulfillment of a precise value of the contact force. This would be possible, in theory, by tuning the active compliance control action and selecting a proper desired location for the end effector; such a strategy would be effective only on the assumption that an accurate estimate of the *contact stiffness* is available.

A radically different approach consists in designing a *direct force control* which operates on a force error between the desired and the measured values. On the other hand, in the previous chapter it has been emphasized that even impedance control, which does not aim at achieving a desired force, needs contact force measurements to obtain a linear and decoupled end-effector dynamics during the interaction. This is desirable in order to realize a compliant behavior only along those task directions that are actually constrained by the presence of the environment. Therefore, contact force measurements are fully exploited hereafter to design direct force control.

The realization of a force control scheme can be entrusted to the closure of an *outer force control* loop generating the reference input to the motion control scheme the robot manipulator is usually endowed with. Therefore, direct force control schemes are presented below which are logically derived from the motion control schemes using a static model-based compensation and a dynamic model-based compensation, respectively. In this respect, it should be stressed that the force control problem basically requires *regulation* of the contact force to a *constant* desired value.

1.1 STATIC MODEL-BASED COMPENSATION

Let \mathbf{f}_d and $\boldsymbol{\mu}_d$ denote the constant desired contact force and moment. With reference to the *static model-based compensation* in (2.92), the vectors $\boldsymbol{\gamma}_p$ and $\boldsymbol{\gamma}_o$ can be chosen as

$$\boldsymbol{\gamma}_p = \mathbf{K}_{Pp} \Delta \mathbf{p}_{ce} + \mathbf{f}_d \quad (4.1)$$

$$\boldsymbol{\gamma}_o = \mathbf{T}^{-T}(\boldsymbol{\varphi}_e) \mathbf{K}_{Po} \Delta \boldsymbol{\varphi}_{ce} + \boldsymbol{\mu}_d \quad (4.2)$$

with $\Delta \mathbf{p}_{ce}$ in (3.27) and $\Delta \boldsymbol{\varphi}_{ce}$ in (3.46). Notice that \mathbf{p}_c and $\boldsymbol{\varphi}_c$ represent the position and orientation of a *compliant frame* Σ_c which shall be determined through a proper force and moment control action. The terms \mathbf{f}_d in (4.1) and $\boldsymbol{\mu}_d$ in (4.2) represent a force and moment feedforward aimed at creating the presence of a force and moment error as

$$\Delta \mathbf{f} = \mathbf{f}_d - \mathbf{f} \quad (4.3)$$

$$\Delta \boldsymbol{\mu} = \boldsymbol{\mu}_d - \boldsymbol{\mu} \quad (4.4)$$

in the closed-loop equation of the system. Then, the vectors \mathbf{p}_c and $\boldsymbol{\varphi}_c$ can be chosen as a *proportional–integral (PI) control* on the force and moment error, i.e.

$$\mathbf{p}_c = \mathbf{K}_{Pp}^{-1} \left(\mathbf{K}_{Fp} \Delta \mathbf{f} + \mathbf{K}_{Ip} \int_0^t \Delta \mathbf{f} d\varsigma \right) \quad (4.5)$$

$$\boldsymbol{\varphi}_c = \mathbf{K}_{Po}^{-1} \left(\mathbf{K}_{Fo} \Delta \boldsymbol{\mu} + \mathbf{K}_{Io} \int_0^t \Delta \boldsymbol{\mu} d\varsigma \right) \quad (4.6)$$

where \mathbf{K}_{Fp} , \mathbf{K}_{Ip} , \mathbf{K}_{Fo} and \mathbf{K}_{Io} are suitable positive definite matrix gains. Notice that Equations (4.5) and (4.6) set an outer control loop on the contact force and moment, with respect to the inner control loop on the end-effector position and orientation in (4.1) and (4.2). To this regard, \mathbf{K}_{Pp}^{-1} in (4.5) and \mathbf{K}_{Po}^{-1} in (4.6) have been introduced in order to make the resulting force and moment control actions in (4.1) and (4.2) independent of the choice of the proportional gain on the position and orientation, respectively.

On the assumption that the desired contact force and moment are assigned so that they have nonnull components only along the constrained task directions,

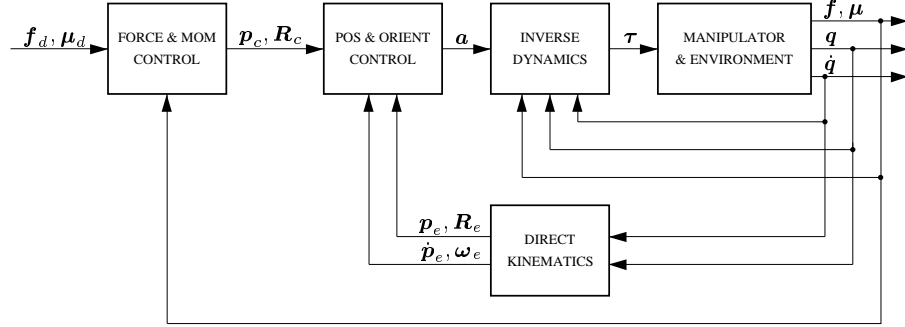


Figure 4.1. Force and moment control with inner motion control loop.

the control scheme based on (4.1), (4.2), (4.5) and (4.6) gives at steady state

$$\mathbf{f}_\infty = \mathbf{f}_d \quad (4.7)$$

$$\boldsymbol{\mu}_\infty = \boldsymbol{\mu}_d \quad (4.8)$$

thanks to the use of *integral control* actions on the force and moment errors. On the other hand, the proportional actions on the force and moment errors are aimed at improving the transient behavior during the interaction.

In sum, *regulation* of the *contact force and moment* to the desired values can be obtained, provided that the control gains are properly chosen so as to ensure stability of the closed-loop system.

1.2 DYNAMIC MODEL-BASED COMPENSATION

In order to enhance the performance of the system during the transient, it is worth considering *dynamic model-based compensation* as in (3.17) with α as in (2.26). With reference to (3.26) and (3.45), the linear and angular accelerations can be respectively chosen as

$$\mathbf{a}_p = -\mathbf{K}_{Dp}\dot{\mathbf{p}}_e + \mathbf{K}_{Pp}\Delta\mathbf{p}_{ce} \quad (4.9)$$

$$\mathbf{a}_o = \mathbf{T}(\varphi_e)(-\mathbf{K}_{Do}\dot{\varphi}_e + \mathbf{K}_{Po}\Delta\varphi_{ce}) + \dot{\mathbf{T}}(\varphi_e, \dot{\varphi}_e)\dot{\varphi}_e \quad (4.10)$$

where \mathbf{p}_c and φ_c are given in (4.5) and (4.6). Notice that, differently from (3.26) and (3.45), no feedforward of the linear and angular velocity and acceleration of Σ_c has been used since the goal is simply to achieve force regulation. As above, at steady state, the contact force and moment are taken to the desired values assuming that these are assigned consistently with the constrained task directions.

A block diagram of the resulting force and moment control scheme with dynamic model-based compensation is sketched in Fig. 4.1 where the presence of the *inner motion control* loop has been evidenced. Also, the orientation

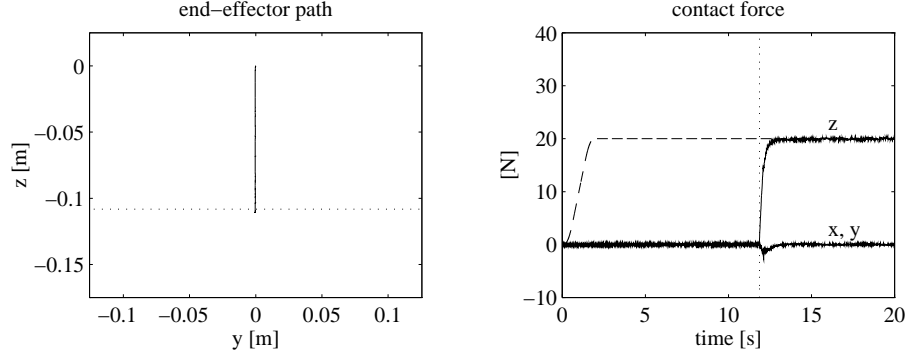


Figure 4.2. Experimental results under force control with static model-based compensation.

of the relevant frames has been described in terms of rotation matrices. With respect to the impedance control scheme with inner motion control in Fig. 3.4, the impedance control is replaced with a force and moment control which generates the position and orientation of Σ_c according to (4.5) and (4.6).

1.3 EXPERIMENTS

The above force and moment control schemes have been tested in *experiments* on the six-joint industrial robot described in Section 3. of Chapter 1 endowed with the force/torque sensor.

Only the inner three joints are used while the outer three joints are mechanically braked. Hence $n = 3$ in (2.92) with $\mathbf{J} = \mathbf{J}_p$ and $\boldsymbol{\gamma} = \boldsymbol{\gamma}_p$; accordingly, a three-DOF task is considered.

The environment and the end effector are those described in Subsection 1.2 of Chapter 3. The end effector is placed in the same initial position as for the case study in that subsection but, of course, no position trajectory is assigned. The desired force along Z_b is taken to 20 N according to a trapezoidal velocity profile with cubic blends, and null initial and final first and second time derivatives, and a duration of 2 s. The constant value is kept for the remaining portion of the task.

First case study: Force control with static model-based compensation. The gains of the various control actions have been set to $\mathbf{K}_{Pp} = 300000\mathbf{I}$ in (4.1), $\mathbf{K}_D = 3000\mathbf{I}$ in (2.92), while $\mathbf{K}_{Fp} = \mathbf{O}$ and $\mathbf{K}_{Ip} = 150\mathbf{I}$ in (4.5); note that the proportional action on the force error does not vanish because of the null \mathbf{K}_{Fp} since the force feedforward in (4.1) combined with the contact force term in (2.20) is in turn equivalent to a unitary proportional action.

The results are presented in Fig. 4.2 in terms of the end-effector path, together with the time history of the desired (dashed) and the actual (solid) contact

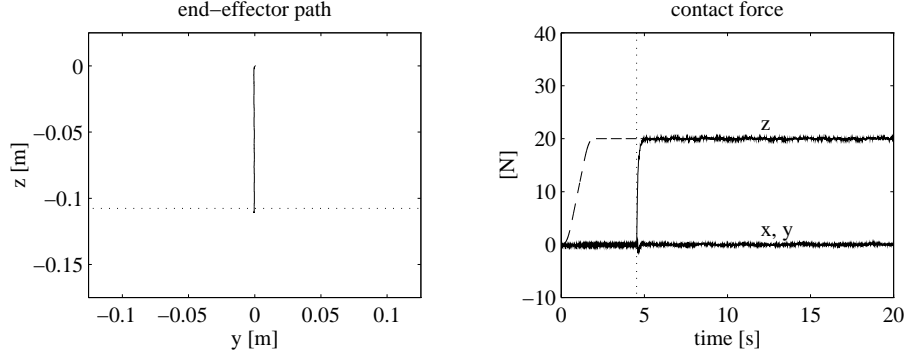


Figure 4.3. Experimental results under force control with dynamic model-based compensation.

force. As usual, the approximate location (dotted) of the surface is illustrated on the plot of the end-effector path, while the instant of contact (dotted line) is evidenced on the plot of the contact force.

Initially, the desired force trajectory causes a downward vertical motion since the end effector is required to push in the air; this brings the end effector to come in contact with the surface at $t = 12$ s. Then, the contact force is successfully regulated to the desired value. The components of contact friction force along X_b and Y_b are nearly zero since no motion is commanded along those directions.

Second case study: Force control with dynamic model-based compensation. The gains of the various control actions have been set to $\mathbf{K}_{Dp} = 90\mathbf{I}$ and $\mathbf{K}_{Pp} = 2500\mathbf{I}$ in (4.9), while $\mathbf{K}_{Fp} = 0.125\mathbf{I}$ and $\mathbf{K}_{Ip} = 37.5\mathbf{I}$ in (4.5).

The results are presented in Fig. 4.3 in terms of the end-effector path, together with the time history of the desired (dashed) and the actual (solid) contact force. As above, the approximate location (dotted) of the surface is illustrated on the plot of the end-effector path, while the instant of contact (dotted line) is evidenced on the plot of the contact force.

Initially, the desired force trajectory causes a downward vertical motion that brings the end effector to come in contact with the surface at $t = 4.5$ s. On the other hand, the response of the contact force is faster than that in Fig. 4.2 with pure force control thanks to the use of a dynamic model-based compensation which allows obtaining a larger bandwidth of the force loop without affecting stability.

2. FORCE AND MOTION CONTROL

With the adoption of a direct force control strategy, regulation of the contact force has been obtained at the expense of loss of control of the end-effector

motion. Nevertheless, it would be desirable to recover motion control along the unconstrained task directions while ensuring force control along the constrained task directions. This goal can be achieved only if a detailed description of the geometry of the environment is available. If that is not the case, an effective strategy can be pursued where control of both force and motion is carried out in all task directions; the control actions are to be designed on the basis of a simplified model of the environment while providing some sort of robustness to uncertainty. This is the underlying philosophy of the so-called *parallel control* approach described hereafter. In view of the difficulties concerned with contact modeling, the problem of force and position control is treated separately from that of moment and orientation control.

2.1 FORCE AND POSITION REGULATION

The idea of *parallel control* is to compose the compliant position in (4.5) with the desired position as

$$\mathbf{p}_r = \mathbf{p}_c + \mathbf{p}_d \quad (4.11)$$

and input this reference position \mathbf{p}_r , in lieu of \mathbf{p}_c , to the static model-based compensation control action in (4.1), i.e.

$$\gamma_p = \mathbf{K}_{Pp}(\mathbf{p}_r - \mathbf{p}_e) + \mathbf{f}_d. \quad (4.12)$$

Then, the control law (2.92) can be rewritten in terms of the quantities involving force and position only, i.e.

$$\boldsymbol{\tau} = \mathbf{J}_p^T(\mathbf{q})\gamma_p - \mathbf{K}_D\dot{\mathbf{q}} + \mathbf{g}(\mathbf{q}), \quad (4.13)$$

which, in view of (4.11) and (4.12), shall allow recovering regulation of the desired end-effector position along the unconstrained task directions if the force error in (4.5) acts only along the constrained task directions.

In order to gain insight into the behavior during interaction with parallel control, it is necessary to utilize a model of the environment. To this purpose, a planar surface is considered, which is locally a good approximation to surfaces of regular curvature, and the rotation matrix of the *compliant frame* Σ_c

$$\mathbf{R}_c = [\mathbf{t}_{1c} \quad \mathbf{t}_{2c} \quad \mathbf{n}_c] \quad (4.14)$$

is conveniently chosen with \mathbf{n}_c normal and \mathbf{t}_{1c} and \mathbf{t}_{2c} tangential to the plane. Thus, the model of the contact force is that given in (3.9), i.e. $\mathbf{f} = \mathbf{K}_f(\mathbf{p}_e - \mathbf{p}_o)$ where \mathbf{p}_o represents the position of any point on the undeformed plane and the *contact stiffness* matrix takes on the form

$$\mathbf{K}_f = \mathbf{R}_c \text{diag}\{0, 0, k_{f,n}\} \mathbf{R}_c^T = k_{f,n} \mathbf{n}_c \mathbf{n}_c^T \quad (4.15)$$

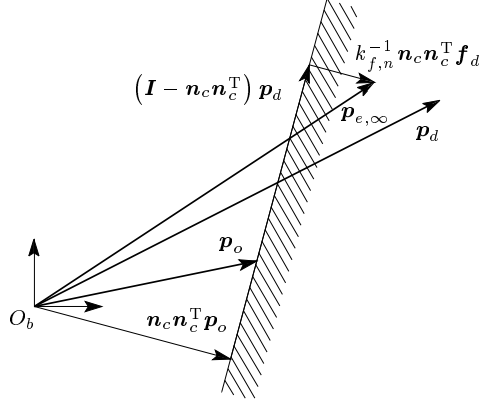


Figure 4.4. Equilibrium position with force and position control.

with $k_{f,n} > 0$. Notice that the orientation of Σ_c does not change during the interaction, hence \mathbf{R}_c is a constant matrix; on the other hand, the origin \mathbf{p}_c of Σ_c changes as a function of the force control action in (4.5).

The elastic contact model (3.9) and (4.15) shows that the contact force is normal to the plane, and thus a null force error can be obtained only if the desired force \mathbf{f}_d is aligned with \mathbf{n}_c . Also, it can be recognized that null position errors can be obtained only on the contact plane ($\mathbf{t}_{1c}, \mathbf{t}_{2c}$), while the component of \mathbf{p}_e along \mathbf{n}_c has to accommodate the force requirement specified by \mathbf{f}_d .

The steady state ($\dot{\mathbf{q}} = \mathbf{0}, \ddot{\mathbf{q}} = \mathbf{0}$) of the system (2.20) with (4.13) and (4.12) is

$$\mathbf{J}^T (\mathbf{K}_{Pp}(\mathbf{p}_r - \mathbf{p}_e) + \mathbf{f}_d) = \mathbf{J}^T \mathbf{f}. \quad (4.16)$$

On the assumption of a full-rank Jacobian, in view of (4.11) and (4.5), Equation (4.16) gives

$$\mathbf{K}_{Pp} \Delta \mathbf{p}_{de} + \mathbf{K}_{Fp} \Delta \mathbf{f} + \mathbf{K}_{Ip} \int_0^\infty \Delta \mathbf{f} d\varsigma + \Delta \mathbf{f} = \mathbf{0} \quad (4.17)$$

where the choice of scalar matrix gains is to be made, i.e. $\mathbf{K}_{Pp} = k_{Pp} \mathbf{I}$, $\mathbf{K}_{Fp} = k_{Fp} \mathbf{I}$ and $\mathbf{K}_{Ip} = k_{Ip} \mathbf{I}$, in order to avoid any rotation of the force and position vectors.

In view of the contact model (3.9) and (4.15), \mathbf{f}_d is taken along \mathbf{n}_c and thus the equilibrium is described by

$$\mathbf{p}_{e,\infty} = (\mathbf{I} - \mathbf{n}_c \mathbf{n}_c^T) \mathbf{p}_d + \mathbf{n}_c \mathbf{n}_c^T (k_{f,n}^{-1} \mathbf{f}_d + \mathbf{p}_o) \quad (4.18)$$

$$\mathbf{f}_\infty = k_{f,n} \mathbf{n}_c \mathbf{n}_c^T (\mathbf{p}_{e,\infty} - \mathbf{p}_o) = \mathbf{f}_d \quad (4.19)$$

where the matrix $(\mathbf{I} - \mathbf{n}_c \mathbf{n}_c^T)$ projects the vectors on the contact plane.

In Fig. 4.4 the equilibrium position is depicted when a constant \mathbf{p}_d is assigned. It can be recognized that $\mathbf{p}_{e,\infty}$ differs from \mathbf{p}_d by a vector aligned along the normal to the contact plane whose magnitude is that necessary to guarantee $\mathbf{f}_\infty = \mathbf{f}_d$ in view of (4.19).

It might be argued that the assignment of \mathbf{f}_d along \mathbf{n}_c indeed requires the knowledge of the normal direction to the contact plane. If this conditions does not hold, then it can be found that a drift motion of the end effector is generated along the plane. Therefore, if the contact geometry is unknown, it is advisable to set $\mathbf{f}_d = \mathbf{0}$.

In sum, *regulation* of the *end-effector position* to the desired components along the plane with *regulation* of the *contact force* to the desired component along the normal to the plane can be obtained, provided that the control gains are properly chosen so as to ensure stability of the closed-loop system. This issue will be reconsidered in the next chapter, when an adaptive version of this parallel regulator will be presented.

2.2 FORCE AND POSITION CONTROL

The above control scheme provides regulation of the end-effector position along the unconstrained task directions. On the other hand, tracking of a desired time-varying position can be achieved by using a dynamic model-based compensation. To this purpose, the linear acceleration in (4.9) can be modified as

$$\mathbf{a}_p = \ddot{\mathbf{p}}_d + \mathbf{K}_{Dp}(\dot{\mathbf{p}}_d - \dot{\mathbf{p}}_e) + \mathbf{K}_{Pp}(\mathbf{p}_r - \mathbf{p}_e) \quad (4.20)$$

where \mathbf{p}_r is given in (4.11) and feedforward of the desired velocity and acceleration has been added in view of the presence of \mathbf{p}_d in \mathbf{p}_r .

The equations of the closed-loop system can be obtained by plugging (4.20) in (2.30) with \mathbf{p}_c as in (4.5), leading to

$$\Delta \ddot{\mathbf{p}}_{de} + \mathbf{K}_{Dp} \Delta \dot{\mathbf{p}}_{de} + \mathbf{K}_{Pp} \Delta \mathbf{p}_{de} + \mathbf{K}_{Fp} \Delta \mathbf{f} + \mathbf{K}_{Ip} \int_0^t \Delta \mathbf{f} d\varsigma = \mathbf{0}. \quad (4.21)$$

Projecting (4.21) on the axes of Σ_c in (4.14) and taking $\mathbf{f}_{d,t} = \mathbf{0}$ yields

$$\Delta \ddot{\mathbf{p}}_{de,t} + k_{Dp} \Delta \dot{\mathbf{p}}_{de,t} + k_{Pp} \Delta \mathbf{p}_{de,t} = \mathbf{0} \quad (4.22)$$

$$\Delta \ddot{p}_{de,n} + k_{Dp} \Delta \dot{p}_{de,n} + k_{Pp} \Delta p_{de,n} + k_{Fp} \Delta f_n + k_{Ip} \int_0^t \Delta f_n d\varsigma = 0 \quad (4.23)$$

where $\mathbf{K}_{Dp} = k_{Dp} \mathbf{I}$, $\mathbf{K}_{Pp} = k_{Pp} \mathbf{I}$, $\mathbf{K}_{Fp} = k_{Fp} \mathbf{I}$ and $\mathbf{K}_{Ip} = k_{Ip} \mathbf{I}$.

Equation (4.22) describes the dynamic behavior of the components of the position error on the contact plane. Stability is obtained for any choice of $k_{Dp}, k_{Pp} > 0$ and *tracking* of the desired *end-effector position* on the contact plane is ensured.

On the other hand, Equation (4.23) involves the normal components of both the position error and the force error. In view of the model (3.9) and (4.15), it is

$$\Delta p_{de,n} = k_{f,n}^{-1} \Delta f_n - d_n \quad (4.24)$$

with

$$d_n = k_{f,n}^{-1} f_{d,n} - p_{d,n} + p_{o,n}, \quad (4.25)$$

which allows rewriting (4.23) as

$$k_{f,n}^{-1} \Delta \ddot{f}_n + k_{f,n}^{-1} k_{Dp} \Delta \dot{f}_n + (k_{f,n}^{-1} k_{Pp} + k_{Fp}) \Delta f_n + k_{Ip} \int_0^t \Delta f_n d\varsigma = \phi_n \quad (4.26)$$

where

$$\phi_n = \ddot{d}_n + k_{Dp} \dot{d}_n + k_{Pp} d_n. \quad (4.27)$$

Stability of the third-order system described by (4.26) can be ensured by choosing the gains k_{Dp} , k_{Pp} , k_{Fp} and k_{Ip} so as to satisfy the condition

$$k_{Ip} < k_{Dp} (k_{f,n}^{-1} k_{Pp} + k_{Fp}) \quad (4.28)$$

which requires a rough estimate of the stiffness coefficient $k_{f,n}$. Further, if d_n is constant, then ϕ_n is constant and *regulation* of the *contact force* to the desired component along the normal to the plane is ensured.

Notice that, since $p_{o,n}$ and $f_{d,n}$ in (4.25) have been assumed to be constant, d_n is constant as long as $p_{d,n}$ is constant, i.e. the desired trajectory must have null velocity and acceleration along the normal to the plane.

On the other hand, if $p_{d,n}$ is not constant, then in view of (4.26) the position trajectory acts as a disturbance on the dynamics of the force error. Such a disturbance ϕ_n is bounded as long as the desired position, velocity and acceleration are bounded. The presence of an integral action on the force error confers disturbance rejection capability to the system while guaranteeing null force error at steady state for a constant disturbance. This feature makes the scheme inherently robust to unplanned contact situations. In fact, if contact occurs along a faulty supposedly unconstrained task direction (where a null desired force is assigned), control provides an immediate recovery by keeping the contact force bounded at the expense of a position error along that direction.

A block diagram of the resulting *force and position control* scheme with parallel composition is sketched in Fig. 4.5. Apart from the lack of control of orientation and moment, this scheme differs from the force control scheme in Fig. 4.1 in that the position of the compliant frame is added to the desired position as in (4.11) generating the position of a reference frame Σ_r for the position control; this receives as input also the desired velocity and acceleration.

The selection of the control gains for the above parallel control scheme shall be accomplished so as to achieve a satisfactory behavior during both

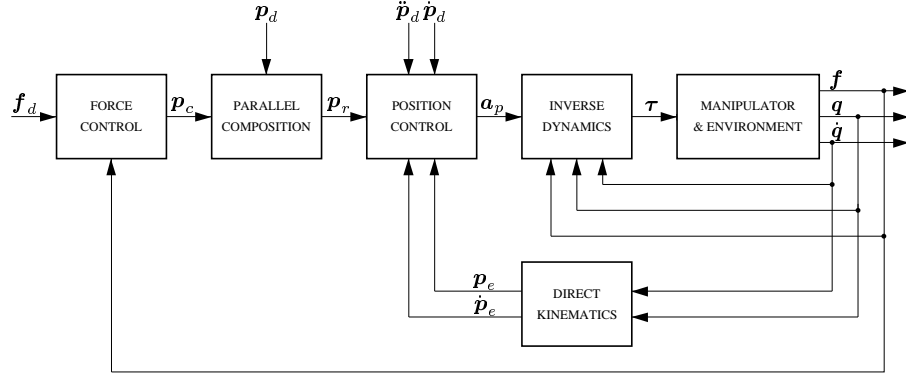


Figure 4.5. Force and position control with parallel composition.

unconstrained and constrained motion. It might be argued, however, that the choice of the gains for the force control action does depend on the choice of the gains for the position control action.

A modified parallel control scheme can be devised with the goal of designing the force control action independently of the position control action. In particular, the *parallel composition* in (4.11) can be extended to velocity and acceleration, i.e.

$$\dot{p}_r = \dot{p}_c + \dot{p}_d \quad (4.29)$$

$$\ddot{\mathbf{p}}_r = \ddot{\mathbf{p}}_c + \ddot{\mathbf{p}}_d \quad (4.30)$$

and thus the linear acceleration in (4.20) is modified into

$$\mathbf{a}_p = \ddot{\mathbf{p}}_r + \mathbf{K}_{Dp}(\dot{\mathbf{p}}_r - \dot{\mathbf{p}}_e) + \mathbf{K}_{Pp}(\mathbf{p}_r - \mathbf{p}_e) \quad (4.31)$$

where p_c in (4.11) is the solution to the differential equation

$$K_{Ap}\ddot{p}_c + K_{Vp}\dot{p}_c = \Delta f \quad (4.32)$$

with $\mathbf{p}_c(0) = \mathbf{0}$, $\mathbf{K}_{Ap} = k_{Ap}\mathbf{I}$ and $\mathbf{K}_{Vp} = k_{Vp}\mathbf{I}$. It is worth pointing out that \mathbf{p}_c resulting from integration of (4.32) provides an *integral control* action on the force error.

Projecting (4.32) on n_c gives

$$k_{Ap}\ddot{p}_{c,n} + k_V p \dot{p}_{c,n} = \Delta f_n, \quad (4.33)$$

while assuming that f_d is along n_c , it is $\mathbf{p}_{c,t} = \mathbf{0}$ and $\dot{\mathbf{p}}_{c,t} = \mathbf{0}$. On the other hand, Equation (4.31) with (2.30) reveals that the end-effector position \mathbf{p}_e tracks the trajectory given by \mathbf{p}_r , i.e. $\mathbf{p}_e = \mathbf{p}_r$ and $\dot{\mathbf{p}}_e = \dot{\mathbf{p}}_r$. Therefore, projecting (4.11) and (4.29) on the contact plane gives

$$p_{e,t} = p_{d,t} \quad (4.34)$$

$$\dot{\mathbf{p}}_{e,t} = \dot{\mathbf{p}}_{d,t} \quad (4.35)$$

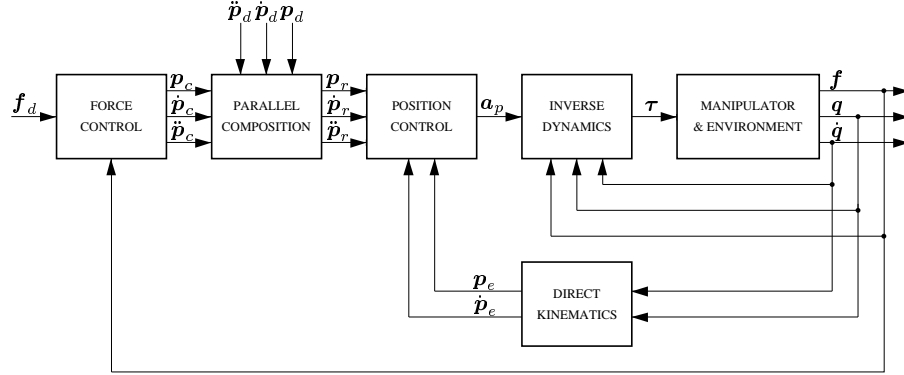


Figure 4.6. Force and position control with full parallel composition.

and thus *tracking* of the desired *end-effector position* along the unconstrained task directions is ensured.

Further, assuming that the component of \mathbf{p}_d along \mathbf{n}_c is constant, the projection of (4.29) and (4.30) on the normal to the contact plane gives

$$\dot{p}_{e,n} = \dot{p}_{c,n} \quad (4.36)$$

$$\ddot{p}_{e,n} = \ddot{p}_{c,n}. \quad (4.37)$$

Folding (4.36) and (4.37) into (4.33) and using (4.24) with constant $f_{d,n}$ yields

$$k_{Ap} k_{f,n}^{-1} \ddot{f}_n + k_{Vp} k_{f,n}^{-1} \dot{f}_n = \Delta f_n \quad (4.38)$$

which implies *regulation* of the *contact force* to the desired value along the constrained task direction, for any choice of $k_{Ap}, k_{Vp} > 0$. The force error dynamics continues to depend on the contact stiffness but, remarkably, is now independent of the position error dynamics, so as wished.

A block diagram of the resulting force and position control scheme is sketched in Fig. 4.6, where the full parallel composition is evidenced. Compared to the previous scheme in Fig. 4.5, the force control generates the velocity and acceleration of the origin of the compliant frame as in (4.32) in addition to its position; these are summed to the corresponding desired position, velocity and acceleration to provide the analogous quantities to be input to the position control.

2.3 MOMENT AND ORIENTATION CONTROL

The strategy presented above for force and position control can be conceptually pursued also for *moment and orientation control*, as shown in the following.

The counterpart of (4.31) is given by the angular acceleration

$$\mathbf{a}_o = \dot{\boldsymbol{\omega}}_r + \mathbf{K}_{Do}(\boldsymbol{\omega}_r - \boldsymbol{\omega}_e) + \mathbf{K}_{Po} \mathbf{R}_e^e \boldsymbol{\epsilon}_{re} \quad (4.39)$$

where ${}^e\epsilon_{re}$ is the vector part of the quaternion $\mathcal{Q}_{re} = \mathcal{Q}_e^{-1} * \mathcal{Q}_r$ expressing the orientation error between Σ_r and Σ_e ; accordingly, ω_r and $\dot{\omega}_r$ respectively denote the angular velocity and acceleration of Σ_r .

By analogy with (4.11), (4.29) and (4.30), the *parallel composition* rule can be written in terms of

$$\mathcal{Q}_r = \mathcal{Q}_c * \mathcal{Q}_{dc} \quad (4.40)$$

$${}^c\omega_r = {}^c\omega_c + {}^c\omega_{dc} \quad (4.41)$$

$${}^c\dot{\omega}_r = {}^c\dot{\omega}_c + {}^c\dot{\omega}_{dc} \quad (4.42)$$

where \mathcal{Q}_c , ω_c and $\dot{\omega}_c$ characterize the rotational motion of the *compliant frame* Σ_c , \mathcal{Q}_{dc} , ω_{dc} and $\dot{\omega}_{dc}$ represent the desired rotational motion where the double subscript indicates that such a motion shall be assigned as a *relative rotation* with respect to the time-varying compliant frame; also, the quantities in (4.41) and (4.42) have been conveniently referred to Σ_c .

The analogy is completed by computing the rotational motion of Σ_c according to the differential equation

$$\mathbf{K}_{Ao} {}^c\dot{\omega}_c + \mathbf{K}_{Vo} {}^c\omega_c = \Delta {}^c\mu \quad (4.43)$$

with $\Delta\mu$ as in (4.4), where $\mathbf{K}_{Ao} = k_{Ao}\mathbf{I}$ and $\mathbf{K}_{Vo} = k_{Vo}\mathbf{I}$. On the other hand, the origin \mathbf{p}_c of Σ_c is assumed to be constant. As for the previous force and position control scheme, \mathcal{Q}_c resulting from integration of (4.43) provides an *integral control* action on the moment error.

A block diagram of the resulting moment and orientation control scheme with parallel composition is sketched in Fig. 4.7, where rotation matrices have been conventionally indicated to represent orientation of relevant frames. This scheme is the counterpart of the force and position control scheme in Fig. 4.6, where the moment control generates the orientation, angular velocity and angular acceleration of Σ_c as in (4.43); these are combined with the desired orientation, angular velocity and angular acceleration as in (4.40), (4.41) and (4.42) to generate the corresponding reference quantities to be input to the orientation control.

By assuming a frictionless and elastically compliant type of contact, the model of the environment utilized to analyze the behavior during interaction with the above control scheme is taken as

$${}^c\mu = {}^c\mathbf{K}_\mu {}^c\omega_{edt}, \quad (4.44)$$

where ${}^c\omega_{edt}$ denotes an infinitesimal angular displacement of Σ_e and all the quantities have been referred to Σ_c . The rotational *contact stiffness* ${}^c\mathbf{K}_\mu$ is a symmetric and positive semi-definite matrix which is constant when referred

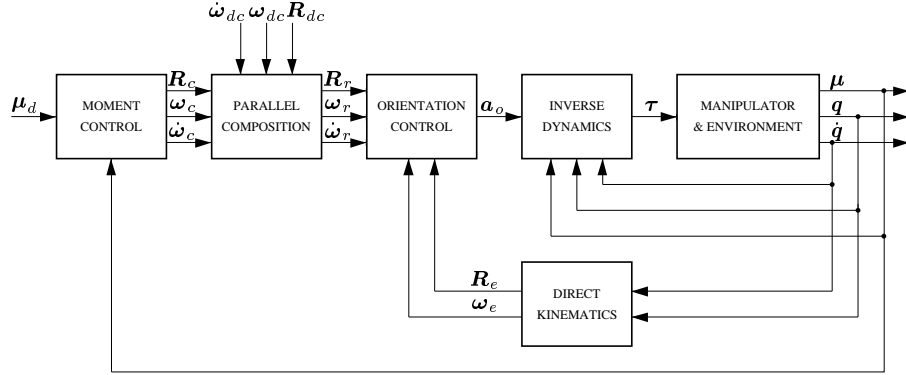


Figure 4.7. Moment and orientation control with parallel composition.

to Σ_c . With reference to \mathbf{R}_c in (4.14), a possible choice for ${}^c\mathbf{K}_\mu$ is

$${}^c\mathbf{K}_\mu = \begin{bmatrix} {}^c\mathbf{K}_{\mu,t} & \mathbf{0} \\ \mathbf{0}^T & 0 \end{bmatrix} \quad (4.45)$$

where ${}^c\mathbf{K}_{\mu,t}$ is a positive definite matrix expressing the rotational stiffness about two axes of the plane $(\mathbf{t}_{1c}, \mathbf{t}_{2c})$.

The elastic contact model (4.44) and (4.45) suggests that, since ${}^c\mu_n = 0$, a null moment error can be obtained only if the desired moment ${}^c\mu_d$ has a null component along \mathbf{n}_c , i.e. ${}^c\mu_{d,n} = 0$. Further, a desired rotational motion relative to Σ_c can be imposed only about \mathbf{n}_c , i.e. along the unconstrained task direction, and thus the choice ${}^c\omega_{dc,t} = \mathbf{0}$ and ${}^c\dot{\omega}_{dc,t} = \mathbf{0}$. These assumptions are assumed to hold in the remainder. Accordingly, it is ${}^c\omega_{c,n} = 0$ and ${}^c\dot{\omega}_{c,n} = 0$ in (4.43) which can thus be projected on the tangential plane, i.e.

$$k_{Ao} {}^c\dot{\omega}_{c,t} + k_{Vo} {}^c\omega_{c,t} = \Delta {}^c\mu_t. \quad (4.46)$$

Equation (4.39) with (2.31) reveals that the rotational motion of Σ_e tracks the rotational motion of Σ_r , i.e. $\omega_e = \omega_r$. Therefore, the projection of (4.41) and (4.42) along \mathbf{n}_c gives

$${}^c\omega_{e,n} = {}^c\omega_{dc,n} \quad (4.47)$$

and thus *tracking* of the desired *end-effector rotational motion* along the unconstrained task direction is ensured.

On the other hand, the projection of (4.41) and (4.42) on the tangential plane gives

$${}^c\omega_{e,t} = {}^c\omega_{c,t} \quad (4.48)$$

$${}^c\dot{\omega}_{e,t} = {}^c\dot{\omega}_{c,t}. \quad (4.49)$$

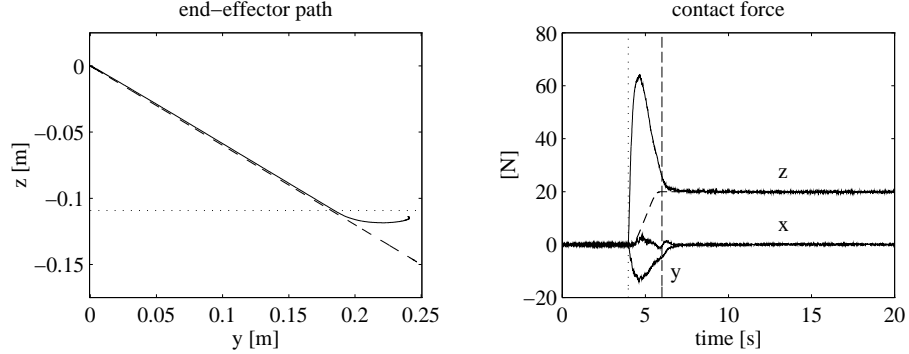


Figure 4.8. Experimental results under force and position regulator with parallel composition.

Computing the time derivative of (4.44) and projecting on the tangential plane yields

$${}^c\dot{\mu}_t = {}^cK_{\mu,t} {}^c\omega_{e,t}. \quad (4.50)$$

Then, folding (4.48) and (4.49) into (4.46) and using (4.50) leads to

$$k_{Ao} {}^cK_{\mu,t}^{-1} {}^c\ddot{\mu}_t + k_{Vo} {}^cK_{\mu,t}^{-1} {}^c\dot{\mu}_t = \Delta {}^c\mu_t \quad (4.51)$$

which implies *regulation* of the *contact moment* to the desired value along the constrained task directions, for any choice of $k_{Ao}, k_{Vo} > 0$.

2.4 EXPERIMENTS

The above force and motion control schemes have been tested in *experiments* on the six-joint industrial robot described in Section 3. of Chapter 1 endowed with the force/torque sensor.

First case study: Force and position regulation. Only the inner three joints are used while the outer three joints are mechanically braked; accordingly, a three-DOF task is considered.

The environment and the end effector are those described in Subsection 1.2 of Chapter 3. The end effector is placed in the same initial position as for the previous case studies. The end-effector task is the same as for the case study in Subsection 1.2 of Chapter 3, while the same force trajectory as in Subsection 1.3 starts when contact is detected. The gains of the control action in (4.12) and (4.5) have been chosen as for the first case study of Subsection 1.3.

The results are presented in Fig. 4.8 in terms of the desired (dashed) and the actual (solid) end-effector path, together with the time history of the desired (dashed) and the actual (solid) contact force. As above, the approximate location (dotted) of the surface is illustrated on the plot of the end-effector

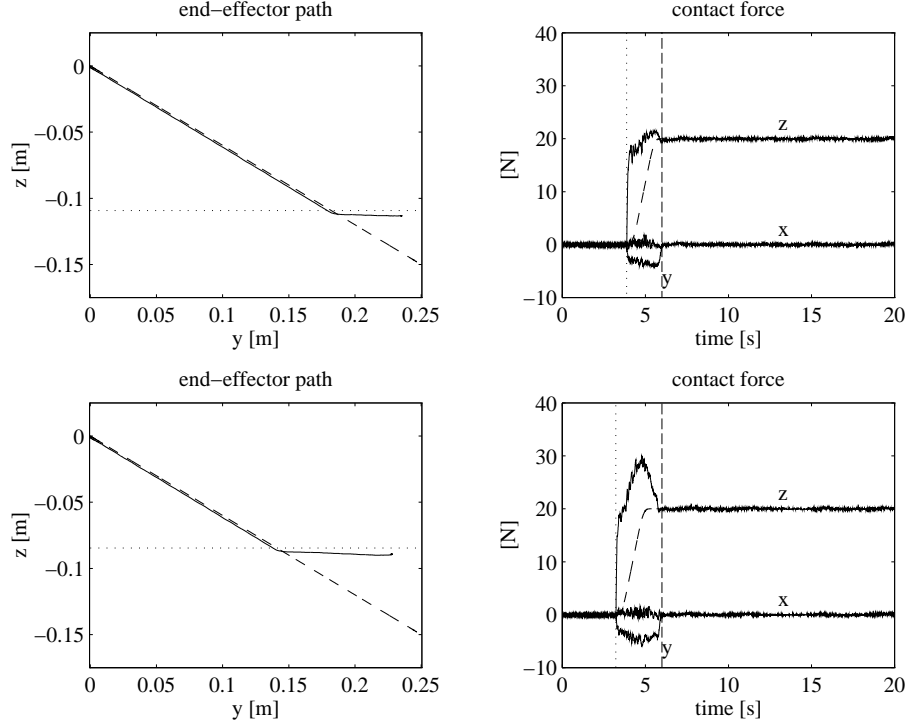


Figure 4.9. Experimental results under force and position control with full parallel composition.

path, while the instant of contact (dotted line) and the instant of the end of the motion trajectory (dashed line) are evidenced on the plot of the contact force.

It can be recognized that path tracking accuracy is satisfactory during unconstrained motion, even with a simple PD position control action plus gravity compensation. On the other hand, during constrained motion, after a transient the contact force reaches the desired value; the peak on the component along Z_b is due to the nonnull value of end-effector velocity at the contact as well as to the imposed motion into the surface, whereas the appreciable deviation from zero of the component along Y_b can be imputed to contact friction and local deformation of the surface resulting from the imposed end-effector motion.

In any case, both components of contact friction force along X_b and Y_b are regulated to zero in view of the integral action on all the components of the force error, whereas the component along Z_b reaches a steady-state value which guarantees exact force regulation.

Second case study: Force and position control. In view of its expected better performance, the force and position control with full parallel composition is considered.

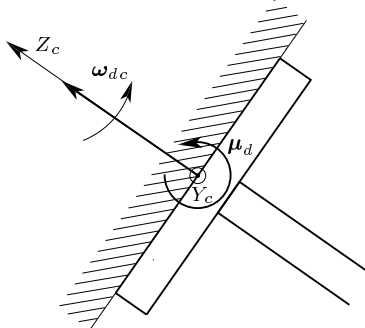


Figure 4.10. Geometry of contact.

As above, only the inner three joints are used while the outer three joints are mechanically braked; accordingly, a three-DOF task is considered.

The environment, the end effector and the task are the same as in the previous case study. The gains of the control action in (4.31) and (4.32) have been set to $\mathbf{K}_{Dp} = 90\mathbf{I}$, $\mathbf{K}_{Pp} = 2500\mathbf{I}$, $\mathbf{K}_{Ap} = 8\mathbf{I}$ and $\mathbf{K}_{Vp} = 480\mathbf{I}$.

The results are presented in the upper part of Fig. 4.9 in terms of the desired (dashed) and the actual (solid) end-effector path, together with the time history of the desired (dashed) and the actual (solid) contact force. As above, the approximate location (dotted) of the surface is illustrated on the plot of the end-effector path, while the instant of contact (dotted line) and the instant of the end of the motion trajectory (dashed line) are evidenced on the plot of the contact force.

It can be recognized that path tracking accuracy is very good during unconstrained motion. On the other hand, the response of the contact force is faster than that with the force and position regulator, in view of the inverse dynamics compensation. As a consequence, the peak on the contact force along Z_b is greatly reduced and successful regulation to the desired value continues to be achieved. A smaller deformation of the surface occurs which also contributes to reducing the contact friction along Y_b by a factor of about two.

As for the second case study of impedance control with inner motion control in Subsection 2.4 of Chapter 3, to investigate robustness of the scheme with respect to changes in the environment location, the task is repeated with the same control parameters as above but the cardboard box is raised by about 0.025 m. From the results presented in the lower part of Fig. 4.9, it can be recognized that, despite the different location of the surface, the desired force set point is still achieved; however, larger values of contact force are obtained during the transient due to the larger impact velocity.

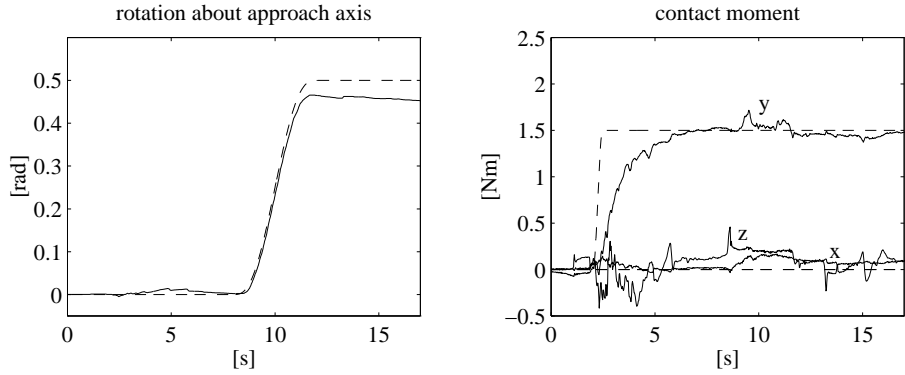


Figure 4.11. Experimental results under moment and orientation control.

Third case study: Moment and orientation control. All the six joints of the robot are involved in this case study.

The end effector is that described in Subsection 3.4. The disk is in contact with a planar surface such that the approach axis is aligned with the normal to the surface. The contact is characterized by a rotational stiffness matrix $\mathbf{K}_\mu = \text{diag}\{30, 30, 0\}$ Nm/rad, i.e. the unconstrained motion is described by any rotation about the approach axis. The compliant frame is determined so that its Z_c -axis is aligned with the normal to the surface.

The interaction task is as follows. At $t = 2$ s, the moment is taken to $[0 \ 1.5 \ 0]^T$ in Σ_c , according to a fifth-order polynomial with null initial and final first and second time derivatives, and a duration of 0.5 s; the final value is kept constant for the remaining portion of the task. The desired end-effector position is kept constant. After a lapse of 6 s, the desired end-effector orientation is required to make a rotation of 0.5 rad about the approach axis; the trajectory is generated according to a fifth-order interpolating polynomial with null initial and final velocities and accelerations, and a duration of 4 s. The geometry of the contact during the task is depicted in Fig. 4.10 where the desired angular velocity and contact moment are represented.

A full six-DOF inverse dynamics control is used, where the linear acceleration is taken as a pure position control with the gains in (2.33) as $\mathbf{K}_{Dp} = 65\mathbf{I}$ and $\mathbf{K}_{Pp} = 2500\mathbf{I}$. On the other hand, the angular acceleration is chosen as in (4.39) and the gains have been set to $\mathbf{K}_{Do} = 65\mathbf{I}$ and $\mathbf{K}_{Do} = 4500\mathbf{I}$, and the gains in the moment control action (4.43) have been set to $\mathbf{K}_{Ao} = \mathbf{I}$ and $\mathbf{K}_{Vo} = 24\mathbf{I}$.

The results are presented in Fig. 4.11 in terms of the time history of the rotation angle about the approach axis of Σ_e and of the three components of the desired (dashed) and the actual (solid) contact moment. It can be recognized that satisfactory tracking of the desired end-effector orientation trajectory is

achieved, while the contact moment is successfully regulated to the desired value. Notice that the moment components along X_c and Z_c are affected by contact friction which causes a steady-state deviation on the rotation angle from the desired value; this cannot be recovered since the integral action operates on all the components of the moment error, causing an orientation error also about the unconstrained motion axis.

3. FORCE TRACKING

The common feature of all the above force and motion control schemes is the possibility of regulating the contact force to a desired value, without using explicit information on the *contact stiffness* of the environment. It has been shown, however, that the actual value of the stiffness does influence the transient behavior during the interaction. The typical uncertainty on the contact stiffness constitutes the key limitation preventing *force tracking*. Below is presented a force and position control scheme which achieves force tracking along the constrained task direction and position tracking along the unconstrained task directions, thanks to the use of an adaptation mechanism on the estimate of the contact stiffness.

3.1 CONTACT STIFFNESS ADAPTATION

With reference to the force and position control with full parallel composition, the force control action described in (4.32) can be replaced with

$$\mathbf{K}_{Ap}\ddot{\mathbf{p}}_c + \mathbf{K}_{Vp}\dot{\mathbf{p}}_c = \boldsymbol{\phi} \quad (4.52)$$

where

$$\boldsymbol{\phi} = k_{f,n}^{-1} \mathbf{f}_c \quad (4.53)$$

with

$$\mathbf{f}_c = \mathbf{K}_{Ap}\ddot{\mathbf{f}}_d + \mathbf{K}_{Vp}\dot{\mathbf{f}}_d + \Delta\mathbf{f}. \quad (4.54)$$

It is worth pointing out that a *time-varying* desired force has been considered with suitable feedforward of the first and second derivatives in (4.54). Also, \mathbf{f}_d , $\dot{\mathbf{f}}_d$ and $\ddot{\mathbf{f}}_d$ are assumed to be aligned with \mathbf{n}_c .

Integration of (4.52) gives the position, linear velocity and acceleration of Σ_c to be used in the parallel compositions (4.11), (4.29) and (4.30). Then, the linear acceleration is computed as in (4.31) for inverse dynamics control.

By assuming that the component of \mathbf{p}_d along \mathbf{n}_c is constant, *tracking* of the desired *end-effector position* along the unconstrained task directions continues to hold. Moreover, projecting (4.52) on the normal to the contact plane gives

$$k_{Ap}\Delta\ddot{f}_n + k_{Vp}\Delta\dot{f}_n + \Delta f_n = 0 \quad (4.55)$$

where (4.24), (4.36), (4.37), (4.53) and (4.54) have been used. Equation (4.55) implies *tracking* of the desired *contact force* along the constrained task direction.

The above result relies on the assumption that $k_{f,n}$ in (4.53) is exactly known, which is unlikely to be the case in practice. However, the control scheme can be modified by using an estimate of the contact stiffness to be suitably updated as shown in the remainder.

Let $\hat{\varepsilon}$ denote the time-varying estimate of the inverse of the contact stiffness coefficient

$$\varepsilon = k_{f,n}^{-1}; \quad (4.56)$$

then Equation (4.53) can be modified as

$$\phi = \hat{\varepsilon} \mathbf{f}_c + \dot{\hat{\varepsilon}} \psi \quad (4.57)$$

where ψ is the solution to the differential equation

$$\dot{\psi} + \lambda \psi = \mathbf{f}_c \quad (4.58)$$

with $\lambda > 0$ and $\dot{\hat{\varepsilon}}$ is computed according to the update law

$$\dot{\hat{\varepsilon}} = \gamma \psi^T \Delta \mathbf{f} \quad (4.59)$$

with $\gamma > 0$.

By observing that ε in (4.56) is a constant, Equation (4.57) can be rewritten as

$$\phi = \varepsilon \mathbf{f}_c - \tilde{\varepsilon} \mathbf{f}_c - \dot{\hat{\varepsilon}} \psi \quad (4.60)$$

where

$$\tilde{\varepsilon} = \varepsilon - \hat{\varepsilon} \quad (4.61)$$

denotes the estimate error. Then, folding (4.58) into (4.60) gives

$$\phi = \varepsilon \mathbf{f}_c - \dot{\zeta} - \lambda \zeta \quad (4.62)$$

where

$$\zeta = \tilde{\varepsilon} \psi. \quad (4.63)$$

Therefore, the force control action in (4.52) can be computed with ϕ as in (4.62) in lieu of (4.53). The resulting projection along \mathbf{n}_c gives

$$k_{Ap} \Delta \ddot{f}_n + k_{Vp} \Delta \dot{f}_n + \Delta f_n = k_{f,n} (\dot{\zeta}_n + \lambda \zeta_n). \quad (4.64)$$

It can be found that Δf_n and $\dot{\Delta f}_n$ tend to zero as long as the transfer function of the system described by (4.64) with input ζ_n and output Δf_n is *strictly positive real*; a sufficient condition to guarantee this is simply

$$\lambda < \frac{k_{Vp}}{k_{Ap}}. \quad (4.65)$$

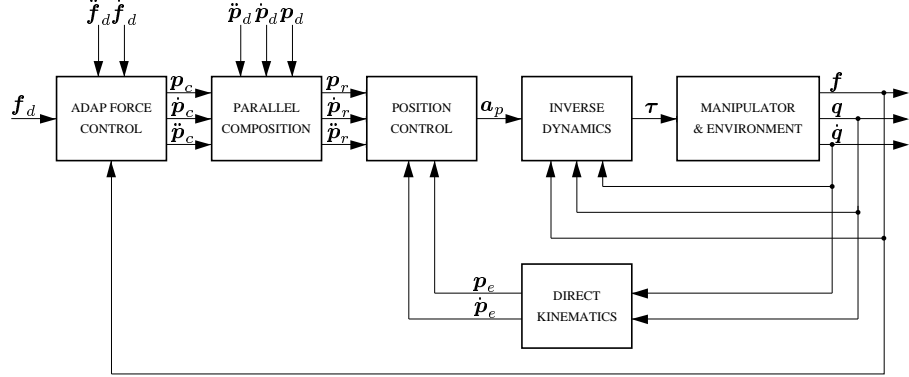


Figure 4.12. Force and position control with contact stiffness adaptation.

It can be concluded that *tracking* of the desired *contact force* is recovered thanks to the adaptation on the stiffness coefficient.

A block diagram of the resulting force and position control scheme with contact stiffness adaptation is sketched in Fig. 4.12. Compared to the scheme in Fig. 4.6, the derivatives of the desired contact force are input to the force control described by (4.52), (4.54), (4.57) and (4.58) which is then made adaptive according to (4.59) to allow for force tracking even with unknown stiffness.

3.2 EXPERIMENTS

The above force and position control schemes aimed at force tracking have been tested in *experiments* on the six-joint industrial robot described in Section 3. of Chapter 1 endowed with the force/torque sensor. Only the inner three joints are used while the outer three joints are mechanically braked.

Case study. The environment and the end effector are those described in Subsection 1.2 of Chapter 3. A task in the $Y_b Z_b$ -plane is assigned. An end-effector displacement of 0.12 m along Z_b and of 0.25 along Y_b is commanded. The trajectory along the path is generated according to a fifth-order interpolating polynomial with null initial and final velocities and accelerations, and a duration of 6 s after an initial lapse of 2 s. The surface of the cardboard box is nearly flat and is placed horizontally, i.e. in the $X_b Y_b$ -plane. Initially, the end effector is not in contact with the surface, and a null set point is assigned to the desired contact force. When the end effector comes in contact with the surface, i.e. when a nonnegligible force is sensed, the desired force along Z_b is taken to 40 N according to a fifth-order polynomial with null initial and final first and second time derivatives, and a duration of 1 s. The constant value is kept for 0.5 s, and then the desired force is taken back to zero in 1 s with the same polynomial as

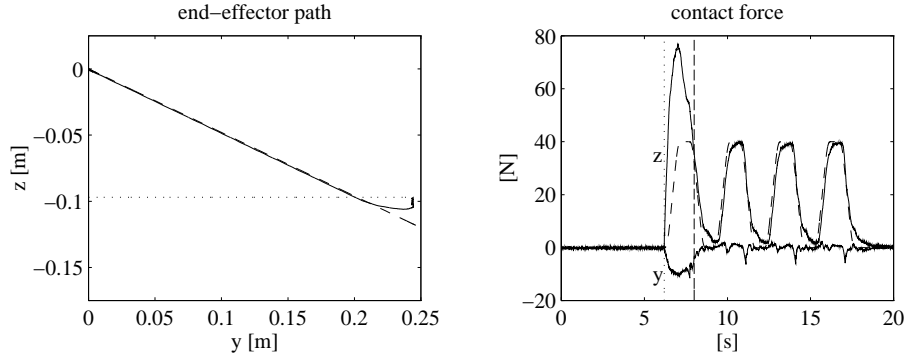


Figure 4.13. Experimental results under force and position control aimed at force tracking.

above, making a tooth-shaped profile. Then, the tooth is replicated three times with a 0.5 s lapse between each pair of teeth.

The task has first been executed using the force and position control scheme with feedforward of first and second derivatives of the contact force. The control gains in (4.31) have been set to $k_{Dp} = 90\mathbf{I}$ and $\mathbf{K}_{Pp} = 2500\mathbf{I}$. Also, the control gains in (4.54) have been set to $\mathbf{K}_{Ap} = 0.005\mathbf{I}$ and $\mathbf{K}_{Vp} = 0.15\mathbf{I}$ so as to achieve a satisfactory behavior with a design value of 15000 N/m for the stiffness coefficient $k_{f,n}$.

The experimental results are presented in Fig. 4.13 in terms of the end-effector path, together with the time history of the desired (dashed) and the actual (solid) contact force. As usual, the approximate location (dotted) of the surface is illustrated on the plot of the end-effector path, while the instant of contact (dotted line) is evidenced on the plot of the contact force. It can be recognized that a large peak occurs on the contact force along Z_b due to the nonnull velocity at the impact. Also, a time delay is experienced on the tracking of the reference force trajectory, whereas the appreciable deviation from zero of the component along Y_b is mainly due to contact friction. On the other hand, the position tracking performance is very good before the contact, whereas after the contact the end-effector position has to comply with the surface in view of the imposed desired force.

The above task has been repeated using the control scheme with contact stiffness adaptation. The values of the control gains are the same as before, while the control gains in (4.58) and (4.59) have been set to $\lambda = 20$ and $\gamma = 0.0001$. The initial estimate has been set so that $1/\hat{\varepsilon}(0) = 15000$, according to the above design value.

The experimental results are presented in Fig. 4.14 in terms of the end-effector path, together with the time history of the desired (dashed) and the actual (solid) contact force. As usual, the approximate location (dotted) of the surface is illustrated on the plot of the end-effector path, while the instant of

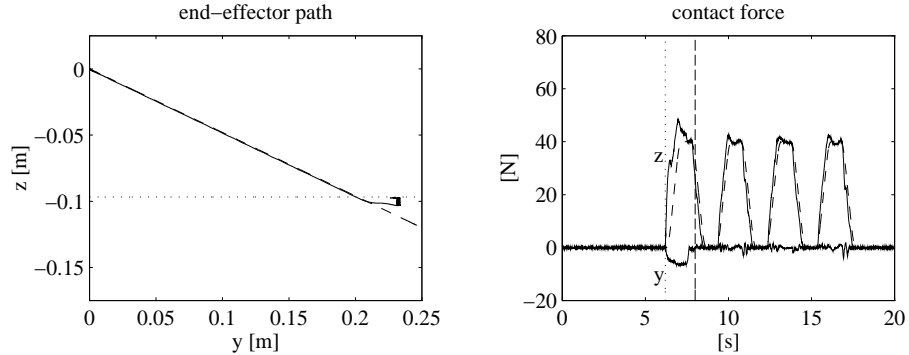


Figure 4.14. Experimental results under force and position control with contact stiffness adaptation.

contact (dotted line) is evidenced on the plot of the contact force. It can be recognized how the adaptation mechanism is capable of reducing the peak and ensuring good contact force tracking along Z_b . This is obtained at the expense of a larger end-effector position error along Y_b due to contact friction, since the force control action with stiffness adaptation operates on all the task directions.

4. FURTHER READING

Early work on force control can be found in [109]. The integral action for removing steady-state force errors has traditionally been used; its stability was proven in [108], while robustness with respect to force measurement delays was investigated in [104, 112].

The original idea of closing an outer force control loop around an inner position control loop dates back to [36]. This was a source of inspiration for the parallel approach to force/position control introduced in [24] using an inverse dynamics controller. The parallel force and position regulator was developed in [25]. The moment and orientation control has been derived in [72]. An experimental analysis of parallel control schemes has been carried out in [26], while an extensive comparison with the other force and motion control schemes presented in this chapter can be found in [29]. The extension of the force and position control scheme to the case of unknown stiffness with an adaptation mechanism has been proposed in [27] where a complete stability proof is given, while experimental tests are described in [28]. Another force and position control scheme with stiffness adaptation has been proposed in [114].

It has been generally recognized that force control may cause unstable behaviour during contact with environment. Dynamic models for explaining this phenomenon were introduced in [40]. Experimental investigations can be found in [2] and [103]. Emphasis on the problems with a stiff environment is given in [44]. Modelling of interaction between a manipulator and a dynamic

environment was presented in [33]. Moreover, control schemes are usually derived on the assumption that the manipulator end effector is in contact with the environment and this contact is not lost. Impact phenomena may occur which deserve careful consideration, and there is a need for global analysis of control schemes including the transition from non-contact into contact and vice-versa, e.g. [69, 101, 13].

Chapter 5

ADVANCED FORCE AND POSITION CONTROL

The model-based compensation requirements of the direct force control schemes in the previous chapter can be relaxed by resorting to an adaptive control acting on the estimates of the dynamic parameters. A regulation scheme and a passivity-based control scheme are developed with reference to the manipulator dynamics in the task space. Output feedback versions of the control schemes are derived to cope with the lack of joint velocity measurements. Experimental results of the advanced force and position control schemes are presented throughout the chapter.

1. TASK SPACE DYNAMICS

The interaction control schemes presented in the previous two chapters have been derived on the basis of the dynamic model of the robot manipulator in the joint space, as presented in Subsection 1.2 of Chapter 2. However, in order to derive *advanced force and position control* schemes, it is worth considering the *dynamics* directly in the *task space*. Further, in view of the difficulties evidenced for analyzing the performance of direct force control schemes aimed at controlling both contact force and contact moment, the coverage in this chapter is restricted only to force and position control.

With reference to the Lagrangian dynamics, for a three-joint nonredundant manipulator ($n = m = 3$), the components of the end-effector position \mathbf{p}_e constitute a set of generalized coordinates for the mechanical system as long as the Jacobian \mathbf{J}_p in (2.6) is nonsingular. Hence, the counterpart of the *dynamic model* (2.20) in the task space can be written as

$$\mathbf{B}_p(\mathbf{p}_e)\ddot{\mathbf{p}}_e + \mathbf{C}_p(\mathbf{p}_e, \dot{\mathbf{p}}_e)\dot{\mathbf{p}}_e + \mathbf{g}_p(\mathbf{p}_e) = \mathbf{u} - \mathbf{f} \quad (5.1)$$

where \mathbf{B}_p , \mathbf{C}_p and \mathbf{g}_p are related to \mathbf{B} , \mathbf{C} and \mathbf{g} as

$$\mathbf{B}_p = \mathbf{J}_p^{-T} \mathbf{B} \mathbf{J}_p^{-1} \quad (5.2)$$

$$\mathbf{C}_p = \mathbf{J}_p^{-T} \left(\mathbf{C} - \mathbf{B} \mathbf{J}_p^{-1} \dot{\mathbf{J}}_p \right) \mathbf{J}_p^{-1} \quad (5.3)$$

$$\mathbf{g}_p = \mathbf{J}_p^{-T} \mathbf{g}. \quad (5.4)$$

Notice that friction has been neglected for the sake of simplicity.

The vector \mathbf{u} in (5.1) represents the equivalent end-effector driving forces which are to be chosen according to some control strategy; then, the joint driving torques $\boldsymbol{\tau}$ can be computed as

$$\boldsymbol{\tau} = \mathbf{J}_p^T \mathbf{u}. \quad (5.5)$$

A number of useful properties of the dynamic model (5.1) are presented below which can be conceptually derived from the basic properties holding for the joint space dynamic model.

The inertia matrix \mathbf{B}_p is symmetric and positive definite. If B_m (B_M) denotes its minimum (maximum) eigenvalue, then in a finite region of the task space it is

$$0 < B_m \mathbf{I} \leq \mathbf{B}_p(\mathbf{p}_e) \leq B_M \mathbf{I} \quad (5.6)$$

with $B_M < \infty$.

The following identity holds

$$\dot{\mathbf{p}}_e^T \left(\dot{\mathbf{B}}_p(\mathbf{p}_e, \dot{\mathbf{p}}_e) - 2\mathbf{C}_p(\mathbf{p}_e, \dot{\mathbf{p}}_e) \right) \dot{\mathbf{p}}_e = 0. \quad (5.7)$$

This result is a direct consequence of the so-called *passivity* property of the manipulator dynamic model. Further, there exists a choice of matrix \mathbf{C}_p so that the matrix

$$\mathbf{N}_p(\mathbf{p}_e, \dot{\mathbf{p}}_e) = \dot{\mathbf{B}}_p(\mathbf{p}_e, \dot{\mathbf{p}}_e) - 2\mathbf{C}_p(\mathbf{p}_e, \dot{\mathbf{p}}_e) \quad (5.8)$$

is skew-symmetric; this also implies that

$$\dot{\mathbf{B}}_p(\mathbf{p}_e, \dot{\mathbf{p}}_e) = \mathbf{C}_p(\mathbf{p}_e, \dot{\mathbf{p}}_e) + \mathbf{C}_p^T(\mathbf{p}_e, \dot{\mathbf{p}}_e). \quad (5.9)$$

For this choice, \mathbf{C}_p satisfies:

$$\mathbf{C}_p(\mathbf{p}_e, \mathbf{v}_1) \mathbf{v}_2 = \mathbf{C}_p(\mathbf{p}_e, \mathbf{v}_2) \mathbf{v}_1 \quad (5.10)$$

$$\mathbf{C}_p(\mathbf{p}_e, \mathbf{v}_1 + \mathbf{v}_2) \mathbf{v}_3 = \mathbf{C}_p(\mathbf{p}_e, \mathbf{v}_1) \mathbf{v}_3 + \mathbf{C}_p(\mathbf{p}_e, \mathbf{v}_2) \mathbf{v}_3 \quad (5.11)$$

for all vectors \mathbf{v}_1 , \mathbf{v}_2 and \mathbf{v}_3 .

There exists a constant $0 < C_M < \infty$ so that

$$\|\mathbf{C}_p(\mathbf{p}_e, \dot{\mathbf{p}}_e)\| \leq C_M \|\dot{\mathbf{p}}_e\| \quad (5.12)$$

in a finite region of the task space.

The dynamic model (5.1) is linear in the parameters, i.e.

$$\mathbf{B}(\mathbf{p}_e)\ddot{\mathbf{p}}_e + \mathbf{C}_p(\mathbf{p}_e, \dot{\mathbf{p}}_e)\dot{\mathbf{p}}_e + \mathbf{g}_p(\mathbf{p}_e) = \mathbf{Y}_p(\mathbf{p}_e, \dot{\mathbf{p}}_e, \ddot{\mathbf{p}}_e)\boldsymbol{\pi} \quad (5.13)$$

where \mathbf{Y}_p is the $(3 \times p)$ regressor matrix and $\boldsymbol{\pi}$ is defined as in (2.21). In particular, the gravity forces can be written as

$$\mathbf{g}_p(\mathbf{p}_e) = \mathbf{G}_p(\mathbf{p}_e)\boldsymbol{\pi}_g \quad (5.14)$$

where \mathbf{G}_p is a $(3 \times r)$ matrix and $\boldsymbol{\pi}_g$ is an $(r \times 1)$ vector of dynamic parameters. Note that $r < p$ since gravity forces depend only on the mass and first moment of inertia of each link.

2. ADAPTIVE CONTROL

Any model-based compensation to be used by the control schemes presented in the previous three chapters relies on the exact knowledge of the dynamic parameters. These are typically determined via an identification procedure which provides accurate estimates of the parameters as the result of experimental tests executed on the real robot manipulator. Nevertheless, parameter mismatching always exists in practice and further adjustments of some parameters would be required in case of variable payloads. In such cases, it is possible to resort to an adaptation mechanism which provides an on-line update of the estimates of the dynamic parameters as a function of the relevant (motion and force) errors. To this purpose, *adaptive* versions of the *force and position control* schemes are developed in the sequel. First, the static model-based compensation is considered for *force and position regulation*. Then, the dynamic model-based compensation is treated for *force regulation* and *position tracking*.

2.1 REGULATION

With reference to the *force and position regulation* control scheme in Sub-section 2.1 of Chapter 4, the counterpart of the joint space control law (4.13) with (4.12), (4.11) and (4.5) can be written in the task space as

$$\mathbf{u} = k_{Pp}\Delta\mathbf{p}_{de} - k_{Dp}\dot{\mathbf{p}}_e + \mathbf{f}_d + k_{Fp}\Delta\mathbf{f} + k_{Ip}\int_0^t \Delta\mathbf{f} d\varsigma + \hat{\mathbf{g}}_p(\mathbf{p}_e) \quad (5.15)$$

where the control gains have all been taken as scalars and the damping action has been conveniently expressed in terms of the end-effector linear velocity; also, the quantity $\hat{\mathbf{g}}_p$ denotes the estimate of the gravity forces.

In case of perfect gravity compensation ($\hat{\mathbf{g}}_p = \mathbf{g}_p$), the end-effector position and contact force at the equilibrium are described by (4.18) and (4.19) as long as the desired force \mathbf{f}_d is taken along the normal \mathbf{n}_c to the contact plane.

A stability analysis around the equilibrium is carried out below as a useful premise to the case of imperfect gravity compensation (with adaptation). Let

$$\mathbf{e} = \mathbf{p}_{e,\infty} - \mathbf{p}_e \quad (5.16)$$

denote the deviation of the end-effector position from the equilibrium position. Then, by using (4.18), (3.9) and (4.15), Equation (5.16) can be rewritten as

$$\mathbf{e} = (\mathbf{I} - \mathbf{n}_c \mathbf{n}_c^T) \Delta \mathbf{p}_{de} + k_{f,n}^{-1} \Delta \mathbf{f} \quad (5.17)$$

where the first term is tangential to the contact plane while the second term is normal to the plane. Then, in view of (5.17), it is

$$\Delta \mathbf{f} = k_{f,n} \mathbf{n}_c \mathbf{n}_c^T \mathbf{e}. \quad (5.18)$$

Moreover, in view of (4.24) and (4.25), the deviation can be expressed as

$$\mathbf{e} = \Delta \mathbf{p}_{de} + d_n \mathbf{n}_c \quad (5.19)$$

representing a modified end-effector position error where d_n accounts for the presence of the environment and the desired force along the constrained task direction.

Computing the time derivative of (5.16) gives

$$\dot{\mathbf{e}} = -\dot{\mathbf{p}}_e. \quad (5.20)$$

Then, folding (5.15) in (5.1) and accounting for (5.18), (5.19) and (5.20) yields

$$\mathbf{B}_p(\mathbf{p}_e) \ddot{\mathbf{e}} + \mathbf{C}_p(\mathbf{p}_e, \dot{\mathbf{p}}_e) \dot{\mathbf{e}} + k_{Dp} \dot{\mathbf{e}} + k_{Pp} \mathbf{e} + k'_{Fp} k_{f,n} \mathbf{n}_c \mathbf{n}_c^T \mathbf{e} + k_{Ip} h \mathbf{n}_c = \mathbf{0} \quad (5.21)$$

where $k'_{Fp} = 1 + k_{Fp}$ and

$$h = \mathbf{n}_c^T \left(\int_0^t \Delta \mathbf{f} d\varsigma - k_{Pp} k_{Ip}^{-1} d_n \mathbf{n}_c \right). \quad (5.22)$$

Computing the time derivative of (5.22) and accounting for (5.18) gives

$$\dot{h} = k_{f,n} \mathbf{n}_c^T \mathbf{e}. \quad (5.23)$$

Equations (5.21) and (5.23) describe the closed-loop system in terms of the (7×1) state vector

$$\mathbf{z} = [\dot{\mathbf{e}}^T \quad \mathbf{e}^T \quad h]^T \quad (5.24)$$

as

$$\dot{\mathbf{z}} = \mathbf{A} \mathbf{z} \quad (5.25)$$

with

$$\mathbf{A} = \begin{bmatrix} -\mathbf{B}_p^{-1}(\mathbf{C}_p + k_{Dp} \mathbf{I}) & -\mathbf{B}_p^{-1}(k_{Pp} \mathbf{I} + k'_{Fp} k_{f,n} \mathbf{n}_c \mathbf{n}_c^T) & -k_{Ip} \mathbf{B}_p^{-1} \mathbf{n}_c \\ \mathbf{I} & \mathbf{O} & \mathbf{0} \\ \mathbf{0}^T & k_{f,n} \mathbf{n}_c^T & 0 \end{bmatrix}. \quad (5.26)$$

Notice that the origin of the state space represents the equilibrium of the system (5.25). Stability around this equilibrium can be ascertained as follows.

Consider the Lyapunov function candidate

$$\mathcal{V} = \frac{1}{2} \mathbf{z}^T \mathbf{P} \mathbf{z} \quad (5.27)$$

where

$$\mathbf{P} = \begin{bmatrix} \mathbf{B}_p & \mu \mathbf{B}_p & \mathbf{0} \\ \mu \mathbf{B}_p & (k_{Pp} + \mu k_{Dp}) \mathbf{I} + k'_{Fp} k_{f,n} \mathbf{n}_c \mathbf{n}_c^T & k_{Ip} \mathbf{n}_c \\ \mathbf{0}^T & k_{Ip} \mathbf{n}_c^T & \mu k_{Ip} k_{f,n}^{-1} \end{bmatrix} \quad (5.28)$$

with $\mu > 0$.

The function \mathcal{V} can be lower-bounded as

$$\begin{aligned} \mathcal{V} &\geq \frac{1}{2} [\|\dot{\mathbf{e}}\| \ \|\mathbf{e}\|] \begin{bmatrix} B_m & -\mu B_M \\ -\mu B_M & k_{Pp} + \mu k_{Dp} \end{bmatrix} \begin{bmatrix} \|\dot{\mathbf{e}}\| \\ \|\mathbf{e}\| \end{bmatrix} \\ &\quad + \frac{1}{2} [|\mathbf{n}_c^T \mathbf{e}| \ |h|] \begin{bmatrix} k'_{Fp} k_{f,n} & -k_{Ip} \\ -k_{Ip} & \mu k_{Ip} k_{f,n}^{-1} \end{bmatrix} \begin{bmatrix} |\mathbf{n}_c^T \mathbf{e}| \\ |h| \end{bmatrix}, \end{aligned} \quad (5.29)$$

where (5.6) has been used. Equation (5.29) reveals that \mathcal{V} is positive definite provided that

$$k_{Pp} > \frac{\mu^2 B_M^2}{B_m} - \mu k_{Dp} \quad (5.30)$$

$$k_{Ip} < \mu k'_{Fp}. \quad (5.31)$$

Computing the time derivative of \mathcal{V} along the trajectories of the system (5.25) and (5.26), and accounting for (5.7), yields

$$\begin{aligned} \dot{\mathcal{V}} &= -\dot{\mathbf{e}}^T (k_{Dp} \mathbf{I} - \mu \mathbf{B}_p) \dot{\mathbf{e}} + \mu \mathbf{e}^T \mathbf{C}_p^T \dot{\mathbf{e}} - \mu k_{Pp} \mathbf{e}^T \mathbf{e} \\ &\quad - (\mu k'_{Fp} - k_{Ip}) k_{f,n} (\mathbf{n}_c^T \mathbf{e})^2 \end{aligned} \quad (5.32)$$

where (5.9) has been used. In view of (5.6) and (5.12), the function $\dot{\mathcal{V}}$ can be upper-bounded as

$$\dot{\mathcal{V}} \leq -(k_{Dp} - \mu B_M - \mu C_M \|\mathbf{e}\|) \|\dot{\mathbf{e}}\|^2 - \mu k_{Pp} \|\mathbf{e}\|^2 - (\mu k'_{Fp} - k_{Ip}) k_{f,n} (\mathbf{n}_c^T \mathbf{e})^2. \quad (5.33)$$

Consider the region of the state space

$$\mathcal{Z} = \{\mathbf{z} : \|\mathbf{z}\| < \Phi\}. \quad (5.34)$$

Equation (5.33) reveals that $\dot{\mathcal{V}}$ is negative semidefinite in \mathcal{Z} provided that (5.31) holds and

$$0 < \Phi < \frac{k_{Dp} - \mu B_M}{\mu C_M}. \quad (5.35)$$

It can be recognized that $\dot{\mathcal{V}} = 0$ implies $\dot{e} = \mathbf{0}$ and $e = \mathbf{0}$. Then, in view of (5.21), in the largest invariant set containing the set where $\dot{\mathcal{V}} = 0$ it is $h = 0$. Asymptotic stability of $z = \mathbf{0}$ can be concluded from LaSalle theorem, implying *regulation of the contact force* along the constrained task direction and *regulation of the end-effector position* along the unconstrained task directions to their respective desired values.

It is worth remarking that the stiffness coefficient $k_{f,n}$ does not appear in the conditions (5.30), (5.31), which can be easily satisfied since μ is a free parameter not used by the control. Notice, however, that such conditions are only sufficient for asymptotic stability, i.e. stability may hold even though they are not satisfied.

In the case of imperfect gravity compensation ($\hat{\mathbf{g}}_p \neq \mathbf{g}_p$), a different equilibrium position is reached for the system (5.1) under the control (5.15), while contact force regulation is still achieved, i.e.

$$\hat{\mathbf{p}}_{e,\infty} = \mathbf{p}_{e,\infty} + k_{Pp}^{-1} \left(\mathbf{I} - \mathbf{n}_c \mathbf{n}_c^T \right) \left(\mathbf{g}_p(\hat{\mathbf{p}}_{e,\infty}) - \hat{\mathbf{g}}_p(\hat{\mathbf{p}}_{e,\infty}) \right) \quad (5.36)$$

$$\mathbf{f}_{e,\infty} = \mathbf{f}_d \quad (5.37)$$

showing that an error occurs on the end-effector position along the unconstrained task directions which can be reduced by suitably increasing the control gain k_{Pp} . The stability analysis for the closed-loop system is conceptually analogous to the case of perfect gravity compensation.

An effective way to recover the original equilibrium position is to make the force and position regulator *adaptive* with respect to the dynamic parameters in the gravity forces. By exploiting the linearity property in (5.14), the control law (5.15) can be rewritten as

$$\mathbf{u} = k_{Pp} \boldsymbol{\rho} - k_{Dp} \dot{\mathbf{p}}_e + \mathbf{f}_d + k_{Fp} \Delta \mathbf{f} + \mathbf{G}_p(\mathbf{p}_e) \hat{\boldsymbol{\pi}}_g \quad (5.38)$$

where $\hat{\boldsymbol{\pi}}_g$ is the vector of estimated parameters, and the position

$$\boldsymbol{\rho} = \Delta \mathbf{p}_{de} + k_{Pp}^{-1} k_{Ip} \int_0^t \Delta \mathbf{f} d\varsigma \quad (5.39)$$

has been made. The equations of the closed-loop system then become

$$\dot{\mathbf{z}} = \mathbf{A} \mathbf{z} + \boldsymbol{\eta} \quad (5.40)$$

with

$$\boldsymbol{\eta} = \begin{bmatrix} -\mathbf{B}_p^{-1} \mathbf{G}_p \hat{\boldsymbol{\pi}}_g \\ \mathbf{0} \\ 0 \end{bmatrix}, \quad (5.41)$$

where

$$\tilde{\boldsymbol{\pi}}_g = \boldsymbol{\pi}_g - \hat{\boldsymbol{\pi}}_g \quad (5.42)$$

is the parameter estimate error.

Consider the Lyapunov function candidate

$$\mathcal{V} = \frac{1}{2} \mathbf{z}^T \mathbf{Q} \mathbf{z} + \frac{1}{2} \tilde{\boldsymbol{\pi}}_g^T \boldsymbol{\Upsilon}_g \tilde{\boldsymbol{\pi}}_g \quad (5.43)$$

where $\boldsymbol{\Upsilon}_g$ is a symmetric and positive definite matrix and

$$\mathbf{Q} = \begin{bmatrix} \mathbf{B}_p & \mu \mathbf{B}_p & \varrho \mathbf{B}_p \mathbf{n}_c \\ \mu \mathbf{B}_p & (k_{Pp} + \mu k_{Dp}) \mathbf{I} + k'_{Fp} k_{f,n} \mathbf{n}_c \mathbf{n}_c^T & (k_{Ip} + \varrho k_{Dp}) \mathbf{n}_c \\ \varrho \mathbf{n}_c^T \mathbf{B}_p & (k_{Ip} + \varrho k_{Dp}) \mathbf{n}_c^T & \mu k_{Ip} k_{f,n}^{-1} + \varrho (k_{Pp} k_{f,n}^{-1} + k'_{Fp}) \end{bmatrix} \quad (5.44)$$

with $\varrho > 0$. Notice that \mathbf{Q} coincides with \mathbf{P} in (5.28) when $\varrho = 0$.

Computing the time derivative of \mathcal{V} along the trajectories of the system (5.40), (5.26) and (5.41), and accounting for (5.7), gives

$$\begin{aligned} \dot{\mathcal{V}} = & -\dot{\mathbf{e}}^T (k_{Dp} \mathbf{I} - \mu \mathbf{B}_p) \dot{\mathbf{e}} + (\mu \mathbf{e}^T + \varrho h \mathbf{n}_c^T) \mathbf{C}_p^T \dot{\mathbf{e}} - \mu k_{Pp} \mathbf{e}^T \mathbf{e} \\ & - (\mu k'_{Fp} - k_{Ip} - \varrho k_{Dp}) k_{f,n} (\mathbf{n}_c^T \mathbf{e})^2 - \varrho k_{Ip} h^2 + \varrho k_{f,n} \dot{\mathbf{e}}^T \mathbf{B}_p \mathbf{n}_c \mathbf{n}_c^T \mathbf{e} \\ & + (\dot{\mathbf{e}}^T + \mu \mathbf{e}^T + \varrho h \mathbf{n}_c^T) \mathbf{G}_p \tilde{\boldsymbol{\pi}}_g - \dot{\tilde{\boldsymbol{\pi}}}_g^T \boldsymbol{\Upsilon}_g \tilde{\boldsymbol{\pi}}_g \end{aligned} \quad (5.45)$$

where (5.9) has been used.

The last two terms in (5.45) suggest selecting the parameter estimate update as

$$\dot{\tilde{\boldsymbol{\pi}}}_g = \boldsymbol{\Upsilon}_g^{-1} \mathbf{G}_p^T (\dot{\mathbf{e}} + \mu \mathbf{e} + \varrho h \mathbf{n}_c) \quad (5.46)$$

so as to cancel them out. Notice that, in view of (5.19) and (5.22), it is worth choosing the free parameter ϱ as

$$\varrho = \mu k_{Pp}^{-1} k_{Ip} \quad (5.47)$$

which allows the adaptive law (5.46) to be computed in terms of physically measurable quantities (position, velocity and force) already used in the control law (5.38), i.e.

$$\dot{\tilde{\boldsymbol{\pi}}}_g = -\boldsymbol{\Upsilon}_g^{-1} \mathbf{G}_p^T (\dot{\mathbf{p}}_e - \mu \boldsymbol{\rho}) \quad (5.48)$$

with $\boldsymbol{\rho}$ in (5.39).

The function \mathcal{V} in (5.43) can be lower-bounded as

$$\begin{aligned} \mathcal{V} \geq & \frac{1}{2} [\|\dot{\mathbf{e}}\| \quad \|\mathbf{e}\|] \begin{bmatrix} B_m/2 & -\mu B_M \\ -\mu B_M & k_{Pp} + \mu k_{Dp} \end{bmatrix} [\|\dot{\mathbf{e}}\| \quad \|\mathbf{e}\|] \\ & + \frac{1}{2} [|\mathbf{n}_c^T \mathbf{e}| \quad |h|] \begin{bmatrix} k'_{Fp} k_{f,n} & -k_{Ip} - \varrho k_{Dp} \\ -k_{Ip} - \varrho k_{Dp} & \mu k_{Ip} k_{f,n}^{-1} \end{bmatrix} [|\mathbf{n}_c^T \mathbf{e}| \quad |h|] \end{aligned} \quad (5.49)$$

$$+ \frac{1}{2} \begin{bmatrix} \|\dot{\mathbf{e}}\| & |h| \end{bmatrix} \begin{bmatrix} B_m/2 & -\varrho B_M \\ -\varrho B_M & \varrho(k_{Pp}k_{f,n}^{-1} + k'_{Fp}) \end{bmatrix} \begin{bmatrix} \|\dot{\mathbf{e}}\| \\ |h| \end{bmatrix} \\ + \frac{1}{2} \tilde{\boldsymbol{\pi}}_g^T \boldsymbol{\Upsilon}_g \tilde{\boldsymbol{\pi}}_g$$

where (5.6) has been used.

On the other hand, by using (5.12) and the inequality

$$\dot{\mathbf{e}}^T \mathbf{B}_p \mathbf{n}_c \mathbf{n}_c^T \mathbf{e} \leq \frac{1}{2} B_M (\|\dot{\mathbf{e}}\|^2 + \|\mathbf{e}\|^2), \quad (5.50)$$

the function $\dot{\mathcal{V}}$ in (5.45) can be upper-bounded as

$$\begin{aligned} \dot{\mathcal{V}} \leq & -(k_{Dp} - \mu B_M - \mu C_M \|\mathbf{e}\| - \varrho k_{f,n} B_M/2 - \varrho C_M |h|) \|\dot{\mathbf{e}}\|^2 \\ & - (\mu k_{Pp} - \varrho k_{f,n} B_M/2) \|\mathbf{e}\|^2 \\ & - (\mu k'_{Fp} - k_{Ip} - \varrho k_{Dp}) k_{f,n} (\mathbf{n}_c^T \mathbf{e})^2 - \varrho k_{Ip} h^2. \end{aligned} \quad (5.51)$$

Consider the region (5.34) of the state space with

$$0 < \Phi < \frac{k_{Dp} k_{Pp}}{2\mu(k_{Pp} + k_{Ip}) C_M}. \quad (5.52)$$

Equations (5.49) and (5.51) reveal that \mathcal{V} is positive definite and $\dot{\mathcal{V}}$ is negative semidefinite in the region (5.34), provided that

$$k_{Ip} < \frac{2k_{Pp}^2}{k_{f,n} B_M} \quad (5.53)$$

$$k_{Dp} > \max \left\{ \frac{2\mu B_M^2}{B_m} - \frac{k_{Pp}}{\mu}, \mu B_M \left(2 + \frac{k_{Ip} k_{f,n}}{k_{Pp}} \right) \right\} \quad (5.54)$$

$$k'_{Fp} > \max \left\{ \frac{2\mu k_{Ip} B_M^2}{k_{Pp} B_m} - \frac{k_{Pp}}{k_{f,n}}, \frac{k_{Ip}}{\mu} \left(1 + \frac{\mu k_{Dp}}{k_{Pp}} \right)^2 \right\} \quad (5.55)$$

where (5.47) has been used.

Hence, the system (5.40) is stable around $\mathbf{z} = \mathbf{0}$ and $\tilde{\boldsymbol{\pi}}_g = \mathbf{0}$. It can be recognized that $\dot{\mathcal{V}} = 0$ implies $\dot{\mathbf{e}} = \mathbf{0}$ and $\mathbf{e} = \mathbf{0}$. Then, in view of (5.21), in the largest invariant set containing the set where $\dot{\mathcal{V}} = 0$ it is $h = 0$. Asymptotic stability of $\mathbf{z} = \mathbf{0}$ can be concluded from LaSalle theorem. Therefore, thanks to the adaptive law, *regulation* of the *contact force* to the desired value and of the *end-effector position* to the original equilibrium is recovered.

It is worth remarking that only the asymptotic convergence of \mathbf{z} to zero is ensured by the previous analysis, whereas the parameter estimate error $\tilde{\boldsymbol{\pi}}_g$ is

bounded without necessarily converging to zero. Also, the parameter μ is no longer free but is used in the adaptive law (5.48). Finally, the conditions (5.53), (5.54) and (5.55) now require a rough estimate of the contact stiffness coefficient. In particular, for a given choice of k_{Pp} , the gain k_{Ip} can be computed from (5.53), hence the gains k_{Dp} from (5.54) and k'_{Fp} from (5.55) sequentially. Remind, however, that such conditions are only sufficient.

2.2 PASSIVITY-BASED CONTROL

For the motion control problem, it is known that *passivity-based control* exhibits enhanced robustness with respect to inverse dynamics control, since it does not rely on the exact cancellation of nonlinear terms. The resulting control law is composed of a nonlinear model-based term and a linear compensator action. It is termed passivity-based because it is chosen so as to meet a desired energy function for the closed-loop system which preserves the passivity property of the manipulator dynamic model implied by (5.7).

For the interaction control problem, a passivity-based control is presented hereafter which is aimed at guaranteeing *tracking* of the desired *end-effector position* and *regulation* of the *contact force* to a desired value. This control is the natural premise to the case of imperfect model compensation (with adaptation). As in Subsection 2.2 of Chapter 4, the desired force \mathbf{f}_d is taken along the normal \mathbf{n}_c to the contact plane and the component of the desired position \mathbf{p}_d along \mathbf{n}_c is constant.

Consider the control law

$$\mathbf{u} = \hat{\mathbf{B}}_p(\mathbf{p}_e)\dot{\mathbf{r}} + \hat{\mathbf{C}}_p(\mathbf{p}_e, \dot{\mathbf{p}}_e)\mathbf{r} + \hat{\mathbf{g}}_p(\mathbf{p}_e) + \mathbf{f} + \lambda_1(\mathbf{r} - \dot{\mathbf{p}}_e) + \lambda_2\boldsymbol{\rho} \quad (5.56)$$

where $\lambda_1, \lambda_2 > 0$, $\boldsymbol{\rho}$ as in (5.39) and \mathbf{r} is a reference vector given by

$$\mathbf{r} = \dot{\mathbf{p}}_d + k_{Pp}\boldsymbol{\rho}; \quad (5.57)$$

also in (5.56) the quantities $\hat{\mathbf{B}}_p$, $\hat{\mathbf{C}}_p$ and $\hat{\mathbf{g}}_p$ denote the estimates of the respective quantities in the dynamic model (5.1).

On the assumption of perfect dynamic compensation ($\hat{\mathbf{B}}_p = \mathbf{B}_p$, $\hat{\mathbf{C}}_p = \mathbf{C}_p$, $\hat{\mathbf{g}}_p = \mathbf{g}_p$), folding (5.56) into (5.1) gives

$$\mathbf{B}_p(\mathbf{p}_e)\dot{\boldsymbol{\sigma}} + \mathbf{C}_p(\mathbf{p}_e, \dot{\mathbf{p}}_e)\boldsymbol{\sigma} + \lambda_1\boldsymbol{\sigma} + \lambda_2\boldsymbol{\rho} = \mathbf{0}, \quad (5.58)$$

where

$$\boldsymbol{\sigma} = \mathbf{r} - \dot{\mathbf{p}}_e = \Delta\dot{\mathbf{p}}_{de} + k_{Pp}\boldsymbol{\rho}. \quad (5.59)$$

In view of (5.19) and (5.22), the vector $\boldsymbol{\rho}$ in (5.39) can be rewritten as

$$\boldsymbol{\rho} = \boldsymbol{\epsilon} + k_{Pp}^{-1}k_{Ip}h\mathbf{n}_c. \quad (5.60)$$

Also, in view of (5.59) and (5.60), the time derivative of the end-effector deviation from the equilibrium position in (5.19) can be written as

$$\dot{\mathbf{e}} = \Delta \dot{\mathbf{p}}_{de} = \boldsymbol{\sigma} - k_{Pp} \mathbf{e} - k_{Ip} h \mathbf{n}_c. \quad (5.61)$$

Thus Equation (5.58) becomes

$$\mathbf{B}_p(\mathbf{p}_e) \dot{\boldsymbol{\sigma}} + \mathbf{C}_p(\mathbf{p}_e, \dot{\mathbf{p}}_e) \boldsymbol{\sigma} + \lambda_1 \boldsymbol{\sigma} + \lambda_2 \mathbf{e} + \lambda_2 k_{Pp}^{-1} k_{Ip} h \mathbf{n}_c = \mathbf{0}. \quad (5.62)$$

Equations (5.62), (5.61) and (5.23) describe the closed-loop system in terms of the (7×1) state vector

$$\mathbf{z}' = [\boldsymbol{\sigma}^T \quad \mathbf{e}^T \quad h]^T \quad (5.63)$$

as

$$\dot{\mathbf{z}}' = \mathbf{A}' \mathbf{z}' \quad (5.64)$$

with

$$\mathbf{A}' = \begin{bmatrix} -\mathbf{B}_p^{-1}(\mathbf{C}_p + \lambda_1 \mathbf{I}) & -\lambda_2 \mathbf{B}_p^{-1} & -\lambda_2 k_{Pp}^{-1} k_{Ip} \mathbf{B}_p^{-1} \mathbf{n}_c \\ \mathbf{I} & -k_{Pp} \mathbf{I} & -k_{Ip} \mathbf{n}_c \\ \mathbf{0}^T & k_{f,n} \mathbf{n}_c^T & 0 \end{bmatrix}. \quad (5.65)$$

Notice that the origin of the state space represents the equilibrium of the system (5.64). Stability around this equilibrium can be ascertained as follows.

Consider the Lyapunov function candidate

$$\mathcal{V} = \frac{1}{2} \mathbf{z}'^T \mathbf{P}' \mathbf{z}' \quad (5.66)$$

with

$$\mathbf{P}' = \begin{bmatrix} \mathbf{B}_p & \mathbf{O} & \mathbf{0} \\ \mathbf{O} & \lambda_2 \mathbf{I} & \lambda_2 k_{Pp}^{-1} k_{Ip} \mathbf{n}_c \\ \mathbf{0}^T & \lambda_2 k_{Pp}^{-1} k_{Ip} \mathbf{n}_c^T & \lambda_2 k_{Ip} k_{f,n}^{-1} \end{bmatrix}. \quad (5.67)$$

The function \mathcal{V} can be lower-bounded as

$$\mathcal{V} \geq \frac{1}{2} B_m \|\boldsymbol{\sigma}\|^2 + \frac{1}{2} \lambda_2 [\|\mathbf{e}\| \quad |h|] \begin{bmatrix} 1 & -k_{Pp}^{-1} k_{Ip} \\ -k_{Pp}^{-1} k_{Ip} & k_{Ip} k_{f,n}^{-1} \end{bmatrix} \begin{bmatrix} \|\mathbf{e}\| \\ |h| \end{bmatrix}. \quad (5.68)$$

where (5.6) has been used. Computing the time derivative of \mathcal{V} along the trajectories of the system (5.64), and accounting for (5.8), gives

$$\begin{aligned} \dot{\mathcal{V}} = & -\lambda_1 \boldsymbol{\sigma}^T \boldsymbol{\sigma} - \lambda_2 k_{Pp} \mathbf{e}^T \mathbf{e} + \lambda_2 k_{Pp}^{-1} k_{Ip} k_{f,n} (\mathbf{n}_c^T \mathbf{e})^2 \\ & - \lambda_2 k_{Pp}^{-1} k_{Ip}^2 h^2 - \lambda_2 k_{Ip} h \mathbf{n}_c^T \mathbf{e}. \end{aligned} \quad (5.69)$$

It is easy to see from (5.69) and (5.68) that \mathcal{V} is positive definite and $\dot{\mathcal{V}}$ is negative definite provided that

$$k_{Pp}^2 > \frac{4}{3}k_{Ip}k_{f,n} \quad (5.70)$$

holds. Therefore, asymptotic stability of $\mathbf{z}' = \mathbf{0}$ can be concluded, implying *regulation* of the *contact force* along the constrained task direction and *tracking* of the *end-effector position* along the unconstrained task directions to their respective desired values.

It is worth remarking that condition (5.70) can be satisfied for a suitable choice of k_{Pp} and k_{Ip} with a given estimate of the contact stiffness coefficient $k_{f,n}$. Also, stability holds for any λ_1 and λ_2 which are then available to meet design specifications on system performance.

Notice that the last term on the right-hand side of (5.56) is not strictly needed in the controller, and in fact it is possible to prove stability even without it. Nevertheless, such term will be useful for the observer design to follow in the next section.

In the case of imperfect model compensation, the passivity-based control can be made *adaptive* with respect to the dynamic parameters as follows. By exploiting the linearity property in (5.13), the control law (5.56) can be rewritten as

$$\mathbf{u} = \mathbf{Y}_p(\mathbf{p}_e, \dot{\mathbf{p}}_e, \mathbf{r}, \dot{\mathbf{r}})\hat{\boldsymbol{\pi}} + \mathbf{f} + \lambda_1(\mathbf{r} - \dot{\mathbf{p}}_e) + \lambda_2\boldsymbol{\rho} \quad (5.71)$$

where $\hat{\boldsymbol{\pi}}$ is the vector of estimated parameters. The equations of the closed-loop system become

$$\dot{\mathbf{z}}' = \mathbf{A}'\mathbf{z}' + \boldsymbol{\eta}' \quad (5.72)$$

with \mathbf{A}' as in (5.65) and

$$\boldsymbol{\eta}' = \begin{bmatrix} -\mathbf{B}_p^{-1}\mathbf{Y}_p\tilde{\boldsymbol{\pi}} \\ \mathbf{0} \\ 0 \end{bmatrix} \quad (5.73)$$

where

$$\tilde{\boldsymbol{\pi}} = \boldsymbol{\pi} - \hat{\boldsymbol{\pi}} \quad (5.74)$$

is the parameter estimate error.

Consider the Lyapunov function candidate

$$\mathcal{V} = \frac{1}{2}\mathbf{z}'^T \mathbf{P}' \mathbf{z}' + \frac{1}{2}\tilde{\boldsymbol{\pi}}^T \boldsymbol{\Upsilon} \tilde{\boldsymbol{\pi}} \quad (5.75)$$

with \mathbf{P}' as in (5.67) and $\boldsymbol{\Upsilon}$ a symmetric and positive definite matrix.

It is easy to see that choosing the parameter estimate update law as

$$\dot{\hat{\boldsymbol{\pi}}} = \boldsymbol{\Upsilon}^{-1} \mathbf{Y}_p^T \boldsymbol{\sigma} \quad (5.76)$$

yields the same time derivative of \mathcal{V} as in (5.69), which is negative semidefinite provided that (5.70) holds. Hence, the system (5.72) is stable around $z' = \mathbf{0}$ and $\hat{\pi} = \mathbf{0}$, and asymptotic stability of z' can be concluded from Barbalat lemma. Therefore, thanks to the adaptive law, *regulation* of the *contact force* to the desired value and *tracking* of the desired *end-effector position* is recovered.

The passivity-based adaptive control has been derived in the task space. Since control actions are to be realized by the joint actuators, it is worth carrying out the implementation in the joint space. By using the relationship between the dynamics in the joint space and the dynamics in the task space established by (5.2), (5.3), (5.4) and (5.5), the counterpart of the control law (5.71) in the joint space is given by

$$\boldsymbol{\tau} = \mathbf{Y}(\boldsymbol{q}, \dot{\boldsymbol{q}}, \boldsymbol{\varrho}, \dot{\boldsymbol{\varrho}}) \hat{\pi} + \mathbf{J}_p^T(\boldsymbol{q}) (\mathbf{f} + \lambda_1 \mathbf{J}_p(\boldsymbol{q})(\boldsymbol{\varrho} - \dot{\boldsymbol{q}}) + \lambda \boldsymbol{\rho}) \quad (5.77)$$

where \mathbf{Y} is the regressor in the joint space defined in (2.21), \mathbf{J}_p is the Jacobian in (2.6), and

$$\boldsymbol{\varrho} = \mathbf{J}_p^{-1}(\boldsymbol{q}) \mathbf{r} \quad (5.78)$$

$$\dot{\boldsymbol{\varrho}} = \mathbf{J}_p^{-1}(\boldsymbol{q}) (\dot{\mathbf{r}} - \dot{\mathbf{J}}_p(\boldsymbol{q}, \dot{\boldsymbol{q}}) \boldsymbol{\varrho}) . \quad (5.79)$$

Further, the counterpart of the adaptive law (5.76) in the joint space is given by

$$\dot{\hat{\pi}} = \boldsymbol{\Upsilon}^{-1} \mathbf{Y}^T(\boldsymbol{\varrho} - \dot{\boldsymbol{q}}) . \quad (5.80)$$

2.3 EXPERIMENTS

The above adaptive passivity-based control scheme has been tested in *experiments* on the six-joint industrial robot described in Section 3. of Chapter 1 endowed with the force/torque sensor; only the second and third joint are used while the others are mechanically braked. A minimum set of dynamic parameters for the manipulator is reported in Appendix B.

Case study. The environment and the end effector are those described in Subsection 1.2 of Chapter 3. The task consists of a straight-line motion in the $X_b Z_b$ -plane with an end-effector (horizontal) displacement of 0.1 m along X_b . The trajectory along the path is generated according to a trapezoidal velocity profile with cubic blends and null initial and final velocities and accelerations; the actual duration of the motion is 3 s after an initial lapse. The surface of the cardboard box is nearly flat and is placed (vertically) in the $Y_b Z_b$ -plane in such a way as to obstruct the desired end-effector motion along X_b . To begin, a null set point is assigned to the contact force; when the end effector comes into contact with the environment, i.e. a nonnegligible force is sensed, the desired

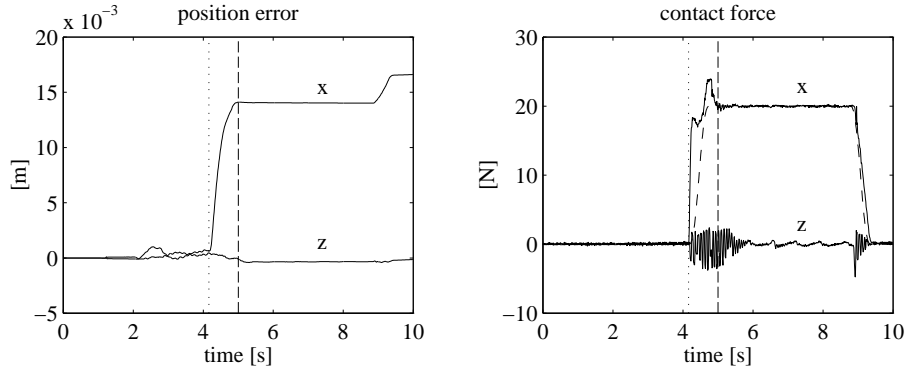


Figure 5.1. Experimental results under passivity-based force and position control with exact parameter estimation.

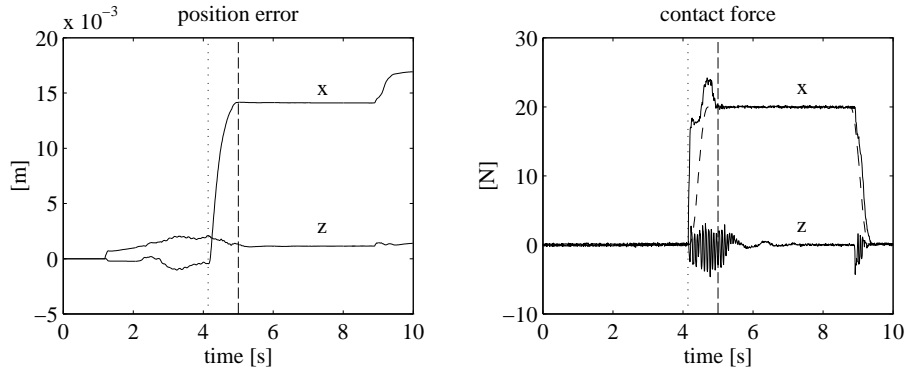


Figure 5.2. Experimental results under passivity-based force and position control with inexact parameter estimation.

force along X_b is taken to 20 N according to the same kind of interpolating polynomial as for the position, with null initial and final first and second time derivatives, and an actual duration of 0.6 s. The constant value is kept for 4 s, and then the desired force is taken back to zero in 0.6 s with the same polynomial as above.

The task has first been executed using the force and position passivity-based control scheme with exact parameter estimation. The control gains in (5.77) and (5.39) have been set to $\lambda_1 = 1700$, $\lambda_2 = 0$, $k_{Pp} = 40$ and $k_{Ip} = 0.1$ in order to guarantee a well-damped behavior during the unconstrained motion, as well as to satisfy condition (5.70) with the given stiffness estimate during the constrained motion.

The experimental results are presented in Fig. 5.1 in terms of the time history of the desired (dashed) and actual (solid) contact forces, and the time

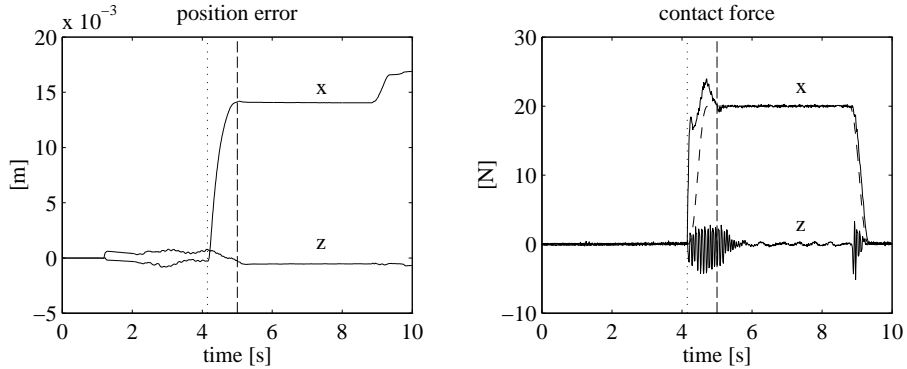


Figure 5.3. Experimental results under passivity-based force and position control with inexact parameter estimation and adaptation.

history of the X_b -component and Z_b -component of the end-effector position error. As usual, the approximate location (dotted) of the surface is illustrated on the plot of the end-effector path, while the instant of contact (dotted line) is evidenced on the plot of the contact force. It can be recognized that after a transient the contact force reaches the desired value, thanks to the integral action; the peak on the component along X_b is due to the nonnull value of the end-effector velocity at the contact, as well as to the imposed motion, whereas the appreciable deviation from zero of the component along Z_b is mainly due to contact friction. On the other hand, the position error along Z_b is very small, whereas a significant position error occurs after the contact along X_b that is caused by the presence of the surface, as well as by the imposed nonnull desired force.

The above task has been repeated using the passivity-based control scheme with inexact parameter estimation. The control gains are unchanged.

The experimental results are presented in Fig. 5.2 in terms of the time history of the desired (dashed) and actual (solid) contact forces, and the time history of the X_b -component and Z_b -component of the end-effector position error. It can be recognized that the time history of the contact force is practically the same, while an appreciable position error occurs along Z_b .

Finally, the task has been executed using the passivity-based control scheme with inexact parameter estimation and adaptation. The control gains in (5.77) and (5.39) are the same as above. Adaptation is performed with respect to a reduced set of five dynamic parameters which are affected by uncertainty on the third link; the matrix gain of the adaptive law (5.80) has been set to $\Upsilon = 70\mathbf{I}$. In order to test the effectiveness of the control scheme in the face of parameter uncertainty, the estimated dynamic parameters of the third link have

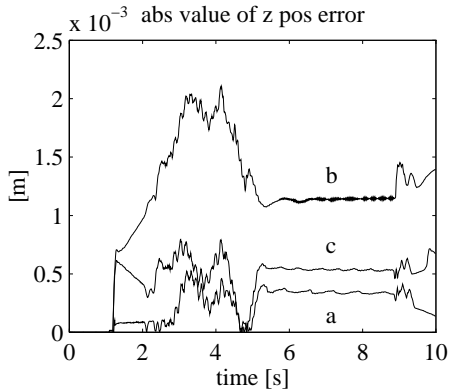


Figure 5.4. Comparison of performance with passivity-based force and position control schemes.

been modified assuming that a payload of 10 kg mass is concentrated at the end effector.

The experimental results are presented in Fig. 5.3 in terms of the time history of the desired (dashed) and actual (solid) contact forces, and the time history of the X_b -component and Z_b -component of the end-effector position error. It can be recognized that the position error along Z_b is successfully recovered by resorting to the adaptive action on the parameter estimates.

Indeed, the performance of the three control schemes along the unconstrained task direction can be evaluated in terms of the position error along Z_b as in Fig. 5.4. Thanks to parameter adaptation, the behaviour of the system with the adaptive control scheme (c) is better than with the control scheme without adaptation and inexact parameter estimation (b), and it can be compared favorably with the control scheme using exact parameter estimation (a).

3. OUTPUT FEEDBACK CONTROL

All previous force and position control schemes require *full-state feedback* of the contact force and the end-effector position and velocity. The force is directly measured by using a force sensor mounted at the robot wrist. The position can be computed from the joint position measurements via the direct kinematics, whereas the velocity could be computed from the joint velocity measurements via the differential kinematics of the manipulator. A problem exists, however, for those robots having only joint encoders or resolvers for measuring positions, but no tachometers for measuring joint velocities. Therefore, it is worth devising suitable *output feedback control* schemes that do not require velocity measurements. In the remainder, two solutions are presented which regard the *force and position regulation* control scheme and the *passivity-based control* scheme discussed above.

3.1 REGULATION

If the end-effector velocity $\dot{\mathbf{p}}_e$ is not available, it is possible to modify the control law (5.15) as

$$\mathbf{u} = k_{Pp}\boldsymbol{\rho} - k_{Dp}\boldsymbol{\theta} + \mathbf{f}_d + k_{Fp}\Delta\mathbf{f} - k_\chi\boldsymbol{\chi} + \hat{\mathbf{g}}_p(\mathbf{p}_e) \quad (5.81)$$

where $\boldsymbol{\rho}$ is defined in (5.39), $k_\chi > 0$, while $\boldsymbol{\theta}$ and $\boldsymbol{\chi}$ are respectively obtained from

$$\dot{\boldsymbol{\theta}} + \alpha_1\boldsymbol{\theta} = \alpha_2\dot{\mathbf{p}}_e \quad (5.82)$$

$$\dot{\boldsymbol{\chi}} + \alpha_1\boldsymbol{\chi} = \alpha_2\Delta\mathbf{f} \quad (5.83)$$

with $\alpha_1, \alpha_2 > 0$. The vector $\boldsymbol{\theta}$ in (5.82) provides an estimate of the end-effector velocity through a *linear observer* (lead filter), whereas the vector $\boldsymbol{\chi}$ in (5.83) corresponds to a filtering action on the force error. It is worth pointing out that, with respect to the control law (5.15), the velocity $\dot{\mathbf{p}}_e$ has been replaced with the estimate $\boldsymbol{\theta}$ while the term $-k_\chi\boldsymbol{\chi}$ has been introduced for stability purposes as illustrated in the sequel.

By assuming that the initial conditions for (5.82) and (5.83) are assigned as $\boldsymbol{\theta}(0) = \mathbf{0}$ and $\boldsymbol{\chi}(0) = \alpha_1^{-1}\alpha_2\Delta\mathbf{f}(0)$, the following equality holds

$$\boldsymbol{\chi} = \alpha_1^{-1}(k_{f,n}\mathbf{n}_c\mathbf{n}_c^T\boldsymbol{\theta} + \alpha_2\Delta\mathbf{f}). \quad (5.84)$$

In fact, taking the time derivative of (5.84) and using (5.82), (5.18) and (5.20) yields

$$\dot{\boldsymbol{\chi}} = -k_{f,n}\mathbf{n}_c\mathbf{n}_c^T\boldsymbol{\theta} \quad (5.85)$$

and it is easy to verify that Equation (5.83) is satisfied by (5.84) and (5.85).

Folding (5.81) in (5.1), and accounting for (5.18), (5.19), (5.20) and (5.39), yields

$$\mathbf{B}_p(\mathbf{p}_e)\ddot{\mathbf{e}} + \mathbf{C}_p(\mathbf{p}_e, \dot{\mathbf{p}}_e)\dot{\mathbf{e}} - k_{Dp}\boldsymbol{\theta} + k_{Pp}\mathbf{e} + h_\theta\mathbf{n}_c = \mathbf{0} \quad (5.86)$$

where

$$h_\theta = \mathbf{n}_c^T(k'_{Fp}k_{f,n}\mathbf{e} + k_{Ip}h\mathbf{n}_c - k_\chi\boldsymbol{\chi}) \quad (5.87)$$

with h as in (5.22) and $\hat{\mathbf{g}}_p = \mathbf{g}_p$.

Computing the time derivative of (5.87), and accounting for (5.23) and (5.85), gives

$$\dot{h}_\theta = k_{f,n}\mathbf{n}_c^T(k'_{Fp}\dot{\mathbf{e}} + k_{Ip}\mathbf{e} + k_\chi\boldsymbol{\theta}). \quad (5.88)$$

Equations (5.86), (5.82) and (5.88) describe the closed-loop system in terms of the (10×1) state vector

$$\mathbf{w} = [\dot{\mathbf{e}}^T \quad \mathbf{e}^T \quad \boldsymbol{\theta}^T \quad h_\theta]^T \quad (5.89)$$

as

$$\dot{\mathbf{w}} = \mathbf{V}\mathbf{w} \quad (5.90)$$

with

$$\mathbf{V} = \begin{bmatrix} -\mathbf{B}_p^{-1}\mathbf{C}_p & -k_{Pp}\mathbf{B}_p^{-1} & k_{Dp}\mathbf{B}_p^{-1} & -\mathbf{B}_p^{-1}\mathbf{n}_c \\ \mathbf{I} & \mathbf{O} & \mathbf{O} & \mathbf{0} \\ -\alpha_2\mathbf{I} & \mathbf{O} & -\alpha_1\mathbf{I} & \mathbf{0} \\ k_{f,n}k'_{Fp}\mathbf{n}_c^T & k_{f,n}k_{Ip}\mathbf{n}_c^T & k_{f,n}k_{\chi}\mathbf{n}_c^T & 0 \end{bmatrix}. \quad (5.91)$$

The origin of the state space gives the equilibrium of the system (5.90). Stability around this equilibrium can be ascertained as follows.

Consider the Lyapunov function candidate

$$\mathcal{V} = \frac{1}{2}\mathbf{w}^T \mathbf{X} \mathbf{w} \quad (5.92)$$

where

$$\mathbf{X} = \begin{bmatrix} \mathbf{B}_p & \mu_1\mathbf{B}_p & \mu_1\mu_2\mathbf{B}_p & \mathbf{0} \\ \mu_1\mathbf{B}_p & k_{Pp}\mathbf{I} & \mathbf{O} & \mathbf{0} \\ \mu_1\mu_2\mathbf{B}_p & \mathbf{O} & \alpha_2^{-1}k_{Dp}\mathbf{I} & \mathbf{0} \\ \mathbf{0}^T & \mathbf{0}^T & \mathbf{0}^T & (k'_{Fp}k_{f,n})^{-1} \end{bmatrix} \quad (5.93)$$

with

$$\mu_1 = k'_{Fp}^{-1}k_{Ip} \quad (5.94)$$

$$\mu_2 = k_{Pp}^{-1}k_{Dp}. \quad (5.95)$$

The function \mathcal{V} can be lower-bounded as

$$\begin{aligned} \mathcal{V} &\geq \frac{1}{2} [\|\dot{\mathbf{e}}\| \quad \|\mathbf{e}\|] \begin{bmatrix} B_m/2 & -\mu_1 B_M \\ -\mu_1 B_M & k_{Pp} \end{bmatrix} \begin{bmatrix} \|\dot{\mathbf{e}}\| \\ \|\mathbf{e}\| \end{bmatrix} \\ &\quad + \frac{1}{2} [\|\dot{\mathbf{e}}\| \quad \|\boldsymbol{\theta}\|] \begin{bmatrix} B_m/2 & -\mu_1\mu_2 B_M \\ -\mu_1\mu_2 B_M & \alpha_2^{-1}k_{Dp} \end{bmatrix} \begin{bmatrix} \|\dot{\mathbf{e}}\| \\ \|\boldsymbol{\theta}\| \end{bmatrix} + \frac{1}{2}(k'_{Fp}k_{f,n})^{-1}h_{\theta}^2 \end{aligned} \quad (5.96)$$

where (5.6) has been used. Equation (5.96) with (5.94) and (5.95) reveals that \mathcal{V} is positive definite provided that

$$k_{Ip}^2 < \frac{B_m k_{Pp} k'_{Fp}^2}{2B_M^2} \min \left\{ 1, \frac{k_{Pp}}{\alpha_2 k_{Dp}} \right\}. \quad (5.97)$$

Computing the time derivative of \mathcal{V} along the trajectories of the system (5.90) and (5.91), and accounting for (5.7), gives

$$\begin{aligned} \dot{\mathcal{V}} &= -\mu_1(\mu_2\alpha_2 - 1)\dot{\mathbf{e}}^T \mathbf{B}_p \dot{\mathbf{e}} - \mu_1 k_{Pp} \mathbf{e}^T \mathbf{e} \\ &\quad - (\alpha_1\alpha_2^{-1} - \mu_1\mu_2)k_{Dp} \boldsymbol{\theta}^T \boldsymbol{\theta} - \mu_1\mu_2\alpha_1 \boldsymbol{\theta}^T \mathbf{B}_p \dot{\mathbf{e}} \\ &\quad + \mu_1(\mathbf{e}^T + \mu_2 \boldsymbol{\theta}^T) \mathbf{C}^T \dot{\mathbf{e}}, \end{aligned} \quad (5.98)$$

where (5.6) has been used and the choice

$$k_\chi = \mu_2 k_{Ip} = k_{Pp}^{-1} k_{Dp} k_{Ip} \quad (5.99)$$

has been made in order to cancel out the cross terms $-\mu_1 \mu_2 \boldsymbol{\theta}^T \mathbf{n}_c h_\theta$ and $h_\theta k_{Fp}'^{-1} k_\chi \mathbf{n}_c^T \boldsymbol{\theta}$. In view of (5.6) and (5.12), the function \mathcal{V} can be upper-bounded as

$$\begin{aligned} \dot{\mathcal{V}} &\leq -\frac{1}{2} \mu_1 (\mu_2 \alpha_2 B_m - 2B_M - 2C_M \|\mathbf{e}\| - 2\mu_2 C_M \|\boldsymbol{\theta}\|) \|\dot{\mathbf{e}}\|^2 \quad (5.100) \\ &\quad - \frac{1}{2} k_{Dp} (\alpha_1 \alpha_2^{-1} - 2\mu_1 \mu_2) \|\boldsymbol{\theta}\|^2 - \mu_1 k_{Pp} \|\mathbf{e}\|^2 \\ &\quad - \frac{1}{2} [\|\dot{\mathbf{e}}\| \quad \|\boldsymbol{\theta}\|] \begin{bmatrix} \mu_1 \mu_2 \alpha_2 B_m & -\mu_1 \mu_2 \alpha_1 B_M \\ -\mu_1 \mu_2 \alpha_1 B_M & \alpha_1 \alpha_2^{-1} k_{Dp} \end{bmatrix} \begin{bmatrix} \|\dot{\mathbf{e}}\| \\ \|\boldsymbol{\theta}\| \end{bmatrix}. \end{aligned}$$

Consider the region of the state space

$$\mathcal{W} = \{\mathbf{w} : \|\mathbf{w}\| < \Theta\}. \quad (5.101)$$

Equation (5.100) with (5.94) and (5.95) reveals that $\dot{\mathcal{V}}$ is negative semidefinite in \mathcal{W} provided that

$$k_{Ip} < k_{Pp} k_{Fp}' \min \left\{ \frac{\alpha_1}{2\alpha_2 k_{Dp}}, \frac{B_m}{\alpha_1 B_M^2} \right\} \quad (5.102)$$

$$0 < \Theta < \frac{\alpha_2 k_{Dp} B_m - 2k_{Pp} B_M}{2(k_{Pp} + k_{Dp}) C_M}. \quad (5.103)$$

It can be recognized that $\dot{\mathcal{V}} = 0$ implies $\dot{\mathbf{e}} = \mathbf{0}$, $\mathbf{e} = \mathbf{0}$ and $\boldsymbol{\theta} = \mathbf{0}$. Then, in view of (5.86), in the largest invariant set containing the set where $\dot{\mathcal{V}} = 0$ it is $h_\theta = 0$. Asymptotic stability of $\mathbf{w} = \mathbf{0}$ can be concluded from LaSalle theorem. Therefore, thanks to the linear observer, *regulation* of the *contact force* and of the *end-effector position* to their respective desired values is ensured.

It is worth remarking that the expression of the Lyapunov function is more complex than in the full-state feedback case, since the additional parameters μ_1 and μ_2 are no longer free but they need to be related to the control gains as in (5.94) and (5.95) in order to simplify the proof. Likewise, the gain k_χ is related to the control gains as in (5.99). Notice that the gains k_{Dp} and k_{Pp} can be chosen to satisfy (5.103); then, k_{Fp}' and k_{Ip} are chosen to satisfy (5.97) and (5.102).

3.2 PASSIVITY-BASED CONTROL

If the end-effector velocity $\dot{\mathbf{p}}_e$ is not available, it is possible to modify the control law (5.56) as

$$\mathbf{u} = \mathbf{B}_p(\mathbf{p}_e) \dot{\mathbf{r}}_\nu + \mathbf{C}_p(\mathbf{p}_e, \boldsymbol{\nu}) \mathbf{r}_\nu + \mathbf{g}_p(\mathbf{p}_e) + \mathbf{f} + \lambda_1(\mathbf{r}_\nu - \boldsymbol{\nu}) + \lambda_2 \boldsymbol{\rho} \quad (5.104)$$

where perfect dynamic compensation has been assumed. Consider also the *nonlinear observer*

$$\dot{\tilde{\mathbf{p}}}_e = \boldsymbol{\kappa} - (k_{Pp} + k_O)\tilde{\mathbf{p}}_e \quad (5.105)$$

$$\boldsymbol{\kappa} = \dot{\mathbf{r}}_\nu + \lambda_2 \mathbf{B}_p^{-1}(\mathbf{p}_e)(\boldsymbol{\rho} - \tilde{\mathbf{p}}_e) - k_{Pp}k_O\tilde{\mathbf{p}}_e \quad (5.106)$$

with $k_O > 0$, where

$$\mathbf{r}_\nu = \dot{\mathbf{p}}_d + k_{Pp}(\boldsymbol{\rho} - \tilde{\mathbf{p}}_e) \quad (5.107)$$

$$\boldsymbol{\nu} = \dot{\tilde{\mathbf{p}}}_e + k_{Pp}\tilde{\mathbf{p}}_e. \quad (5.108)$$

The vector $\boldsymbol{\nu}$ in (5.108) provides an estimate of the end-effector velocity, where the vectors $\boldsymbol{\kappa}$ and $\dot{\tilde{\mathbf{p}}}_e$ are the states of the observer and

$$\tilde{\mathbf{p}}_e = \hat{\mathbf{p}}_e - \mathbf{p}_e \quad (5.109)$$

denotes the observer position estimation error.

Notice that the term $-k_{Pp}\tilde{\mathbf{p}}_e$ in (5.107) has been added in order to allow computation of $\dot{\mathbf{r}}_\nu$ in (5.104) and (5.106) as

$$\dot{\mathbf{r}}_\nu = \ddot{\mathbf{p}}_d + k_{Pp}(\dot{\mathbf{p}}_d - \dot{\tilde{\mathbf{p}}}_e) + k_{Ip}\Delta f \quad (5.110)$$

which depends on end-effector position and contact force only, without requiring velocity measurements. A comparison of the control law (5.104) with the control law (5.56) shows that the end-effector velocity $\dot{\mathbf{p}}_e$ has been replaced with the estimate $\boldsymbol{\nu}$ and accordingly the reference vector \mathbf{r} with \mathbf{r}_ν .

Folding (5.104) in (5.1), and accounting for (5.10) and (5.11), gives

$$\mathbf{B}_p(\mathbf{p}_e)\dot{\mathbf{e}}_\nu + \mathbf{C}_p(\mathbf{p}_e, \dot{\mathbf{p}}_e)\mathbf{e}_\nu + \lambda_1 \mathbf{e}_\nu + \lambda_2 \boldsymbol{\rho} = \lambda_1 \boldsymbol{\varepsilon} - \mathbf{C}_p(\mathbf{p}_e, \mathbf{r}_\nu)\boldsymbol{\varepsilon} \quad (5.111)$$

where

$$\mathbf{e}_\nu = \mathbf{r}_\nu - \dot{\tilde{\mathbf{p}}}_e = \Delta \dot{\mathbf{p}}_{de} + k_{Pp}(\boldsymbol{\rho} - \tilde{\mathbf{p}}_e) \quad (5.112)$$

$$\boldsymbol{\varepsilon} = \boldsymbol{\nu} - \dot{\tilde{\mathbf{p}}}_e = \dot{\tilde{\mathbf{p}}}_e + k_{Pp}\tilde{\mathbf{p}}_e. \quad (5.113)$$

Then, from (5.105) and (5.106) it is

$$\mathbf{B}_p(\mathbf{p}_e)(\dot{\boldsymbol{\varepsilon}} + k_O\boldsymbol{\varepsilon}) + \lambda_2\tilde{\mathbf{p}}_e = \mathbf{B}_p(\mathbf{p}_e)\dot{\mathbf{e}}_\nu + \lambda_2\boldsymbol{\rho}. \quad (5.114)$$

Also, combining (5.114) with (5.111) gives

$$\begin{aligned} \mathbf{B}_p(\mathbf{p}_e)\dot{\boldsymbol{\varepsilon}} + \mathbf{C}_p(\mathbf{p}_e, \mathbf{r}_\nu)\boldsymbol{\varepsilon} + k_O\mathbf{B}_p(\mathbf{p}_e)\boldsymbol{\varepsilon} - \lambda_1\boldsymbol{\varepsilon} + \lambda_2\tilde{\mathbf{p}}_e = \\ -\lambda_1\mathbf{e}_\nu - \mathbf{C}_p(\mathbf{p}_e, \dot{\mathbf{p}}_e)\mathbf{e}_\nu \end{aligned} \quad (5.115)$$

where (5.10) and (5.11) have been exploited again.

Computing the time derivative of \mathbf{e} in (5.19), and using (5.112) and (5.60), gives

$$\dot{\mathbf{e}} = \Delta \dot{\mathbf{p}}_{de} = \mathbf{e}_\nu - k_{Pp}(\boldsymbol{\rho} - \tilde{\mathbf{p}}_e). \quad (5.116)$$

Equations (5.111), (5.115), (5.116), (5.23) and (5.113), with $\boldsymbol{\rho}$ computed as in (5.60), describe the closed-loop system in terms of the (13×1) state vector

$$\mathbf{w}' = [\mathbf{e}_\nu^T \quad \boldsymbol{\epsilon}^T \quad \mathbf{e}^T \quad h \quad \tilde{\mathbf{p}}_e^T]^T \quad (5.117)$$

as

$$\dot{\mathbf{w}}' = \mathbf{V}' \mathbf{w}' \quad (5.118)$$

with

$$\mathbf{V}' = \begin{bmatrix} -\mathbf{B}_p^{-1}(\mathbf{C}_p(\mathbf{p}_e, \dot{\mathbf{p}}_e) + \lambda_1 \mathbf{I}) & -\mathbf{B}_p^{-1}(\mathbf{C}_p(\mathbf{p}_e, \mathbf{r}_\nu) - \lambda_1 \mathbf{I}) \\ -\mathbf{B}_p^{-1}(\mathbf{C}_p(\mathbf{p}_e, \dot{\mathbf{p}}_e) + \lambda_1 \mathbf{I}) & -\mathbf{B}_p^{-1}(\mathbf{C}_p(\mathbf{p}_e, \mathbf{r}_\nu) - \lambda_1 \mathbf{I}) - k_O \mathbf{I} \\ \mathbf{I} & \mathbf{O} \\ \mathbf{0}^T & \mathbf{0}^T \\ \mathbf{O} & \mathbf{I} \\ -\lambda_2 \mathbf{B}_p^{-1} & -\lambda_2 k_{Pp}^{-1} k_{Ip} \mathbf{B}_p^{-1} \mathbf{n}_c & \mathbf{O} \\ \mathbf{O} & \mathbf{0} & -\lambda_2 \mathbf{B}_p^{-1} \\ -k_{Pp} \mathbf{I} & -k_{Ip} \mathbf{n}_c & -k_{Pp} \mathbf{I} \\ k_{f,n} \mathbf{n}_c^T & 0 & \mathbf{0}^T \\ \mathbf{O} & \mathbf{0} & -k_{Pp} \mathbf{I} \end{bmatrix}. \quad (5.119)$$

Notice that the origin of the state space represents the equilibrium of the system (5.118). Stability around this equilibrium can be ascertained as follows.

Consider the Lyapunov function candidate

$$\mathcal{V} = \frac{1}{2} \mathbf{w}'^T \mathbf{X}' \mathbf{w}' \quad (5.120)$$

with

$$\mathbf{X}' = \begin{bmatrix} \mathbf{B}_p & \mathbf{O} & \mathbf{O} & \mathbf{0} & \mathbf{O} \\ \mathbf{O} & \mathbf{B}_p & \mathbf{O} & \mathbf{0} & \mathbf{O} \\ \mathbf{O} & \mathbf{O} & \lambda_2 \mathbf{I} & \lambda_2 k_{Pp}^{-1} k_{Ip} \mathbf{n}_c & \mathbf{O} \\ \mathbf{0}^T & \mathbf{0}^T & \lambda_2 k_{Pp}^{-1} k_{Ip} \mathbf{n}_c^T & \lambda_2 k_{Ip} k_{f,n}^{-1} & \mathbf{0}^T \\ \mathbf{O} & \mathbf{O} & \mathbf{O} & \mathbf{0} & \lambda_2 \mathbf{I} \end{bmatrix}. \quad (5.121)$$

The function \mathcal{V} can be lower-bounded as

$$\begin{aligned} \mathcal{V} &\geq \frac{1}{2} \lambda_2 [\|\mathbf{e}\| \quad |h|] \begin{bmatrix} 1 & -k_{Pp}^{-1} k_{Ip} \\ -k_{Pp}^{-1} k_{Ip} & k_{Ip} k_{f,n}^{-1} \end{bmatrix} \begin{bmatrix} \|\mathbf{e}\| \\ |h| \end{bmatrix} \\ &\quad + \frac{1}{2} B_m \|\mathbf{e}_\nu\|^2 + \frac{1}{2} B_m \|\boldsymbol{\epsilon}\|^2 + \frac{1}{2} \lambda_2 \|\tilde{\mathbf{p}}_e\|^2 \end{aligned} \quad (5.122)$$

where (5.6) has been used. Equation (5.122) reveals that \mathcal{V} is positive definite provided that condition (5.70) holds.

Computing the time derivative of \mathcal{V} along the trajectories of the system (5.118), and accounting for the passivity property of the matrix in (5.8), gives

$$\begin{aligned}\dot{\mathcal{V}} = & -\lambda_1 \mathbf{e}_\nu^T \mathbf{e}_\nu - \lambda_2 k_{Pp} \mathbf{e}^T \mathbf{e} + \lambda_2 k_{Pp}^{-1} k_{Ip} k_{f,n} (\mathbf{n}_c^T \mathbf{e})^2 \\ & - \lambda_2 k_{Pp}^{-1} k_{Ip}^2 h^2 - \lambda_2 k_{Ip} h \mathbf{n}_c^T \mathbf{e} \\ & - k_O \boldsymbol{\varepsilon}^T \mathbf{B}_p \boldsymbol{\varepsilon} + \lambda_1 \boldsymbol{\varepsilon}^T \boldsymbol{\varepsilon} - \mathbf{e}_\nu^T \mathbf{C}_p(\mathbf{p}_e, \boldsymbol{\varepsilon}) \mathbf{r}_\nu \\ & - \boldsymbol{\varepsilon}^T \mathbf{C}(\mathbf{p}_e, \mathbf{e}_\nu)(\boldsymbol{\varepsilon} + \dot{\mathbf{p}}_e) + k_{Pp} \boldsymbol{\rho}^T \tilde{\mathbf{p}}_e - k_{Pp} \tilde{\mathbf{p}}_e^T \tilde{\mathbf{p}}_e,\end{aligned}\quad (5.123)$$

where the equality

$$\mathbf{C}_p(\mathbf{p}_e, \mathbf{r}_\nu) \boldsymbol{\varepsilon} + \mathbf{C}_p(\mathbf{p}_e, \dot{\mathbf{p}}_e) \mathbf{e}_\nu = \mathbf{C}_p(\mathbf{p}_e, \dot{\mathbf{p}}_e) \boldsymbol{\varepsilon} + \mathbf{C}_p(\mathbf{p}_e, \mathbf{e}_\nu)(\boldsymbol{\varepsilon} + \dot{\mathbf{p}}_e) \quad (5.124)$$

has been exploited. In view of (5.6) and (5.12), the function $\dot{\mathcal{V}}$ can be upper-bounded as

$$\begin{aligned}\dot{\mathcal{V}} \leq & -(\lambda_1 - C_M(V_M + k_{Pp}\|\mathbf{e}\| + k_{Ip}|h| + k_{Pp}\|\tilde{\mathbf{p}}_e\| + \|\boldsymbol{\varepsilon}\|))\|\mathbf{e}_\nu\|^2 \\ & -(k_O B_m - \lambda_1 - C_M(V_M + k_{Pp}\|\mathbf{e}\| + k_{Ip}|h| + k_{Pp}\|\tilde{\mathbf{p}}_e\| + \|\mathbf{e}_\nu\|))\|\boldsymbol{\varepsilon}\|^2 \\ & -\lambda_2(k_{Pp} - k_{Pp}^{-1}k_{Ip}k_{f,n})\|\mathbf{e}\|^2 - \lambda_2 k_{Pp}^{-1} k_{Ip}^2 h^2 - \lambda_2 k_{Ip} |h| \|\mathbf{e}\| - k_{Pp} \|\tilde{\mathbf{p}}_e\|^2,\end{aligned}\quad (5.125)$$

where (5.39) has been used, and the upper bound on the desired end-effector velocity

$$\|\dot{\mathbf{p}}_d(t)\| \leq V_M \quad (5.126)$$

has been assumed.

Consider the region of the state space

$$\mathcal{W}' = \{\mathbf{w}' : \|\mathbf{w}'\| < \Theta'\}. \quad (5.127)$$

Equation (5.125) reveals that $\dot{\mathcal{V}}$ is negative definite in \mathcal{W}' provided that (5.70) holds and

$$0 < \Theta' < \min\{\Theta_1, \Theta_2\} \quad (5.128)$$

where

$$\Theta_1 = \frac{\lambda_1 - C_M V_M}{C_M(2k_{Pp} + k_{Ip} + 1)} \quad (5.129)$$

$$\Theta_2 = \frac{k_O B_m - \lambda_1 - C_M V_M}{C_M(2k_{Pp} + k_{Ip} + 1)}. \quad (5.130)$$

Therefore, asymptotic stability of $\mathbf{w}' = \mathbf{0}$ can be concluded, implying *regulation* of the *contact force* to the desired value and *tracking* of the desired *end-effector position*, thanks to the nonlinear observer.

It is worth remarking that, with respect to the previous full-state passivity-based control, λ_1 is used in (5.129) and (5.130), and only λ_2 is free.

The passivity-based output feedback control has been derived in the task space. Since control actions are to be realized by the joint actuators, it is worth carrying out the implementation in the joint space. By using the relationship between the dynamics in the joint space and the dynamics in the task space established by (5.2), (5.3), (5.4) and (5.5), the counterpart of the control law (5.104) in the joint space is given by

$$\boldsymbol{\tau} = \mathbf{B}(\mathbf{q})\boldsymbol{\varrho}_\nu + \mathbf{C}(\mathbf{q}, \mathbf{q}_\nu)\boldsymbol{\varrho} + \mathbf{g}(\mathbf{q}) + \mathbf{J}_p^T(\mathbf{q})(\mathbf{f} + \lambda_1(\mathbf{r}_\nu - \mathbf{\nu}) + \lambda_2\boldsymbol{\rho}) \quad (5.131)$$

where \mathbf{J}_p is the Jacobian in (2.6), and

$$\boldsymbol{\varrho} = \mathbf{J}_p^{-1}(\mathbf{q})\mathbf{r}_\nu \quad (5.132)$$

$$\mathbf{q}_\nu = \mathbf{J}_p^{-1}(\mathbf{q})\mathbf{\nu} \quad (5.133)$$

$$\boldsymbol{\varrho}_\nu = \mathbf{J}_p^{-1}(\mathbf{q})\left(\dot{\mathbf{r}}_\nu - \dot{\mathbf{J}}_p(\mathbf{q}, \mathbf{q}_\nu)\boldsymbol{\varrho}\right). \quad (5.134)$$

As for the observer, its equations can be computed directly by (5.105) and (5.106).

3.3 EXPERIMENTS

The above passivity-based output feedback control scheme has been tested in *experiments* on the six-joint industrial robot described in Section 3. of Chapter 1 endowed with the force/torque sensor; only the inner three joints are used while the outer three joints are mechanically braked.

Case study. The environment and the end effector are those described in Subsection 1.2 of Chapter 3. The task consists of a straight-line motion in the Y_bZ_b -plane with an end-effector (horizontal) displacement of 0.25 m along Y_b and (vertical) displacement of -0.15 m along Z_b . The trajectory along the path is generated according to a trapezoidal velocity profile with cubic blends and null initial and final velocities and accelerations, and a duration of 6 s. The surface of the cardboard box is nearly flat and is placed (horizontally) in the X_bY_b -plane in such a way as to obstruct the desired end-effector motion. To begin, a null set point is assigned to the contact force; when the end effector comes into contact with the environment, the desired force along Z_b is taken to 20 N according to the same kind of interpolating polynomial as for the position, with null initial and final first and second time derivatives, and a duration of 2 s; that value is then kept constant.

The control and observer gains in (5.131), (5.105) and (5.106) have been set to $\lambda_1 = 1700$, $\lambda_2 = 100$, $k_{Pp} = 40$, $k_{Ip} = 0.06$ and $k_O = 100$ in order to guarantee a satisfactory behavior during the constrained motion.

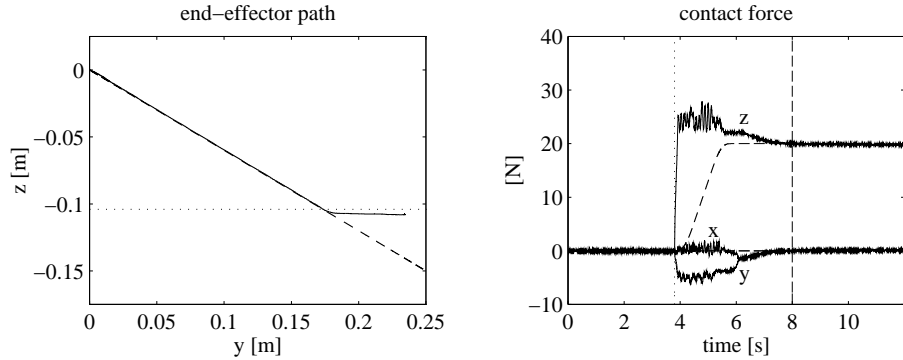


Figure 5.5. Experimental results under passivity-based force and position control with nonlinear observer.

The experimental results are illustrated in Fig. 5.5 in terms of the end-effector path, together with the time history of the desired (dashed) and the actual (solid) contact force. As above, the approximate location (dotted) of the surface is illustrated on the plot of the end-effector path, while the instant of contact (dotted line) is evidenced on the plot of the contact force. It can be recognized that after a transient the contact force reaches the desired value; the transient on the component along Z_b is due to the nonnull value of end-effector velocity at the contact as well as to the imposed motion into the surface, whereas the appreciable deviation from zero of the component along Y_b is mainly due to contact friction. On the other hand, the path is satisfactorily tracked before the contact as well as after the contact along X_b , whereas significant position errors occur after the contact along both Y_b - and Z_b -axes which are caused by the respective forces along those directions. It can be concluded that the use of the nonlinear observer does not compromise the tracking and steady-state performance of the passivity-based control, and thus it represents a valid solution when joint velocities are not available.

4. FURTHER READING

The task space dynamics of a robot manipulator was originally considered in [57] in the context of the operational space approach. A detailed analysis on the bounds of the inertia matrix has recently been presented in [46]. A set of useful relations for the vector of Coriolis and centrifugal forces is given in [102] where gravity adaptation is performed. The property of linearity in the dynamic parameters dates back to [75], and its extension to the task space for passivity-based control has been carried out in [76]. Further material about dynamic model properties used for control purposes can be found in [49].

The adaptive force and position regulation control scheme was introduced in [91]. Passivity-based control of robot manipulators is surveyed in [79, 12] as a useful premise for adaptive control which indeed was originally proposed in [98]. Broader references on passivity-based control of nonlinear systems are [7, 78]. Robustness of passivity-based control with respect to inverse dynamics control was discussed in [3]. The passivity approach has been applied in [92] to design the force regulation and motion control scheme for a robot manipulator in contact with a compliant surface; its adaptive version is developed in [93] together with experimental results. Other adaptive force control schemes can be found in [89, 63, 8, 113].

Design of observers for motion control of robot manipulators was formulated in [10, 77] for the regulation problem and in [11] for the tracking control problem using a passivity approach. Those works are at the basis of the output feedback control schemes; namely, the regulator in [96] and the passivity-based control in [97]. Further material about the stability of the force and position controllers and observers is available in [94]. An output feedback force and position regulator has also been set forth in [62].

Appendix A

Rigid Body Orientation

For the reader's convenience, a few basic concepts regarding different representations for the orientation of a rigid body and their relationship with the body angular velocity are recalled.

1. ROTATION MATRIX

The location of a rigid body in space is typically described in terms of the (3×1) *position vector* \mathbf{p} and the (3×3) *rotation matrix* \mathbf{R} describing the origin and the orientation of a frame attached to the body with respect to a fixed base frame. The matrix \mathbf{R} is orthogonal, i.e.

$$\mathbf{R}^T \mathbf{R} = \mathbf{I} \quad (\text{A.1})$$

where \mathbf{I} is the (3×3) identity matrix. It follows that the transpose of a rotation matrix is equal to its inverse, i.e.

$$\mathbf{R}^T = \mathbf{R}^{-1}. \quad (\text{A.2})$$

The body *linear velocity* is described by the time derivative of the position vector, i.e. $\dot{\mathbf{p}}$, while its *angular velocity* $\boldsymbol{\omega}$ can be defined through the time derivative of the rotation matrix by the relationship

$$\dot{\mathbf{R}} = \mathbf{S}(\boldsymbol{\omega})\mathbf{R}, \quad (\text{A.3})$$

where $\mathbf{S}(\cdot)$ is the operator performing the cross product between two (3×1) vectors. Given $\boldsymbol{\omega} = [\omega_x \ \omega_y \ \omega_z]^T$, $\mathbf{S}(\boldsymbol{\omega})$ takes on the form

$$\mathbf{S}(\boldsymbol{\omega}) = \begin{bmatrix} 0 & -\omega_z & \omega_y \\ \omega_z & 0 & -\omega_x \\ -\omega_y & \omega_x & 0 \end{bmatrix}. \quad (\text{A.4})$$

It is easy to see that \mathbf{S} is a skew-symmetric matrix, i.e.

$$\mathbf{S}^T(\boldsymbol{\omega}) = -\mathbf{S}(\boldsymbol{\omega}); \quad (\text{A.5})$$

also, it can be shown that

$$\mathbf{R}\mathbf{S}(\boldsymbol{\omega})\mathbf{R}^T = \mathbf{S}(\mathbf{R}\boldsymbol{\omega}). \quad (\text{A.6})$$

Consider now two frames, conventionally labeled Σ_1 and Σ_2 . Let \mathbf{R}_1 denote the rotation matrix expressing the orientation of Σ_1 with respect to the base frame, and ${}^1\mathbf{R}_2$ the rotation matrix expressing the orientation of Σ_2 with respect to Σ_1 . Then, the orientation of Σ_2 with respect to the base frame is obtained by composing the successive changes of orientation with respect to the current frame, i.e.

$$\mathbf{R}_2 = \mathbf{R}_1 {}^1\mathbf{R}_2. \quad (\text{A.7})$$

As usual, a superscript denotes the frame to which a quantity (vector or matrix) is referred; the superscript is dropped whenever a quantity is referred to the base frame. From (A.7), the *mutual orientation* between the two frames can be described by the rotation matrix

$${}^1\mathbf{R}_2 = \mathbf{R}_1^T \mathbf{R}_2. \quad (\text{A.8})$$

Differentiating (A.8) with respect to time gives

$$\begin{aligned} {}^1\dot{\mathbf{R}}_2 &= \mathbf{R}_1^T \left(\mathbf{S}^T(\boldsymbol{\omega}_1) + \mathbf{S}(\boldsymbol{\omega}_2) \right) \mathbf{R}_2 \\ &= \mathbf{R}_1^T \mathbf{S}(\boldsymbol{\omega}_2 - \boldsymbol{\omega}_1) \mathbf{R}_1 \mathbf{R}_1^T \mathbf{R}_2 \\ &= \mathbf{S}(\Delta^1 \boldsymbol{\omega}_{21}) {}^1\mathbf{R}_2 \end{aligned} \quad (\text{A.9})$$

where (A.5) and (A.6) have been exploited. The quantity

$$\Delta\boldsymbol{\omega}_{21} = \boldsymbol{\omega}_2 - \boldsymbol{\omega}_1 \quad (\text{A.10})$$

in (A.9) is the angular velocity of Σ_2 relative to Σ_1 ; the operator Δ has been introduced to denote that a vector difference has been taken.

2. EULER ANGLES

Condition (A.1) implies that the nine elements of a rotation matrix are not independent but related by six constraints. A minimal representation of orientation can be obtained by using a set of three angles $\boldsymbol{\varphi} = [\alpha \ \beta \ \gamma]^T$. Consider the rotation matrix expressing the elementary rotation about one of the coordinate axes as a function of a single angle. Then, a generic rotation matrix

can be obtained by composing a suitable sequence of three elementary rotations while guaranteeing that two successive rotations are not made about parallel axes. This implies that 12 sets of angles are allowed out of all 27 possible combinations; each set represents a triplet of *Euler angles*. For instance, the XYZ representation of orientation in terms of Euler angles is described by the rotation matrix

$$\begin{aligned} \mathbf{R}(\varphi) &= \mathbf{R}_x(\alpha)\mathbf{R}_y(\beta)\mathbf{R}_z(\gamma) \\ &= \begin{bmatrix} c_\beta c_\gamma & -c_\beta s_\gamma & s_\beta \\ s_\alpha s_\beta c_\gamma + c_\alpha s_\gamma & -s_\alpha s_\beta s_\gamma + c_\alpha c_\gamma & -s_\alpha c_\beta \\ -c_\alpha s_\beta c_\gamma + s_\alpha s_\gamma & c_\alpha s_\beta s_\gamma + s_\alpha c_\gamma & c_\alpha c_\beta \end{bmatrix} \end{aligned} \quad (\text{A.11})$$

where \mathbf{R}_x , \mathbf{R}_y , \mathbf{R}_z are the matrices of the elementary rotations about the three coordinate axes, and the notations c_ϕ and s_ϕ are the abbreviations for $\cos \phi$ and $\sin \phi$, respectively.

The set of the Euler angles corresponding to a given rotation matrix

$$\mathbf{R} = \begin{bmatrix} R_{11} & R_{12} & R_{13} \\ R_{21} & R_{22} & R_{23} \\ R_{31} & R_{32} & R_{33} \end{bmatrix} \quad (\text{A.12})$$

is

$$\begin{aligned} \alpha &= \text{Atan2}(-R_{23}, R_{33}) \\ \beta &= \text{Atan2}\left(R_{13}, \sqrt{R_{11}^2 + R_{12}^2}\right) \\ \gamma &= \text{Atan2}(-R_{12}, R_{11}) \end{aligned} \quad (\text{A.13})$$

with $\beta \in (-\pi/2, \pi/2)$, whereas the solution is

$$\begin{aligned} \alpha &= \text{Atan2}(R_{23}, -R_{33}) \\ \beta &= \text{Atan2}\left(R_{13}, -\sqrt{R_{11}^2 + R_{12}^2}\right) \\ \gamma &= \text{Atan2}(R_{12}, -R_{11}) \end{aligned} \quad (\text{A.14})$$

with $\beta \in (\pi/2, 3\pi/2)$; the function $\text{Atan2}(y, x)$ computes the arctangent of the ratio y/x but utilizes the sign of each argument to determine which quadrant the resulting angle belongs to.

Solutions (A.13) and (A.14) degenerate when $\beta = \pm\pi/2$; in this case, it is possible to determine only the sum or difference of α and γ , i.e.

$$\alpha \pm \gamma = \text{Atan2}(R_{21}, R_{22}) \quad (\text{A.15})$$

where the plus sign applies for $\beta = +\pi/2$ and the minus sign applies for $\beta = -\pi/2$. These configurations are termed *representation singularities*.

The relationship between the time derivative of the Euler angles $\dot{\varphi}$ and the body *angular velocity* $\boldsymbol{\omega}$ is given by

$$\boldsymbol{\omega} = \mathbf{T}(\varphi)\dot{\varphi}, \quad (\text{A.16})$$

where the transformation matrix \mathbf{T} corresponding to the above XYZ representation is

$$\mathbf{T}(\varphi) = \begin{bmatrix} 1 & 0 & s_\beta \\ 0 & c_\alpha & -s_\alpha c_\beta \\ 0 & s_\alpha & c_\alpha c_\beta \end{bmatrix}. \quad (\text{A.17})$$

It can be recognized that \mathbf{T} becomes singular at the representation singularities $\beta = \pm\pi/2$; notice that, in these configurations, it is not possible to describe an arbitrary angular velocity with a set of Euler angles time derivatives.

Another set of Euler angles which is widely used in robot kinematics is the ZYZ representation, corresponding to the three joint angles of a spherical wrist. The resulting transformation matrix in (A.16) is

$$\mathbf{T}(\varphi) = \begin{bmatrix} 0 & -s_\alpha & c_\alpha s_\beta \\ 0 & c_\alpha & s_\alpha s_\beta \\ 1 & 0 & c_\beta \end{bmatrix} \quad (\text{A.18})$$

which becomes singular at the representation singularities $\beta = 0, \pi$. For the other ten representations of Euler angles, it can easily be found that the second angle of the sequence always generates a pair of representation singularities which are either those of (A.17) or those of (A.18). In other words, no matter what representation is used, a representation singularity occurs whenever the first and last axes of rotation in the sequence lie along the same direction.

With reference to the problem of describing *mutual orientation* between two frames, the use of Euler angles leads to considering the vector difference

$$\Delta\varphi_{21} = \varphi_2 - \varphi_1 \quad (\text{A.19})$$

where φ_1 and φ_2 are the set of Euler angles that can be extracted from \mathbf{R}_1 and \mathbf{R}_2 , respectively.

Alternatively, the mutual rotation matrix ${}^1\mathbf{R}_2$ can be computed first; then, a set of Euler angles φ_{21} can be extracted from ${}^1\mathbf{R}_2$. The angular velocity $\Delta^1\boldsymbol{\omega}_{21}$ in (A.9) is related to the time derivative of φ_{21} as

$$\Delta^1\boldsymbol{\omega}_{21} = \mathbf{T}(\varphi_{21})\dot{\varphi}_{21} \quad (\text{A.20})$$

where (A.16) and (A.3) have been used.

3. ANGLE/AXIS

An alternative representation of orientation can be obtained in terms of a rotation angle ϑ about an axis in space described by the (3×1) unit vector \mathbf{r} . The rotation matrix corresponding to an *angle/axis* representation is

$$\mathbf{R}(\vartheta, \mathbf{r}) = \mathbf{r}\mathbf{r}^T + \cos \vartheta (\mathbf{I} - \mathbf{r}\mathbf{r}^T) + \sin \vartheta \mathbf{S}(\mathbf{r}). \quad (\text{A.21})$$

It is clear that $\mathbf{R}(-\vartheta, -\mathbf{r}) = \mathbf{R}(\vartheta, \mathbf{r})$, i.e. a rotation by $-\vartheta$ about $-\mathbf{r}$ cannot be distinguished from a rotation by ϑ about \mathbf{r} ; hence, the angle/axis representation is not unique.

On the other hand, the angle/axis corresponding to a given rotation matrix (A.12) is

$$\vartheta = \cos^{-1} \left(\frac{R_{11} + R_{22} + R_{33} - 1}{2} \right) \quad (\text{A.22})$$

$$\mathbf{r} = \frac{1}{2 \sin \vartheta} \begin{bmatrix} R_{32} - R_{23} \\ R_{13} - R_{31} \\ R_{21} - R_{12} \end{bmatrix}. \quad (\text{A.23})$$

In the case $\sin \vartheta = 0$, if $R_{11} + R_{22} + R_{33} = 3$, then $\vartheta = 0$; this means that no rotation has occurred and \mathbf{r} is arbitrary (*representation singularity*). Instead, if $R_{11} + R_{22} + R_{33} = -1$, then $\vartheta = \pi$ and the expression of the rotation matrix becomes

$$\mathbf{R}(\pi, \mathbf{r}) = \begin{bmatrix} 2r_x^2 - 1 & 2r_x r_y & 2r_x r_z \\ 2r_x r_y & 2r_y^2 - 1 & 2r_y r_z \\ 2r_x r_z & 2r_y r_z & 2r_z^2 - 1 \end{bmatrix}. \quad (\text{A.24})$$

The three components r_x , r_y and r_z of the unit vector \mathbf{r} can be computed by taking any row or column; for instance, from the first column it is

$$\begin{aligned} r_x &= \pm \sqrt{\frac{R_{11} + 1}{2}} \\ r_y &= \frac{R_{12}}{2r_x} \\ r_z &= \frac{R_{13}}{2r_x}. \end{aligned} \quad (\text{A.25})$$

However, if $r_x \approx 0$, then the computation of r_y and r_z is ill-conditioned. In that case, it is better to use another column to compute either r_y or r_z , and so forth.

The relationship between the time derivative of the angle/axis parameters and the body *angular velocity* is given by:

$$\dot{\vartheta} = \mathbf{r}^T \boldsymbol{\omega} \quad (\text{A.26})$$

$$\dot{\mathbf{r}} = \frac{1}{2} \left((\mathbf{I} - \mathbf{r}\mathbf{r}^T) \cot \frac{\vartheta}{2} - \mathbf{S}(\mathbf{r}) \right) \boldsymbol{\omega}. \quad (\text{A.27})$$

Notice that Equations (A.26) and (A.27) become ill-defined at the representation singularity ($\vartheta = 0$).

4. QUATERNION

The drawbacks of the angle/axis representation can be overcome by a four-parameter representation; namely, the unit *quaternion*, viz. Euler parameters, defined as:

$$\mathcal{Q} = \{\eta, \boldsymbol{\epsilon}\} \quad (\text{A.28})$$

where

$$\eta = \cos \frac{\vartheta}{2} \quad (\text{A.29})$$

$$\boldsymbol{\epsilon} = \sin \frac{\vartheta}{2} \mathbf{r}, \quad (\text{A.30})$$

with $\eta \geq 0$ for $\vartheta \in [-\pi, \pi]$; η is called the scalar part of the quaternion while $\boldsymbol{\epsilon}$ is called the vector part of the quaternion. They are constrained by

$$\eta^2 + \boldsymbol{\epsilon}^T \boldsymbol{\epsilon} = 1, \quad (\text{A.31})$$

hence the name *unit* quaternion. It is worth remarking that, differently from the angle/axis representation, a rotation by $-\vartheta$ about $-\mathbf{r}$ gives the same quaternion as that associated with a rotation by ϑ about \mathbf{r} ; this solves the above nonuniqueness problem. Also, no singularity occurs.

The quaternion extracted from \mathbf{R}^{-1} is denoted as \mathcal{Q}^{-1} and can be computed as

$$\mathcal{Q}^{-1} = \{\eta, -\boldsymbol{\epsilon}\}. \quad (\text{A.32})$$

The rotation matrix corresponding to a given quaternion is

$$\mathbf{R}(\eta, \boldsymbol{\epsilon}) = (\eta^2 - \boldsymbol{\epsilon}^T \boldsymbol{\epsilon}) \mathbf{I} + 2\boldsymbol{\epsilon}\boldsymbol{\epsilon}^T + 2\eta\mathbf{S}(\boldsymbol{\epsilon}). \quad (\text{A.33})$$

On the other hand, the quaternion corresponding to a given rotation matrix (A.12) is

$$\eta = \frac{1}{2} \sqrt{R_{11} + R_{22} + R_{33} + 1} \quad (\text{A.34})$$

$$\boldsymbol{\epsilon} = \frac{1}{2} \begin{bmatrix} \text{sgn}(R_{32} - R_{23}) \sqrt{R_{11} - R_{22} - R_{33} + 1} \\ \text{sgn}(R_{13} - R_{31}) \sqrt{R_{22} - R_{33} - R_{11} + 1} \\ \text{sgn}(R_{21} - R_{12}) \sqrt{R_{33} - R_{11} - R_{22} + 1} \end{bmatrix}. \quad (\text{A.35})$$

The relationship between the time derivative of the Euler parameters and the body *angular velocity* $\boldsymbol{\omega}$ is established by the so-called propagation rule:

$$\dot{\eta} = -\frac{1}{2}\boldsymbol{\epsilon}^T \boldsymbol{\omega} \quad (A.36)$$

$$\dot{\boldsymbol{\epsilon}} = \frac{1}{2}\mathbf{E}(\eta, \boldsymbol{\epsilon})\boldsymbol{\omega} \quad (A.37)$$

with

$$\mathbf{E}(\eta, \boldsymbol{\epsilon}) = \eta \mathbf{I} - \mathbf{S}(\boldsymbol{\epsilon}). \quad (A.38)$$

With reference to the problem of describing *mutual orientation* between two frames, the quantity

$$\mathcal{Q}_{21} = \{\eta_{21}, {}^1\boldsymbol{\epsilon}_{21}\} \quad (A.39)$$

denotes the quaternion that can be extracted directly from ${}^1\mathbf{R}_2$. Notice that the vector part of the quaternion is the same when referred to Σ_2 , i.e. ${}^1\boldsymbol{\epsilon}_{21} = {}^2\boldsymbol{\epsilon}_{21}$.

The composition rule in terms of quaternions corresponding to (A.7) is defined by the operator “*” as

$$\mathcal{Q}_2 = \mathcal{Q}_1 * \mathcal{Q}_{21} \quad (A.40)$$

with

$$\eta_2 = \eta_1 \eta_{21} - \boldsymbol{\epsilon}_1^T \boldsymbol{\epsilon}_{21} \quad (A.41)$$

$$\boldsymbol{\epsilon}_2 = \eta_1 {}^1\boldsymbol{\epsilon}_{21} + \eta_{21} \boldsymbol{\epsilon}_1 + \mathbf{S}(\boldsymbol{\epsilon}_1) {}^1\boldsymbol{\epsilon}_{21}. \quad (A.42)$$

Note that in (A.40) \mathcal{Q}_1 and \mathcal{Q}_2 are the quaternions that can be extracted from \mathbf{R}_1 and \mathbf{R}_2 , respectively, with \mathcal{Q}_{21} as in (A.39).

In view of (A.32) and (A.40), the quaternion expressing the mutual orientation between two frames can also be computed by the composition

$$\mathcal{Q}_{21} = \mathcal{Q}_1^{-1} * \mathcal{Q}_2 \quad (A.43)$$

with

$$\eta_{21} = \eta_1 \eta_2 + \boldsymbol{\epsilon}_1^T \boldsymbol{\epsilon}_2 \quad (A.44)$$

$${}^1\boldsymbol{\epsilon}_{21} = \eta_1 \boldsymbol{\epsilon}_2 - \eta_2 \boldsymbol{\epsilon}_1 - \mathbf{S}(\boldsymbol{\epsilon}_1) \boldsymbol{\epsilon}_2. \quad (A.45)$$

The propagation rule (A.36) and (A.37) for the quaternion in (A.39) can be written as

$$\dot{\eta}_{21} = -\frac{1}{2} {}^1\boldsymbol{\epsilon}_{21}^T \Delta {}^1\boldsymbol{\omega}_{21} \quad (A.46)$$

$${}^1\dot{\boldsymbol{\epsilon}}_{21} = \frac{1}{2}\mathbf{E}(\eta_{21}, {}^1\boldsymbol{\epsilon}_{21})\Delta {}^1\boldsymbol{\omega}_{21} \quad (A.47)$$

with \mathbf{E} defined as in (A.38).

Appendix B

Models of Robot Manipulators

The kinematic models and dynamic models for the two robot manipulators used in the experiments are presented.

1. KINEMATIC MODELS

Two industrial robots Comau SMART-3S are available in the PRISMA Lab. Each robot manipulator has an open kinematic chain with six revolute joints, creating an anthropomorphic geometry with nonnull shoulder and elbow offsets and non-spherical wrist. One manipulator is mounted on a sliding track (prismatic joint) which provides an additional degree of mobility. The geometry of the seven-joint manipulator is depicted in Fig. B.1 where the joint variables are numbered from q_0 to q_6 . Then, the joint variables for the six-joint manipulator are numbered from q_1 to q_6 . Further, the link lengths are denoted from l_0 to l_7 and their numerical values, listed in Table B.1, are taken from the data sheet of the robot manufacturer.

Table B.1. Link lengths for the two robot manipulators.

Link	l_i
0	0.850
1	0.150
2	0.610
3	0.110
4	0.610
5	0.113
6	0.103

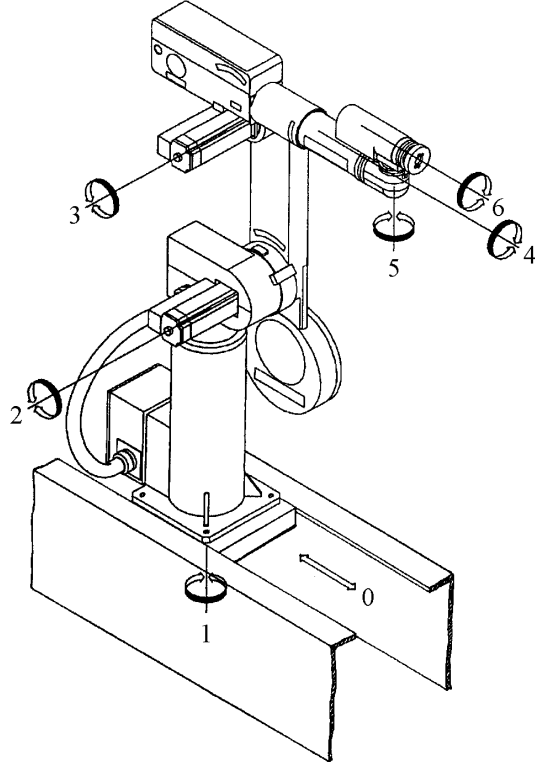


Figure B.1. Geometry of seven-joint manipulator.

1.1 SIX-JOINT MANIPULATOR

The *kinematic model* has been derived using the Denavit and Hartenberg convention. The computation has been cast in a recursive fashion in terms of the position and orientation of the intermediate frames attached to the six links in the chain. Let

$$\mathbf{p}_i = \begin{bmatrix} p_{i,1} \\ p_{i,2} \\ p_{i,3} \end{bmatrix} \quad (\text{B.1})$$

denote the position vector of the origin of the frame attached to link i , and

$$\mathbf{R}_i = \begin{bmatrix} R_{i,11} & R_{i,12} & R_{i,13} \\ R_{i,21} & R_{i,22} & R_{i,23} \\ R_{i,31} & R_{i,32} & R_{i,33} \end{bmatrix} \quad (\text{B.2})$$

denote the rotation matrix expressing the orientation of that frame. These quantities run for $i = 1, \dots, 6$ and are assumed to be referred to the base frame. This is chosen with the Z_b -axis aligned with the axis of joint 1 and the

origin at the intersection of the common normal between the axes of joints 1 and 2 with the axis of joint 1.

The sequence is as follows. For link 1:

$$\begin{aligned}
 R_{1,11} &= c_1 \\
 R_{1,12} &= 0 \\
 R_{1,13} &= -s_1 \\
 R_{1,21} &= s_1 \\
 R_{1,22} &= 0 \\
 R_{1,23} &= c_1 \\
 R_{1,31} &= 0 \\
 R_{1,32} &= -1 \\
 R_{1,33} &= 0
 \end{aligned} \tag{B.3}$$

and

$$\begin{aligned}
 p_{1,1} &= l_1 R_{1,11} \\
 p_{1,2} &= l_1 R_{1,21} \\
 p_{1,3} &= 0.
 \end{aligned} \tag{B.4}$$

For link 2:

$$\begin{aligned}
 R_{2,11} &= c_2 R_{1,11} \\
 R_{2,12} &= -s_2 R_{1,11} \\
 R_{2,13} &= -R_{1,13} \\
 R_{2,21} &= c_2 R_{1,21} \\
 R_{2,22} &= -s_2 R_{1,21} \\
 R_{2,23} &= R_{1,23} \\
 R_{2,31} &= s_2 R_{1,32} \\
 R_{2,32} &= c_2 R_{1,32} \\
 R_{2,33} &= 0
 \end{aligned} \tag{B.5}$$

and

$$\begin{aligned}
 p_{2,1} &= l_2 R_{2,11} + p_{1,1} \\
 p_{2,2} &= l_2 R_{2,21} + p_{1,2} \\
 p_{2,3} &= -l_2 R_{2,31} + p_{1,3}.
 \end{aligned} \tag{B.6}$$

For link 3:

$$R_{3,11} = c_3 R_{2,11} + s_3 R_{2,12}$$

$$\begin{aligned}
R_{3,12} &= -R_{2,13} \\
R_{3,13} &= c_3 R_{2,12} - s_3 R_{2,11} \\
R_{3,21} &= c_3 R_{2,21} + s_3 R_{2,22} \\
R_{3,22} &= -R_{2,23} \\
R_{3,23} &= c_3 R_{2,22} - s_3 R_{2,21} \\
R_{3,31} &= c_3 R_{2,31} + s_3 R_{2,32} \\
R_{3,32} &= 0 \\
R_{3,33} &= c_3 R_{2,32} - s_3 R_{2,31}
\end{aligned} \tag{B.7}$$

and

$$\begin{aligned}
p_{3,1} &= l_3 R_{3,11} + p_{2,1} \\
p_{3,2} &= l_3 R_{3,21} + p_{2,2} \\
p_{3,3} &= l_3 R_{3,31} + p_{2,3}.
\end{aligned} \tag{B.8}$$

For link 4:

$$\begin{aligned}
R_{4,11} &= c_4 R_{3,11} + s_4 R_{3,12} \\
R_{4,12} &= R_{3,13} \\
R_{4,13} &= s_4 R_{3,11} - c_4 R_{3,12} \\
R_{4,21} &= c_4 R_{3,21} + s_4 R_{3,22} \\
R_{4,22} &= R_{3,23} \\
R_{4,23} &= s_4 R_{3,21} - c_4 R_{3,22} \\
R_{4,31} &= c_4 R_{3,31} \\
R_{4,32} &= R_{3,33} \\
R_{4,33} &= s_4 R_{3,31}
\end{aligned} \tag{B.9}$$

and

$$\begin{aligned}
p_{4,1} &= l_4 R_{3,13} + p_{3,1} \\
p_{4,2} &= l_4 R_{3,23} + p_{3,2} \\
p_{4,3} &= l_4 R_{3,33} + p_{3,3}.
\end{aligned} \tag{B.10}$$

For link 5:

$$\begin{aligned}
R_{5,11} &= c_5 R_{4,11} + s_5 R_{4,12} \\
R_{5,12} &= -R_{4,13} \\
R_{5,13} &= c_5 R_{4,12} - s_5 R_{4,11} \\
R_{5,21} &= c_5 R_{4,21} + s_5 R_{4,22}
\end{aligned}$$

$$\begin{aligned}
 R_{5,22} &= -R_{4,23} & (B.11) \\
 R_{5,23} &= c_5 R_{4,22} - s_5 R_{4,21} \\
 R_{5,31} &= c_5 R_{4,31} + s_5 R_{4,32} \\
 R_{5,32} &= -R_{4,33} \\
 R_{5,33} &= c_5 R_{4,32} - s_5 R_{4,31}
 \end{aligned}$$

and

$$\begin{aligned}
 p_{5,1} &= -l_5 R_{4,13} + p_{4,1} \\
 p_{5,2} &= -l_5 R_{4,23} + p_{4,2} & (B.12) \\
 p_{5,3} &= -l_5 R_{4,33} + p_{4,3}.
 \end{aligned}$$

For link 6:

$$\begin{aligned}
 R_{6,11} &= c_6 R_{5,11} + s_6 R_{5,12} \\
 R_{6,12} &= c_6 R_{5,12} - s_6 R_{5,11} \\
 R_{6,13} &= R_{5,13} \\
 R_{6,21} &= c_6 R_{5,21} + s_6 R_{5,22} \\
 R_{6,22} &= c_6 R_{5,22} - s_6 R_{5,21} & (B.13) \\
 R_{6,23} &= R_{5,23} \\
 R_{6,31} &= c_6 R_{5,31} + s_6 R_{5,32} \\
 R_{6,32} &= c_6 R_{5,32} - s_6 R_{5,31} \\
 R_{6,33} &= R_{5,33}
 \end{aligned}$$

and

$$\begin{aligned}
 p_{6,1} &= l_6 R_{5,13} + p_{5,1} \\
 p_{6,2} &= l_6 R_{5,23} + p_{5,2} & (B.14) \\
 p_{6,3} &= l_6 R_{5,33} + p_{5,3},
 \end{aligned}$$

where $\mathbf{p}_6 = \mathbf{p}_e$ and $\mathbf{R}_6 = \mathbf{R}_e$ represent the position and the orientation of the end effector as in (2.2) and (2.3).

With reference to (2.6), the *Jacobian* \mathbf{J}_p is the (3×6) matrix given by:

$$\begin{aligned}
 J_{p,11} &= -p_{e2} \\
 J_{p,12} &= R_{1,23} r_{e1,3} - R_{1,33} r_{e1,2} \\
 J_{p,13} &= R_{2,23} r_{e2,3} - R_{2,33} r_{e2,2} \\
 J_{p,14} &= R_{3,23} r_{e3,3} - R_{3,33} r_{e3,2} \\
 J_{p,15} &= R_{4,23} r_{e4,3} - R_{4,33} r_{e4,2} \\
 J_{p,16} &= R_{5,23} r_{e5,3} - R_{5,33} r_{e5,2}
 \end{aligned}$$

$$\begin{aligned}
J_{p,21} &= p_{e1} \\
J_{p,22} &= R_{1,33}r_{e1,1} - R_{1,13}r_{e1,3} \\
J_{p,23} &= R_{2,33}r_{e2,1} - R_{2,13}r_{e2,3} \\
J_{p,24} &= R_{3,33}r_{e3,1} - R_{3,13}r_{e3,3} \\
J_{p,25} &= R_{4,33}r_{e4,1} - R_{4,13}r_{e4,3} \\
J_{p,26} &= R_{5,33}r_{e5,1} - R_{5,13}r_{e5,3} \\
J_{p,31} &= 0 \\
J_{p,32} &= R_{1,13}r_{e1,2} - R_{1,23}r_{e1,1} \\
J_{p,33} &= R_{2,13}r_{e2,2} - R_{2,23}r_{e2,1} \\
J_{p,34} &= R_{3,13}r_{e3,2} - R_{3,23}r_{e3,1} \\
J_{p,35} &= R_{4,13}r_{e4,2} - R_{4,23}r_{e4,1} \\
J_{p,36} &= R_{5,13}r_{e5,2} - R_{5,23}r_{e5,1}
\end{aligned} \tag{B.15}$$

where

$$\mathbf{r}_{ei} = \mathbf{p}_e - \mathbf{p}_i \tag{B.16}$$

for $i = 1, \dots, 5$. The Jacobian \mathbf{J}_o is the (3×6) matrix given by

$$\begin{aligned}
J_{o,11} &= 0 \\
J_{o,12} &= R_{1,13} \\
J_{o,13} &= R_{2,13} \\
J_{o,14} &= R_{3,13} \\
J_{o,15} &= R_{4,13} \\
J_{o,16} &= R_{5,13} \\
J_{o,21} &= 0 \\
J_{o,22} &= R_{1,23} \\
J_{o,23} &= R_{2,23} \\
J_{o,24} &= R_{3,23} \\
J_{o,25} &= R_{4,23} \\
J_{o,26} &= R_{5,23} \\
J_{o,31} &= 1 \\
J_{o,32} &= R_{1,33} \\
J_{o,33} &= R_{2,33} \\
J_{o,34} &= R_{3,33} \\
J_{o,35} &= R_{4,33} \\
J_{o,36} &= R_{5,33}.
\end{aligned} \tag{B.17}$$

1.2 SEVEN-JOINT MANIPULATOR

The *kinematic model* has been derived from that of the six-joint manipulator as follows.

The base frame is chosen with the Z_b -axis aligned with the axis of joint 0, the Y_b -axis aligned with the axis of joint 1, and the origin at the mechanical limit for the range of the prismatic joint. The orientation and position of the frame attached to link 0 are given by:

$$\begin{aligned} R_{0,11} &= 1 \\ R_{0,12} &= 0 \\ R_{0,13} &= 0 \\ R_{0,21} &= 0 \\ R_{0,22} &= 0 \\ R_{0,23} &= 1 \\ R_{0,31} &= 0 \\ R_{0,32} &= -1 \\ R_{0,33} &= 0 \end{aligned} \quad (B.18)$$

and

$$\begin{aligned} p_{0,1} &= 0 \\ p_{0,2} &= 0 \\ p_{0,3} &= q_0. \end{aligned} \quad (B.19)$$

The orientation and position of the frame attached to link 1 are given by:

$$\begin{aligned} R_{1,11} &= c_1 R_{0,11} \\ R_{1,12} &= 0 \\ R_{1,13} &= -s_1 R_{0,11} \\ R_{1,21} &= 0 \\ R_{1,22} &= -R_{0,23} \\ R_{1,23} &= 0 \\ R_{1,31} &= s_1 R_{0,32} \\ R_{1,32} &= 0 \\ R_{1,33} &= c_1 R_{0,32} \end{aligned} \quad (B.20)$$

and

$$\begin{aligned} p_{1,1} &= l_1 c_1 R_{0,11} + p_{0,1} \\ p_{1,2} &= l_0 R_{0,23} + p_{0,2} \\ p_{1,3} &= l_1 s_1 R_{0,32} + p_{0,3}. \end{aligned} \quad (B.21)$$

Then the sequence for the remaining frames proceeds from (B.5) and (B.6) to (B.13) and (B.14) giving the position and orientation of the end effector.

With reference to (B.15), the additional elements needed for the computation of the (3×7) Jacobian matrix \mathbf{J}_p are:

$$\begin{aligned} J_{p,10} &= R_{0,13} \\ J_{p,20} &= R_{0,23} \\ J_{p,30} &= R_{0,33}. \end{aligned} \quad (\text{B.22})$$

All the remaining elements are the same except $J_{p,11}$, $J_{p,21}$ and $J_{p,31}$ that are to be replaced with:

$$\begin{aligned} J_{p,11} &= R_{0,23}r_{e0,3} - R_{0,33}r_{e0,2} \\ J_{p,21} &= R_{0,33}r_{e0,1} - R_{0,13}r_{e0,3} \\ J_{p,31} &= R_{0,13}r_{e0,2} - R_{0,23}r_{e0,1} \end{aligned} \quad (\text{B.23})$$

where

$$\mathbf{r}_{e0} = \mathbf{p}_e - \mathbf{p}_0. \quad (\text{B.24})$$

With reference to (B.17), the additional elements needed for the computation of the (3×7) Jacobian matrix \mathbf{J}_o are:

$$\begin{aligned} J_{o,10} &= 0 \\ J_{o,20} &= 0 \\ J_{o,30} &= 0. \end{aligned} \quad (\text{B.25})$$

All the remaining elements are the same except $J_{o,11}$, $J_{o,21}$ and $J_{o,31}$ that are to be replaced with:

$$\begin{aligned} J_{o,11} &= R_{0,13} \\ J_{o,21} &= R_{0,23} \\ J_{o,31} &= R_{0,33}. \end{aligned} \quad (\text{B.26})$$

2. DYNAMIC MODELS

Since the dynamic parameters are typically not available from the robot manufacturer, the dynamic models of the two robot manipulators have been identified in terms of a minimum number of parameters. To this purpose, the dynamics of the outer three joints has been simply chosen as purely inertial and decoupled. Only joint viscous friction has been included, since other types of friction (e.g. Coulomb and dry friction) are difficult to model. With reference to (2.21), the dynamic parameters are listed in Table B.2.

Table B.2. Identified dynamic parameters for the two robot manipulators.

π_i	<i>Six-joint</i>	<i>Seven-joint</i>
1	78.7384	762.5649
2	-46.8840	114.8766
3	2.2870	45.7747
4	53.5654	-10.0998
5	-14.2332	-69.9282
6	-9.4194	83.5433
7	3.4727	-10.1028
8	-8.5887	994.8749
9	1.2018	119.3700
10	-0.0989	-4.6261
11	104.4293	-9.7233
12	0.2424	-1.2431
13	0.4411	-4.0507
14	0.9313	-1.1146
15	11.5712	133.0195
16	-5.2824	6.4472
17	3.4585	2.7719
18	3.3329	0.8022
19	35.4644	13.8884
20	0.6165	-21.1525
21	2.4082	-7.2273
22	0.6808	4.7310
23	11.7816	-20.8157
24	0.2077	2.2258
25	3.0460	63.4472
26		0.6165
27		2.4082
28		0.6808
29		11.7816
30		0.2077
31		3.0460

2.1 SIX-JOINT MANIPULATOR

The elements of the symmetric inertia matrix are given by:

$$\begin{aligned}
 B_{11} &= \pi_1 + s_2^2 \pi_2 + 2l_1 c_2 \pi_5 + s_{23}^2 \pi_6 + 2s_2^2 \pi_8 - 2l_1 s_2 \pi_{10} \\
 &\quad + 2s_{23} c_{23} \pi_{12} + 2c_{23} (l_2 c_2 + l_1) \pi_{16} - 2s_{23} (l_2 c_2 + l_1) \pi_{17} \\
 B_{12} &= -s_2 \pi_3 - c_2 \pi_9 - s_{23} \pi_{13} - c_{23} \pi_{14} \\
 B_{13} &= -s_{23} \pi_{13} - c_{23} \pi_{14} \\
 B_{14} &= 0 \\
 B_{15} &= 0
 \end{aligned}$$

$$\begin{aligned}
B_{16} &= 0 \\
B_{22} &= \pi_4 + \pi_{15} + 2c_3l_2\pi_{16} - 2s_3l_2\pi_{17} \\
B_{23} &= \pi_{15} + c_3l_2\pi_{16} - s_3l_2\pi_{17} + (1/k_{r3})\pi_{18} \\
B_{24} &= 0 \\
B_{25} &= 0 \\
B_{26} &= 0 \\
B_{33} &= \pi_{15} + \pi_{18} \\
B_{34} &= 0 \\
B_{35} &= 0 \\
B_{36} &= 0 \\
B_{44} &= \pi_{20} \\
B_{45} &= 0 \\
B_{46} &= 0 \\
B_{55} &= \pi_{22} \\
B_{56} &= 0 \\
B_{66} &= \pi_{24}
\end{aligned} \tag{B.27}$$

where the notations $c_{i\dots j}$ and $s_{i\dots j}$ are the abbreviations for $\cos(q_i + \dots + q_j)$ and $\sin(q_i + \dots + q_j)$, respectively.

The elements of the matrix C in the Coriolis and centrifugal torques are given by:

$$\begin{aligned}
C_{11} &= \dot{q}_2s_2c_2\pi_2 - \dot{q}_2s_2l_1\pi_5 + (\dot{q}_2 + \dot{q}_3)s_{23}c_{23}\pi_6 + \dot{q}_2(c_2^2 - s_2^2)\pi_8 \\
&\quad - \dot{q}_2l_1c_2\pi_{10} + (\dot{q}_2 + \dot{q}_3)(c_{23}^2 - s_{23}^2)\pi_{12} \\
&\quad - (\dot{q}_2l_2s_2c_{23} + (\dot{q}_2 + \dot{q}_3)(l_1 + l_2c_2)s_{23})\pi_{16} \\
&\quad - ((\dot{q}_2 + \dot{q}_3)(l_2c_2 + l_1)c_{23} - \dot{q}_2l_2s_2s_{23})\pi_{17} \\
C_{31} &= -\dot{q}_1s_{23}c_{23}\pi_6 - \dot{q}_1(c_{23}^2 - s_{23}^2)\pi_{12} + \dot{q}_1(l_2c_2 + l_1)s_{23}\pi_{16} \\
&\quad + \dot{q}_1(l_2c_2 + l_1)c_{23}\pi_{17} \\
C_{21} &= C_{31} - \dot{q}_1s_2c_2\pi_2 + \dot{q}_1l_1s_2\pi_5 - \dot{q}_1(c_2^2 - s_2^2)\pi_8 + \dot{q}_1l_1c_2\pi_{10} \\
&\quad + \dot{q}_1l_2s_2c_{23}\pi_{16} - \dot{q}_1l_2s_2s_{23}\pi_{17} \\
C_{13} &= -C_{31} - (\dot{q}_2 + \dot{q}_3)c_{23}\pi_{13} + (\dot{q}_2 + \dot{q}_3)s_{23}\pi_{14} \\
C_{12} &= -C_{21} + C_{13} + C_{31} - \dot{q}_2\pi_3c_2 + \dot{q}_2s_2\pi_9 \\
C_{22} &= -\dot{q}_3l_2s_3\pi_{16} - \dot{q}_3l_2c_3\pi_{17} \\
C_{32} &= \dot{q}_2l_2s_3\pi_{16} + \dot{q}_2l_2c_3\pi_{17} \\
C_{23} &= C_{22} - C_{32} \\
C_{33} &= 0
\end{aligned} \tag{B.28}$$

while $C_{ij} = 0$ for $i, j = 4, 5, 6$.

The diagonal matrix of viscous friction coefficients is given by:

$$\begin{aligned} F_{11} &= \pi_7 \\ F_{22} &= \pi_{11} \\ F_{33} &= \pi_{19} \\ F_{44} &= \pi_{21} \\ F_{55} &= \pi_{23} \\ F_{66} &= \pi_{25}. \end{aligned} \quad (\text{B.29})$$

The vector of gravity torques is given by:

$$\begin{aligned} g_1 &= 0 \\ g_3 &= g(c_{23}\pi_{16} - s_{23}\pi_{17}) \\ g_2 &= g_3 + g(c_2\pi_5 - s_2\pi_{10}) \end{aligned} \quad (\text{B.30})$$

while $g_i = 0$ for $i = 4, 5, 6$, being g the gravity acceleration.

2.2 SEVEN-JOINT MANIPULATOR

The elements of the symmetric inertia matrix are given by:

$$\begin{aligned} B_{00} &= \pi_1 + (c_1^2 + s_1^2(c_2 + 0.5(c_{22} - 1)))\pi_{20} \\ B_{01} &= -c_1\pi_3 + s_1\pi_4 - c_1c_2\pi_{13} + c_1s_2\pi_{14} - c_1(l_1 + c_2l_2)\pi_{20} \\ &\quad - c_1c_{23}\pi_{21} + c_1s_{23}\pi_{22} + s_1\pi_{23} \\ B_{02} &= s_1s_2\pi_{13} + s_1c_2\pi_{14} + s_1s_2l_2\pi_{20} + s_1s_{23}\pi_{21} + s_1c_{23}\pi_{22} \\ B_{03} &= s_1s_{23}\pi_{21} + s_1c_{23}\pi_{22} \\ B_{04} &= 0 \\ B_{05} &= 0 \\ B_{06} &= 0 \\ B_{11} &= \pi_2 + (l_1^2 + 0.5l_2^2(1 + c_{22}) + 2l_1l_2c_2)\pi_{20} + 0.5(1 - c_{22})\pi_5 \\ &\quad + 0.5(1 - c_{2233})\pi_7 + s_{22}\pi_{10} + 2l_1c_2\pi_{13} - 2l_1s_2\pi_{14} + s_{2233}\pi_{16} \\ &\quad + (l_2c_3 + 2l_1c_{23} + l_2c_{223})\pi_{21} - (l_2s_3 + 2l_1s_{23} + l_2s_{223})\pi_{22} \\ B_{12} &= -s_2\pi_{11} - c_2\pi_{12} - s_{23}\pi_{17} - c_{23}\pi_{18} + s_2l_2\pi_{23} \\ B_{13} &= -s_{23}\pi_{17} - c_{23}\pi_{18} \\ B_{14} &= 0 \\ B_{15} &= 0 \\ B_{16} &= 0 \\ B_{22} &= \pi_6 + \pi_{19} + l_2^2\pi_{20} + 2c_3l_2\pi_{21} - 2l_2s_3\pi_{22} \end{aligned} \quad (\text{B.31})$$

$$\begin{aligned}
B_{23} &= \pi_{19} + c_3 l_2 \pi_{21} - s_3 l_2 \pi_{22} + (1/k_{r3}) \pi_{24} \\
B_{24} &= 0 \\
B_{25} &= 0 \\
B_{26} &= 0 \\
B_{33} &= \pi_{19} + \pi_{24} \\
B_{34} &= 0 \\
B_{35} &= 0 \\
B_{36} &= 0 \\
B_{44} &= \pi_{26} \\
B_{45} &= 0 \\
B_{55} &= \pi_{28} \\
B_{56} &= 0 \\
B_{66} &= \pi_{30}.
\end{aligned}$$

The elements of the vector $\mathbf{c} = \mathbf{C}\dot{\mathbf{q}}$ of the Coriolis and centrifugal torques are given by:

$$\begin{aligned}
c_0 &= \dot{q}_1^2 s_1 \pi_3 + \dot{q}_1^2 c_1 \pi_4 + ((\dot{q}_1^2 + \dot{q}_2^2) s_1 c_2 + 2\dot{q}_1 \dot{q}_2 c_1 s_2) \pi_{13} \\
&\quad - ((\dot{q}_1^2 + \dot{q}_2^2) s_1 s_2 - 2\dot{q}_1 \dot{q}_2 c_1 c_2) \pi_{14} \\
&\quad + ((\dot{q}_1^2 + \dot{q}_2^2) s_1 c_2 l_2 + \dot{q}_1 (2\dot{q}_2 c_1 s_2 l_2 + \dot{q}_1 s_1 l_1)) \pi_{20} \\
&\quad + (((\dot{q}_2 + \dot{q}_3)^2 + \dot{q}_1^2) s_1 c_{23} + 2\dot{q}_1 (\dot{q}_2 + \dot{q}_3) c_1 s_{23}) \pi_{21} \\
&\quad + (2\dot{q}_1 (\dot{q}_2 + \dot{q}_3) c_1 c_{23} - (\dot{q}_1^2 + (\dot{q}_2 + \dot{q}_3)^2) s_1 s_{23}) \pi_{22} + \dot{q}_1^2 c_1 \pi_{23} \\
c_1 &= \dot{q}_1 \dot{q}_2 s_{22} \pi_5 + \dot{q}_1 (\dot{q}_2 + \dot{q}_3) s_{2233} \pi_7 + 2\dot{q}_1 \dot{q}_2 c_{22} \pi_{10} - \dot{q}_2^2 c_2 \pi_{11} \\
&\quad + \dot{q}_2^2 s_2 \pi_{12} - 2\dot{q}_1 \dot{q}_2 s_2 l_1 \pi_{13} - 2\dot{q}_1 \dot{q}_2 l_1 c_2 \pi_{14} + 2\dot{q}_1 (\dot{q}_2 + \dot{q}_3) c_{2233} \pi_{16} \\
&\quad - (\dot{q}_2 + \dot{q}_3)^2 c_{23} \pi_{17} + (\dot{q}_2 + \dot{q}_3)^2 s_{23} \pi_{18} - \dot{q}_1 \dot{q}_2 (2s_2 l_1 + s_{22} l_2) l_2 \pi_{20} \\
&\quad - \dot{q}_1 (\dot{q}_3 s_3 l_2 + 2(\dot{q}_2 + \dot{q}_3) s_{23} l_1 + (2\dot{q}_2 + \dot{q}_3) s_{223} l_2) \pi_{21} \\
&\quad - \dot{q}_1 (\dot{q}_3 c_3 l_2 + 2(\dot{q}_2 + \dot{q}_3) (l_1 c_{23} + l_2 c_{223})) \pi_{22} + \dot{q}_2^2 c_2 l_2 \pi_{23} \\
c_2 &= -0.5 \dot{q}_1^2 s_{22} \pi_5 - 0.5 \dot{q}_1^2 s_{2233} \pi_7 - \dot{q}_1^2 c_{22} \pi_{10} + \dot{q}_1^2 s_2 l_1 \pi_{13} \\
&\quad + \dot{q}_1^2 c_2 l_1 \pi_{14} - \dot{q}_1^2 c_{2233} \pi_{16} + \dot{q}_1^2 (s_2 l_1 + 0.5 s_{22} l_2) l_2 \pi_{20} \\
&\quad - ((2\dot{q}_2 + \dot{q}_3) \dot{q}_3 s_3 l_2 - \dot{q}_1^2 (s_{23} l_1 - s_{223} l_2)) \pi_{21} \\
&\quad - ((2\dot{q}_2 + \dot{q}_3) \dot{q}_3 c_3 l_2 - \dot{q}_1^2 (c_{23} l_1 + c_{223} l_2)) \pi_{22} \\
c_3 &= -0.5 \dot{q}_1^2 s_{2233} \pi_7 - \dot{q}_1^2 c_{2233} \pi_{16} + ((0.5 \dot{q}_1^2 + \dot{q}_2^2) s_3 l_2 \\
&\quad + \dot{q}_1^2 (s_{23} l_1 + 0.5 s_{223} l_2)) \pi_{21} \\
&\quad + (0.5 \dot{q}_1^2 + \dot{q}_2^2) c_3 l_2 + \dot{q}_1^2 (c_{23} l_1 + 0.5 c_{223} l_2) \pi_{22}
\end{aligned} \tag{B.32}$$

while $c_i = 0$ for $i = 4, 5, 6$. The diagonal matrix of viscous friction coefficients is given by:

$$\begin{aligned} F_{00} &= \pi_8 \\ F_{11} &= \pi_9 \\ F_{22} &= \pi_{15} \\ F_{33} &= \pi_{25} \\ F_{44} &= \pi_{27} \\ F_{55} &= \pi_{29} \\ F_{66} &= \pi_{31}. \end{aligned} \tag{B.33}$$

The vector of gravity torques is given by:

$$\begin{aligned} g_0 &= 0 \\ g_1 &= 0 \\ g_3 &= g(\pi_{21}c_{23} - \pi_{22}s_{23}) \\ g_2 &= g((\pi_{13} + l_2\pi_{20})c_2 - \pi_{14}s_2) \end{aligned} \tag{B.34}$$

while $g_i = 0$ for $i = 4, 5, 6$.

References

- [1] An, C.H., Atkeson, C.G., and Hollerbach, J.M. (1988). *Model-Based Control of a Robot Manipulator*. MIT Press, Cambridge, MA.
- [2] An, C.H. and Hollerbach, J.M. (1989). The role of dynamic models in Cartesian force control of manipulators. *Int. J. of Robotics Research*, 8(4):51–72.
- [3] Anderson, R.J. (1989). Passive computed torque algorithms for robots. In *Proc. 28th IEEE Conf. on Decision and Control*, Tampa, FL, pp. 1638–1644.
- [4] Anderson, R.J. and Spong, M.W. (1988). Hybrid impedance control of robotic manipulators. *IEEE J. of Robotics and Automation*, 4:549–556.
- [5] Ang, M.H. and Andeen, G.B. (1995). Specifying and achieving passive compliance based on manipulator structure. *IEEE Trans. on Robotics and Automation*, 11:504–515.
- [6] Angeles, J. (1997). *Fundamentals of Robotic Mechanical Systems*. Springer-Verlag, New York.
- [7] Arimoto, S. (1996). *Control Theory of Non-linear Mecahnical Systems*, Oxford University Press, Oxford, UK.
- [8] Arimoto, S., Liu, Y.H., and Naniwa, T. (1993). Model-based adaptive hybrid control for geometrically constrained robots. In *Proc. 1993 IEEE Int. Conf. on Robotics and Automation*, Atlanta, GA, pp. 618–623.
- [9] Atkeson, C.G., An, C.H., and Hollerbach, J.M. (1986). Estimation of inertial parameters of manipulator loads and links. *Int. J. of Robotics Research*, 5(3):101–119.

- [10] Berghuis, H. and Nijmeijer, H. (1993). Global regulation of robots using only position measurements. *Systems & Control Lett.*, 21:289–293.
- [11] Berghuis, H. and Nijmeijer, H. (1993). A passivity approach to controller–observer design for robots. *IEEE Trans. on Robotics and Automation*, 9:740–754.
- [12] Brogliato, B., Landau, I.D., and Lozano, R. (1991). Adaptive motion control of robot manipulators: A unified approach based on passivity. *Int. J. of Robust and Nonlinear Control*, 1:187–202.
- [13] Brogliato, B., Niculescu, S., and Orhant, P. (1997). On the control of finite dimensional mechanical systems with unilateral constraints. *IEEE Trans. on Automatic Control*, 42:200–215.
- [14] Bruni, F., Caccavale, F., Natale, C., and Villani, L. (1996). Experiments of impedance control on an industrial robot manipulator with joint friction. In *Proc. 5th IEEE Int. Conf. on Control Applications*, Dearborn, MI, pp. 205–210.
- [15] Bruyninckx, H., Dumey, S., Dutré, S., and De Schutter, J. (1995). Kinematic models for model-based compliant motion in the presence of uncertainty. *Int. J. of Robotics Research*, 14:465–482.
- [16] Caccavale, F. and Chiacchio, P. (1994). Identification of dynamic parameters and feedforward control for a conventional industrial manipulator. *Control Engineering Practice*, 2:1039–1050.
- [17] Caccavale, F., Natale, C., Siciliano, B., and Villani, L. (1997). Experiments of spatial impedance control. In *Experimental Robotics V*, Casals, A. and de Almeida, A.T. (Eds.), Springer-Verlag, London, pp. 93–104.
- [18] Caccavale, F., Natale, C., Siciliano, B., and Villani, L. (1998). Resolved-acceleration control of robot manipulators: A critical review with experiments. *Robotica*, 16:565–573.
- [19] Caccavale, F., Natale, C., Siciliano, B., and Villani, L. (1999). Six-DOF impedance control based on angle/axis representations. *IEEE Trans. on Robotics and Automation*, 15:289–300.
- [20] Caccavale, F., Siciliano, B., and Villani, L. (1998). Quaternion-based impedance with nondiagonal stiffness for robot manipulators. In *Proc. 1998 American Control Conference*, Philadelphia, PA, pp. 468–472.
- [21] Caccavale, F., Siciliano, B., and Villani, L. (1999). Robot impedance control with nondiagonal stiffness. *IEEE Trans. on Automatic Control*, 44:1943–1946.

- [22] Canudas de Wit, C., and Brogliato, B. (1997). Direct adaptive impedance control including transition phases. *Automatica*, 33:643–649.
- [23] Canudas de Wit, C., Siciliano, B., and Bastin, G. (Eds.) (1996). *Theory of Robot Control*, Springer-Verlag, London.
- [24] Chiaverini, S. and Sciavicco, L. (1993). The parallel approach to force/position control of robotic manipulators. *IEEE Trans. on Robotics and Automation*, 9:361–373.
- [25] Chiaverini, S., Siciliano, B., and Villani, L. (1994). Force/position regulation of compliant robot manipulators. *IEEE Trans. on Automatic Control*, 39:647–652.
- [26] Chiaverini, S., Siciliano, B., and Villani, L. (1996). Parallel force/position control schemes with experiments on an industrial robot manipulator. In *Prepr. 13th World Congress of IFAC*, San Francisco, CA, vol. A, pp. 25–30.
- [27] Chiaverini, S., Siciliano, B., and Villani, L. (1997). An adaptive force/position control scheme for robot manipulators. *Applied Mathematics and Computer Science*, 7:293–303.
- [28] Chiaverini, S., Siciliano, B., and Villani, L. (1998). Force and position tracking: Parallel control with stiffness adaptation. *IEEE Control Systems Mag.*, 18(1):27–33.
- [29] Chiaverini, S., Siciliano, B., and Villani, L. (1999). A survey of robot interaction control schemes with experimental comparison. *IEEE/ASME Trans. on Mechatronics*, 4:273–285.
- [30] Chou, J.C.K. (1992). Quaternion kinematic and dynamic differential equations. *IEEE Trans. on Robotics and Automation*, 8:53–64.
- [31] Colbaugh, R., Seraji, H., and Glass, K. (1993). Direct adaptive impedance control of robot manipulators. *J. of Robotic Systems*, 10:217–248.
- [32] Craig, J.J. (1989). *Introduction to Robotics: Mechanics and Control*. 2nd Ed., Addison-Wesley, Reading, MA.
- [33] De Luca, A. and Manes, C. (1994). Modeling robots in contact with a dynamic environment. *IEEE Trans. on Robotics and Automation*, 10:542–548.
- [34] De Luca, A., Oriolo, G., and Siciliano, B. (1992). Robot redundancy resolution at the acceleration level. *Laboratory Robotics and Automation*, 4:97–106.

- [35] De Schutter, J., Bruyninckx, H., Zhu, W.-H., and Spong, M.W. (1998). Force control: A bird's eye view. In *Control Problems in Robotics and Automation*, Siciliano, B. and Valavanis, K.P. (Eds.), Springer-Verlag, London, pp. 1–17.
- [36] De Schutter, J. and Van Brussel, H. (1988). Compliant robot motion II. A control approach based on external control loops. *Int. J. of Robotics Research*, 7(4):18–33.
- [37] Doglioni, F., Magnani, G., and Sciavicco, L. (1993). An open architecture industrial controller. *Newsl. of IEEE Robotics and Automation Society*, 7(3):19–21.
- [38] Dombre, E. and Khalil, W. (1988). *Modélisation et Commande des Robots*. Hermès, Paris.
- [39] Egeland, O. and Godhavn, J.-M. (1994). Passivity-based adaptive attitude control of a rigid spacecraft. *IEEE Trans. on Automatic Control*, 39:842–846.
- [40] Eppinger, S.D. and Seering, W.P. (1987). Introduction to dynamic models for robot force control. *IEEE Control Systems Mag.*, 7(2):48–52.
- [41] Fasse, E.D. (1997). On the spatial compliance of robotic manipulators. *ASME J. of Dynamic Systems, Measurement, and Control*, 119:839–844.
- [42] Fasse, E.D. and Broenink, J.F. (1997). A spatial impedance controller for robotic manipulation. *IEEE Trans. on Robotics and Automation*, 13:546–556.
- [43] Featherstone, R. and Khatib, O. (1997). Load independence of the dynamically consistent inverse of the Jacobian matrix. *Int. J. of Robotics Research*, 16:168–170.
- [44] Ferretti, G., Magnani, G., and Rocco, P. (1995). On the stability of integral force control in case of contact with stiff surfaces. *ASME J. of Dynamic Systems, Measurement, and Control*, 117:547–553.
- [45] Gautier, M. and Khalil, W. (1990). Direct calculation of minimum set of inertial parameters of serial robots. *IEEE Trans. on Robotics and Automation*, 6:368–373.
- [46] Ghorbel, F., Srinivasan, B., and Spong, M.W. (1998). On the uniform boundedness of the inertia matrix of serial robot manipulators. *J. of Robotic Systems*, 15:17–28.

- [47] Goldstein, H. (1980). *Classical Mechanics*. 2nd Ed., Addison-Wesley, Reading, MA.
- [48] Gorinevski, D.M., Formalsky, A.M., and Schneider, A.Yu. (1997). *Force Control of Robotics Systems*, CRC Press, Boca Raton, FL.
- [49] Grimm, W.M. (1990). Robot non-linearity bounds evaluation techniques for robust control. *Int. J. of Adaptive Control and Signal Processing*, 4:501–522.
- [50] Hogan, N. (1985). Impedance control: An approach to manipulation: Parts I—III. *ASME J. of Dynamic Systems, Measurement, and Control*, 107:1–24.
- [51] Hogan, N. (1988). On the stability of manipulators performing contact tasks. *IEEE J. of Robotics and Automation*, 4:677–686.
- [52] Hollis, R.L., Salcudean, S.E., and Allan, A.P. (1991). A six-degree-of-freedom magnetically levitated variable compliance fine-motion wrist: Design, modeling and control. *IEEE Trans. on Robotics and Automation*, 7:320–333.
- [53] Hsu, P., Hauser, J., and Sastry, S. (1898). Dynamic control of redundant manipulators. *J. of Robotic Systems*, 6:133–148.
- [54] Kazerooni, H. (1990). Contact instability of the direct drive robot when constrained by a rigid environment. *IEEE Trans. on Automatic Control*, 35:710–714.
- [55] Kazerooni, H., Sheridan, T.B., and Houpt, P.K. (1986). Robust compliant motion for manipulators, Part I: The fundamental concepts of compliant motion. *IEEE J. of Robotics and Automation*, 2:83–92.
- [56] Kelly, R., Carelli, R., Amestegui, M., and Ortega, R. (1989). Adaptive impedance control of robot manipulators,” *IASTED Int. J. of Robotics and Automation*, 4(3):134–141.
- [57] Khatib, O. (1987). A unified approach for motion and force control of robot manipulators: The operational space formulation. *IEEE J. of Robotics and Automation*, 3:43–53.
- [58] Khosla, P.K. and Kanade, T. (1985). Parameter identification of robot dynamics. In *Proc. 24th IEEE Conf. on Decision and Control*, Fort Lauderdale, FL, pp. 1754–1760.
- [59] Lin, S.K. (1988). Euler parameters in robot Cartesian control. In *Proc. 1988 IEEE Int. Conf. on Robotics and Automation*, Philadelphia, PA, pp. 1676–1681.

- [60] Lin, S.K. (1989). Singularity of a nonlinear feedback control scheme for robots. *IEEE Trans. on Systems, Man, and Cybernetics*, 19:134–139.
- [61] Lončarić, J. (1987). Normal forms of stiffness and compliance matrices. *IEEE J. of Robotics and Automation*, 3:567–572.
- [62] Loría, A. and Ortega, R. (1996). Output feedback force-position regulation of robot manipulators. *Automatica*, 32:939–943.
- [63] Lozano, R. and Brogliato, B. (1992). Adaptive hybrid force-position control for redundant manipulators. *IEEE Trans. on Automatic Control*, 37:1501–1505.
- [64] Lu, W.-S. and Meng, Q.-H. (1991). Impedance control with adaptation for robotic manipulators. *IEEE Trans. on Robotics and Automation*, 7:408–415.
- [65] Lu, Z. and Goldenberg, A.A. (1995). Robust impedance control and force regulation: Theory and experiments. *Int. J. of Robotics Research*, 14:225–254.
- [66] Luh, J.Y.S., Walker, M.W., and Paul, R.P.C. (1980). Resolved-acceleration control of mechanical manipulators. *IEEE Trans. on Automatic Control*, 25:468–474.
- [67] McClamroch, N.H. and Wang, D. (1988). Feedback stabilization and tracking of constrained robots. *IEEE Trans. on Automatic Control*, 33:419–426.
- [68] Mills, J.K. and Goldenberg, A.A. (1989). Force and position control of manipulators during constrained motion tasks. *IEEE Trans. on Robotics and Automation*, 5:30–46.
- [69] Mills, J.K. and Lokhorst, D.M. (1993). Control of robotic manipulators during general task execution: A discontinuous control approach. *Int. J. of Robotics Research*, 12:146–163.
- [70] Murray, R.M., Li Z., and Sastry, S.S. (1994). *A Mathematical Introduction to Robotic Manipulation*, CRC Press, Boca Raton, FL.
- [71] Nakamura, Y. (1991). *Advanced Robotics: Redundancy and Optimization*. Addison-Wesley, Reading, MA.
- [72] Natale, C., Siciliano, B., and Villani, L. (1998). Control of moment and orientation for a robot manipulator in contact with a compliant environment. In *Proc. 1998 IEEE Int. Conf. on Robotics and Automation*, Leuven, B, pp. 1755–1760.

- [73] Natale, C., Siciliano, B., and Villani, L. (1999). Spatial impedance control of redundant manipulators. In *Proc. 1999 IEEE Int. Conf. on Robotics and Automation*, Detroit, MI, pp. 1788–1793.
- [74] Nemec, B. and Žlajpah, L. (1998). Implementation of force control on redundant robot. In *Proc. 1998 IEEE/RSJ Int. Conf. on Intelligent Robots and Systems*, Victoria, B.C., CAN, pp. 1314–1320.
- [75] Nicolò, F. and Katende, J. (1983). A robust MRAC for industrial robots. In *Proc. 2nd IASTED Int. Symp. on Robotics and Automation*, Lugano, CH, pp. 162–171.
- [76] Niemeyer, G. and Slotine, J.-J.E. (1991). Performance in adaptive manipulator control. *Int. J. of Robotics Research*, 10:149–161.
- [77] Ortega, R., Loría, A., and Kelly, R. (1995). A semiglobally stable output feedback PI²D regulator for robot manipulators. *IEEE Trans. on Automatic Control*, 40:1432–1436.
- [78] Ortega, R., Loría, A., Nicklasson, P.J., and Sira-Ramírez, H. (1998). *Passivity-based Control of Euler-Lagrange Systems*, Springer-Verlag, London.
- [79] Ortega, R. and Spong, M.W. (1989). Adaptive motion control of rigid robots: a tutorial. *Automatica*, 25:877–888.
- [80] Patterson, T. and Lipkin, H. (1993). Structure of robot compliance. *ASME J. of Mechanical Design*, 115:576–580.
- [81] Paul, R.P. (1981). *Robot Manipulators: Mathematics, Programming, and Control*. MIT Press, Cambridge, MA.
- [82] Paul, R. and Shimano, B. (1976). Compliance and control. In *Proc. 1976 Joint Automatic Control Conf.*, San Francisco, CA, pp. 694–699.
- [83] Peshkin, M.A. (1990). Programmed compliance for error corrective assembly. *IEEE Trans. on Robotics and Automation*, 6:473–482.
- [84] Raibert, M.H. and Craig, J.J. (1981). Hybrid position/force control of manipulators. *ASME J. of Dynamic Systems, Measurement, and Control*, 103:126–133.
- [85] Raucent, B., Campion, G., Bastin, G., Samin, J.C., and Willems, P.Y. (1992). Identification of the barycentric parameters of robot manipulators from external measurements. *Automatica*, 28:1011–1016.
- [86] Roberson, R.E. and Schwertassek, R. (1988). *Dynamics of Multibody Systems*. Springer-Verlag, Berlin.

- [87] Salisbury, J.K. (1980). Active stiffness control of a manipulator in Cartesian coordinates. In *Proc. 19th IEEE Conf. on Decision and Control*, Albuquerque, NM, pp. 95–100.
- [88] Sciavicco, L. and Siciliano, B. (1996). *Modeling and Control of Robot Manipulators*. McGraw-Hill, New York.
- [89] Seraji, H. (1987). Adaptive force and position control of manipulators. *J. of Robotic Systems*, 4:551–578.
- [90] Shepperd, S.W. (1978). Quaternion from rotation matrix. *AIAA J. of Guidance and Control*, 1:223–224.
- [91] Siciliano, B. and Villani, L. (1993). An adaptive force/position regulator for robot manipulators. *Int. J. of Adaptive Control and Signal Processing*, 7:389–403.
- [92] Siciliano, B. and Villani, L. (1996). A passivity-based approach to force regulation and motion control of robot manipulators. *Automatica*, 32:443–447.
- [93] Siciliano, B. and Villani, L. (1996). Adaptive compliant control of robot manipulators. *Control Engineering Practice*, 4:705–712.
- [94] Siciliano, B. and Villani, L. (1997). Design of parallel force/position controllers and observers for robot manipulators. In *Modelling and Control of Mechanical Systems*, Astolfi, A. et al. (Eds.), Imperial College Press, London, pp. 203–218.
- [95] Siciliano, B. and Villani, L. (1997). Six-degree-of-freedom impedance robot control. In *Proc. 8th Int. Conf. on Advanced Robotics*, Monterey, CA, pp. 387–392.
- [96] Siciliano, B. and Villani, L. (1997). An output feedback parallel force/position regulator for a robot manipulator in contact with a compliant environment. *Systems & Control Lett.*, 29:295–300.
- [97] Siciliano, B. and Villani, L. (1998). Passivity-based interaction controller and observer for robot manipulators. *ASME J. of Dynamic Systems, Measurement, and Control*, 120:516–520.
- [98] Slotine, J.-J.E. and Li, W. (1987). On the adaptive control of robot manipulators. *Int. J. of Robotics Research*, 6(3):49–59.
- [99] Spong, M.W. and Vidyasagar, M. (1989). *Robot Dynamics and Control*, Wiley, New York.

- [100] Takegaki, M. and Arimoto, S. (1981). A new feedback method for dynamic control of manipulators. *ASME J. of Dynamic Systems, Measurement, and Control*, 102:119–125.
- [101] Tarn, T.-J., Wu, Y., Xi, N., and Isidori, A. (1996). Force regulation and contact transition control. *IEEE Control Systems Mag.*, 16(1):32–40.
- [102] Tomei, P. (1991) Adaptive PD controller for robot manipulators. *IEEE Trans. on Robotics and Automation*, 7:565–5701.
- [103] Volpe, R. and Khosla, P. (1993). A theoretical and experimental investigation of impact control for manipulators. *Int. J. of Robotics Research*, 12:351–365.
- [104] Volpe, R. and Khosla, P. (1993). A theoretical and experimental investigation of explicit force control strategies for manipulators. *IEEE Trans. on Automatic Control*, 38:1634–1650.
- [105] Vukobratović, M. and Nakamura, Y. (1993). Force and contact control in robotic systems. Tutorial at 1993 *IEEE Int. Conf. on Robotics and Automation*, Atlanta, GA.
- [106] Wampler, C.W. and Leifer, L.J. (1988). Applications of damped least-squares methods to resolved-rate and resolved-acceleration control of manipulators. *ASME J. of Dynamic Systems, Measurement, and Control*, 110:31–38.
- [107] Wen, J.T.-Y. and Kreutz-Delgado, K. (1991). The attitude control problem. *IEEE Trans. on Automatic Control*, 36:1148–1162.
- [108] Wen, J. and Murphy, S. (1991). Stability analysis of position and force control for robot arms. *IEEE Trans. on Automatic Control*, 36:365–371.
- [109] Whitney, D.E. (1977). Force feedback control of manipulator fine motions. *ASME J. of Dynamic Systems, Measurement, and Control*, 99:91–97.
- [110] Whitney, D.E. (1982). Quasi-static assembly of compliantly supported rigid parts. *ASME J. of Dynamic Systems, Measurement, and Control*, 104:65–77.
- [111] Whitney, D.E. (1987). Historical perspective and state of the art in robot force control. *Int. J. of Robotics Research*, 6(1):3–14.
- [112] Wilfinger, L.S., Wen, J.T., and Murphy, S.H. (1994). Integral force control with robustness enhancement. *IEEE Control Systems Mag.*, 14(1):31–40.

- [113] Yao, B. and Tomizuka, M. (1995) Adaptive control of robot manipulators in constrained motion — Controller design. *ASME J. of Dynamic Systems, Measurement, and Control*, 117:320–328.
- [114] Yao, B. and Tomizuka, M. (1998). Adaptive robust motion and force tracking control of robot manipulators in contact with compliant surfaces with unknown stiffness. *ASME J. of Dynamic Systems, Measurement, and Control*, 120:232–240.
- [115] Yoshikawa, T. (1987). Dynamic hybrid position/force control of robot manipulators—Description of hand constraints and calculation of joint driving force. *IEEE J. of Robotics and Automation*, 3:386–392.
- [116] Yoshikawa, T. (1990). *Foundations of Robotics*. MIT Press, Cambridge, MA.
- [117] Yuan, J.S.-C. (1988). Closed-loop manipulator control using quaternion feedback. *IEEE J. of Robotics and Automation*, 4:434–440.

Index

- Active compliance, 32
- Active impedance, 37
- Adaptive control, 91, 94, 99
- Alternative Euler angles displacement, 45
- Alternative Euler angles error, 27, 46
- Angle/axis, 117
- Angle/axis displacement, 44, 46
- Angle/axis error, 16–17, 28, 49
- Angular velocity, 9, 113, 116–117, 119
- Compliance, 32
- Compliance control, 2, 31, 35
- Compliant frame, 39, 66, 70, 76
- Contact force, 2
- Contact stiffness, 33, 70, 76, 82
- Differential kinematics, 9
- Direct force control, 2, 65
- Disturbance rejection, 39
- Dynamic model, 10, 89, 128
- Dynamic model properties, 11, 90
- Dynamic model-based compensation, 12, 36, 67
- Dynamically consistent pseudo-inverse, 24
- End-effector force, 11
- End-effector moment, 11
- End-effector orientation, 8
- End-effector position, 8
- Euler angles, 114
- Euler angles displacement, 44
- Euler angles error, 14, 27, 46
- Experimental apparatus, 4
- Experiments, 34, 40, 51, 68, 78, 84, 100, 110
- Force and motion control, 69
- Force and position control, 72, 79, 106
- Force and position regulation, 70, 78, 91, 104
- Force regulation, 65
- Force tracking, 82
- Force/torque sensor, 2, 6, 37
- Hybrid position/force control, 3
- Impedance, 36
- Impedance control, 2, 36, 41
- Indirect force control, 2, 31
- Inner motion control, 38, 41, 67
- Inner/outer motion/force control, 3
- Integral control, 67, 74, 76
- Interaction control, 1
- Interaction with environment, 1
- Internal motion, 23
- Inverse dynamics control, 12
- Jacobian, 9, 89, 125
- Joint variables, 8
- Kinematic control, 12
- Kinematic model, 8, 121
- Kinematic singularity, 9
- Kinetic energy, 10, 26, 43, 47
- Linear observer, 104
- Linear velocity, 9, 113
- Moment and orientation control, 75, 80
- Motion control, 1, 7
- Mutual orientation, 114, 116, 119
- Nondiagonal stiffness, 61
- Nonlinear observer, 107
- Open control architecture, 5
- Orientation control, 13, 27
- Orientation error, 14
- Outer force control, 66
- Output feedback control, 103
- Parallel composition, 70, 73–76
- Parallel control, 3, 70
- Passive compliance, 34
- Passivity-based control, 97, 106
- PD control with gravity compensation, 26
- Position control, 13, 27
- Position error, 14, 40
- Position vector, 8, 113
- Potential energy, 10, 26–28, 43, 47, 50
- Quaternion, 118
- Quaternion displacement, 44, 50
- Quaternion error, 19, 28, 51
- Redundancy, 9
- Redundancy resolution, 23, 59

- Regulation, 26, 66, 91, 104
Remote center of compliance, 34
Representation singularity, 15, 54, 115, 117
Resolved acceleration, 12–13
Rotation matrix, 8, 113
Rotational impedance, 43–45, 48
Six-DOF impedance control, 43, 52, 54, 56–57, 59
Six-DOF stiffness, 61
Static model-based compensation, 26, 32, 66
Stiffness control, 2
Task geometric consistency, 43–44, 46, 49, 57, 63
Task space control, 12
Task space dynamics, 89
Three-DOF impedance control, 40–41
Tracking control, 12
Translational impedance, 40